# Towards a Quantum Network with Waveguide Quantum Electrodynamics

by

Aziza Almanakly

B.E. Electrical Engineering, The Cooper Union for the Advancement of Science and Art (2020)

Submitted to the Department of Electrical Engineering and Computer Science
in partial fulfillment of the requirements for the degree of

Master of Science

at the

MASSACHUSETTS INSTITUTE OF TECHNOLOGY

September 2022

Author . . . . . . . . . . . . . . . . . . . . . . . . . . . . . . . . . . . . . . . . . . . . . . . . . . . . . . . .
Department of Electrical Engineering and Computer Science
August 26, 2022

Certified by. . . . . . . . . . . . . . . . . . . . . . . . . . . . . . . . . . . . . . . . . . . . . . . . . . . . .
William D. Oliver
Professor of Electrical Engineering and Computer Science and Physics
Thesis Supervisor

Accepted by . . . . . . . . . . . . . . . . . . . . . . . . . . . . . . . . . . . . . . . . . . . . . . . . . . . .
Leslie A. Kolodziejski
Professor of Electrical Engineering and Computer Science
Chair, Department Committee on Graduate Students

# Towards a Quantum Network with Waveguide Quantum Electrodynamics

by

Aziza Almanakly

Submitted to the Department of Electrical Engineering and Computer Science
on August 26, 2022, in partial fulfillment of the
requirements for the degree of
Master of Science

## Abstract

Over the past twenty years, the field of quantum computing has progressed from the investigation of individual quantum systems towards the implementation of many-qubit processors. Distributing information processing over a quantum network consisting of many nodes that communicate via itinerant photons is one potential framework for achieving modular and extensible quantum computation. Systems of superconducting qubits strongly coupled to a continuum of photonic modes in 1D coplanar waveguides, described by the formalism known as waveguide Quantum Electrodynamics (wQED), are emerging as a promising platform for quantum communication. In this work, we develop a quantum module comprised of superconducting qubits strongly coupled to a 1D waveguide that can bidirectionally emit and absorb propagating microwave photons on-demand. These modules can be tiled in series along a waveguide to form an all-to-all, extensible quantum network.

Thesis Supervisor: William D. Oliver
Title: Professor of Electrical Engineering and Computer Science and Physics

# Acknowledgments

First I would like to thank my mentors that have guided me throughout these last two years and made this thesis possible. I thank my advisor Will Oliver, for his continuous support throughout my graduate career. He leads by example, and has taught me what it means and what it takes to become a rigorous, organized, and disciplined scientist, but also a kind and caring leader. He pushes me to write and communicate effectively, and to always think about the broader context of my work. I also thank Research Scientist Jeffrey Grover, who has graciously edited this thesis. He never hesitates to share his expertise in the field of wQED and superconducting systems and has helped me squash many experimental bugs. Jeff is a mentor that genuinely cares about my growth as a researcher. He helps me work through day-by-day problems, and through this I verbalize and solve the problem I am tackling. I also want to thank Principal Investigator Simon Gustavson, for sharing his expertise on the electronics and equipment that would be completely daunting without his guidance and expertise.

For Bharath Kannan, a senior graduate student I started working with immediately, where do I start? I have spent the last two years trying to download his brain and learn everything I need in order to carry on the wQED research branch in the EQuS group. I am still consistently amazed by the science he continues to accomplish. It has been such a privilege and delight to work closely with him everyday – his direct and thorough mentorship has quickly taught me the entire workflow of projects in superconducting wQED, from device design and simulation, to the construction of the experimental setup, to the performance of experiments, and finally to the data analysis and manuscript preparation. He has also become my one of my closest friends, and has made graduate school so fun and exciting.

I am grateful for the support system natural to the EQuS group. There is a constant flow of ideas, and we have a lot of fun at and after work. I want to thank Team 3080 for making building a new lab so fun: Bharath, David, Lamia, Miuko, and Joel. I thank Junyoung and Will B., who joined the group at the same time as me and have become my team for tackling classes and graduate school in general. I also want to thank my close friends Skylar, Katie, Miela, and Reenad for always being there for me. We have so much fun together and lift each other up throughout the process of becoming scientists.

Finally, I want to thank my family. Without their love, support, and encouragement, this thesis and my academic career would not have possible. My parents Fadwa and Maher immigrated across the world and worked hard their entire lives so that my younger brothers, Husam and Waseem, and I could have the privilege of working towards our dreams without burden. They instilled in me the importance of education and hard work, but more importantly, caring for your loved ones and your community.

# Contents

# List of Figures

# List of Tables

# Chapter 1

# Introduction

Modern computer networks at a high level are composed of nodes that store and process information, and communication interconnects that mediate the transfer of information between nodes [1]. Large-scale networks such as the Internet connect end-systems, including computers, servers, and mobile devices, over long distances. These end-systems communicate via electromagnetic waves in the atmosphere or through physical media such as fiber-optic cables.

Even these end-systems themselves, however, contain internal small networks comprising interconnected integrated circuits on a motherboard with specified functions that fall into two main categories: logic and memory. These chips communicate locally through electronic signal lines known as busses to execute a program [2, 3]. The individual integrated circuits are nodes in the network that communicate via electronic circuit interconnects and data busses.

Quantum networks are built on similar principles, but they handle a fundamentally different type of information. At a high level, quantum networks also comprise computational nodes that store and process information. These nodes transmit and receive, or — in more suggestive physical language — emit and absorb, information from other nodes in the network through a communication interconnect. There are several developing quantum network architectures consisting of different physical nodes and communication channels. Nodes are composed of stationary qubits — or physical two-level quantum systems — such as trapped ions, trapped neutral

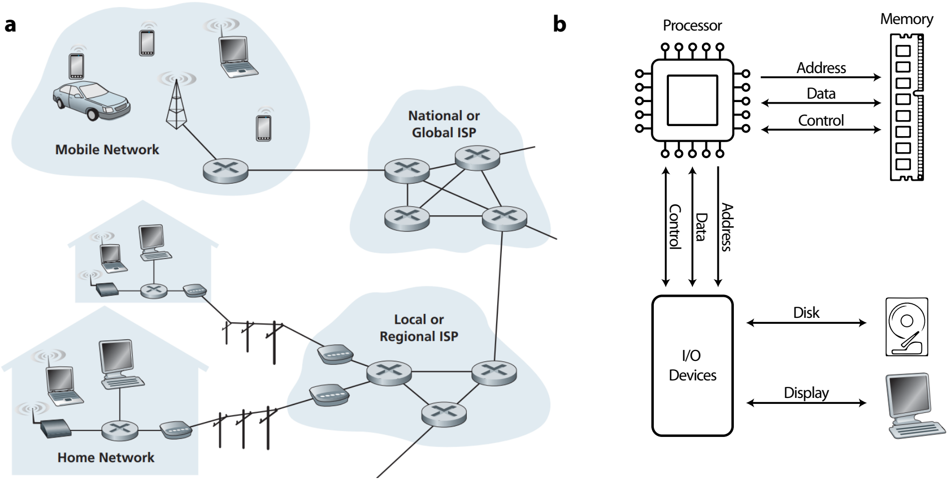

Figure 1-1: **Types of classical computing networks.** **a)** Illustration of the Internet, adapted from [1]. Information transfer between end-systems is either wireless or mediated by physical cables. **b)** Simple computer architecture. Information flows (both data and instruction) between the processor and memory through data busses in a Von Neumann architecture [2] – the architecture of nearly all modern computers. The processor also controls the flow of data through input/output devices to the outside world. This illustration shows that computers rely on the communication of logic and memory components in order to execute a program.

atoms, and superconducting artificial atoms. Communication channels rely on so-called flying qubits that travel between nodes with the intention of generating remote entanglement. Examples of flying qubits include optical photons propagating in optical fibers or photonic waveguides [4–10], mobile ions or neutral atoms in laser trap systems [11–13], and microwave photons in resonators or waveguides [14–24].

The so-called quantum internet operates through the distribution of entanglement across nodes to teleport quantum information with error-correction [25]. Optical photons (telecom-wavelength) are ideal flying qubits because of their ability to travel quickly over metropolitan-scale distances in optical fibers or the atmosphere [26]. In fact, optical photons in a single-mode fiber have teleported qubits over a distance of 44 km [27]. Optical quantum networks advance towards the realization of quantum key distribution for secure communication and the quantum internet [25, 26].

Superconducting artificial atoms offer several advantages as stationary qubits because they can be custom-designed, controlled with conventional microwave electronics, and scaled due to established fabrication techniques. However, superconducting

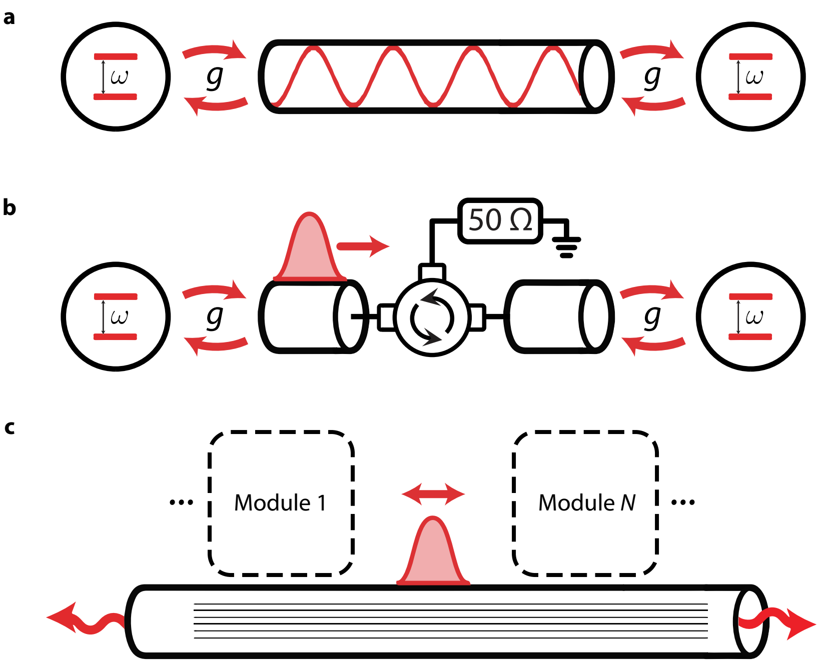

Figure 1-2: **Quantum interconnects with superconducting circuits. a)** Coherent coupling of distant qubits through resonant modes of a cavity, which serve as the communication link. **b)** Quantum information transfer via itinerant single-photon propagation through a unidirectional waveguide. **c)** Proposed architecture for a quantum interconnect where communication modules communicate via itinerant microwave photons in a bidirectional waveguide.

qubits interact with microwave photons, which have a much lower energy than optical photons. Thermal radiation at microwave wavelengths dominates at room temperature and coaxial cables are generally more lossy than optical fibers [28]. Therefore, microwave photons are not ideal flying qubits for long-distance communication. Integrating superconducting qubits into low-loss optical quantum networks requires efficient microwave-to-optical transduction [29, 30].

Though the ideal long-distance quantum internet is not yet physically compatible with the superconducting systems, local networks within superconducting circuits offer the opportunity to distribute quantum information amongst nodes for robust computation. In analogy to classical computer processors, a potential architecture for quantum processors uses microwave resonators or waveguides as data busses to connect superconducting chips. In this quantum computer architecture, the superconducting nodes communicate via microwave photons.

A module that can store, communicate, and process quantum information has been realized within a circuit Quantum Electrodynamics (cQED) architecture, where artificial atoms interact with confined microwave photons. These modules use resonant modes in cavities as communication channels [14–18] as illustrated in Fig. 1-2a. This approach results in high-fidelity, bidirectional communication between modules, but it is not easily extensible. Module connectivity is limited in a quantum network of arbitrary size, and the free-spectral range of the resonant cavity constrains the distance between modules. Increasing resonator length decreases the frequency spacing between resonant modes, which limits communication protocols between distant modules. An alternative recent approach involves communication via itinerant (propagating) photons on a single-ended waveguide, which offers more versatile module connectivity [20, 23, 24] as pictured in Fig. 1-2b. However, to create a 50-$\Omega$ environment for photon propagation while interfacing with another qubit, this approach requires lossy, non-reciprocal microwave elements, such as circulators, which limit state transfer fidelity and render intra-module communication unidirectional. Instead, we seek to create an quantum network architecture with conventional waveguides as the bidirectional communication link and itinerant photons as the information carriers, as shown in Fig. 1-2c.

To develop modules for these quantum interconnects, we turn to waveguide Quantum Electrodynamics (wQED): a formalism that describes the interaction of superconducting qubits with a continuum of propagating photonic modes. The strong coupling regime is readily accessed in wQED systems because of the 1D confinement of photonic modes in the waveguide and the innately large electric dipole moment of superconduting qubits [31, 32]. This platform provides the opportunity to simultaneously explore light-matter interaction and develop quantum communication systems.

In this work, we experimentally demonstrate on-demand, directional, microwave photon emission based on the quantum interference of indistinguishable photons emitted from a superconducting module into a bidirectional waveguide [33]. We theoretically develop photon absorption and remote entanglement protocols, building towards an extensible superconducting quantum network with all-to-all connectivity.

## 1.1 Outline of thesis

To provide the necessary theoretical background for this work, we introduce circuit QED in Chapter 2. First, we quantize the classical LC circuit as a simple harmonic oscillator. Then we introduce the Josephson junction, a non-linear inductor, to eventually derive the Hamiltonian of both the fixed-frequency and flux-tunable transmon qubit.

In Chapter 3, we study several theoretical models of a single qubit coupled to a waveguide to develop the building blocks of the wQED formalism. We begin by drawing the analogy to an atom coupled to a 1D continuum of photonic modes. Then, we perform a classical circuit treatment for the qubit-waveguide system to study classical scattering parameters. We perform a detailed circuit quantization to derive the wQED Hamiltonian describing the interaction of a qubit with the continuum of modes in a waveguide. We also derive the input-output relations of a qubit coupled to a bidirectional waveguide. Finally, we model the system with a master equation to study the steady-state behavior of the qubit-waveguide system in the presence of several loss channels.

We study and simulate multi-qubit wQED phenomena in Chapter 4. First, we derive the master equation formalism for many qubits coupled to a common waveguide. We employ this formalism to study systems of two qubits coupled to a waveguide at specified inter-qubit distances. At the end of this chapter, we survey some of the superconducting wQED experiments in the last decade.

In Chapter 5, we discuss the first experimental demonstration of directional photon emission in a microwave waveguide. We lay out the device module design and theoretical model before outlining the directional emission protocol. We explain the device calibration process in detail. We use a heterodyne detection scheme to measure the photon temporal envelope and obtain statistics for photon state tomography.

We propose a quantum interconnect capable of both photon emission and absorption by placing two identical modules along a common bidirectional waveguide in Chapter 6. With this quantum interconnect, we develop a photon absorption protocol.

We provide the theory of photon shaping with this module to produce time-symmetric photons such that the absorption protocol is identical to the emission protocol. We also construct a remote entanglement protocol for the quantum interconnect. We conclude the thesis with a proposal to implement emission, absorption, and remote entanglement with an array of these modules in order to create a quantum network.

# Chapter 2

# Circuit Quantum Electrodynamics

A qubit is a quantum two-level system consisting of a ground and an excited state that represent the computational states 0 and 1, respectively. In contrast to a classical bit, which can only be in state 0 or 1, a qubit can be placed in a superposition of its ground and excited states. The energy levels of atoms found in nature can be used to form a qubit. We can also engineer qubits – or artificial atoms – with classical lumped circuit elements such as capacitors and inductors, and quantum circuit elements such as the Josephson junction. By designing artificial atoms to have transition frequencies in the microwave regime, we can use commonplace microwave electronics to control these qubits and their interactions. In this chapter, we provide a brief overview of circuit quantum electrodynamics (cQED), the study of light-matter interaction with engineered quantum systems, which is the foundation for the work in this thesis.

## 2.1 Quantum Harmonic Oscillator

Following the discussion in Ref. [34], we begin by quantizing a simple harmonic oscillator composed of a capacitor with capacitance $C$ and inductor with inductance $L$ in parallel. We define the voltage across the capacitor as $V(t)$ and the current through the inductor as $I(t)$, as shown in Fig. 2-1a. We write the classical Hamiltonian for this system, or the total energy of the $LC$ circuit, as

$$H = \frac{1}{2}CV^2(t) + \frac{1}{2}LI^2(t) = \frac{Q^2(t)}{2C} + \frac{\Phi^2(t)}{2L}, \tag{2.1}$$

where we define the charge at the node as $Q(t) = CV(t)$ and the flux through the circuit loop as $\Phi(t) = LI(t)$. We see that this Hamiltonian resembles that of the simple harmonic oscillator, for example, a block of mass $m$ on a spring with spring constant $k$. The Hamiltonian for the analogous mechanical system is

$$H = \frac{p^2(t)}{2m} + \frac{1}{2}kx^2(t), \tag{2.2}$$

where $x(t)$ is the position of the block and $p(t)$ is the momentum of the block. The flux variable $\Phi(t)$ is analogous to the position variable $x(t)$ of the block, and the charge variable $Q(t) = C\dot{\Phi}(t)$ is analogous to the momentum variable $p(t) = m\dot{x}(t)$. The "mass" of the circuit is the capacitance $C$, and the "spring constant" of the circuit is the inverse of the inductance $1/L$. The resonance frequency of the circuit is $\omega = 1/\sqrt{LC}$, whereas in the block-spring analogy the frequency is $\omega = \sqrt{k/m}$. Because we assign the flux variable as the position-like variable, the potential energy of the circuit is the inductive energy $U = \Phi^2(t)/2L$ and the kinetic energy is the capacitive energy $K = Q^2/2C$. We see from this analogy that flux and charge are conjugate variables and Fourier pairs with a Poisson bracket equal to one

$$\{\Phi, Q\} = \frac{\delta\Phi}{\delta\Phi}\frac{\delta Q}{\delta Q} - \frac{\delta Q}{\delta\Phi}\frac{\delta\Phi}{\delta Q} = 1. \tag{2.3}$$

We promote the $Q(t)$ and $\Phi(t)$ quantum operators $\hat{Q}$ and $\hat{\Phi}$. It follows that the operators have the commutation relation $[\hat{\Phi}, \hat{Q}] = i\hbar$. We write the quantum-mechanical Hamiltonian for the LC circuit as

$$\hat{H} = \frac{\hat{Q}^2(t)}{2C} + \frac{\hat{\Phi}^2(t)}{2L} = 4E_{\mathrm{C}}\hat{n}^2 + \frac{1}{2}E_{\mathrm{L}}\hat{\phi}^2, \tag{2.4}$$

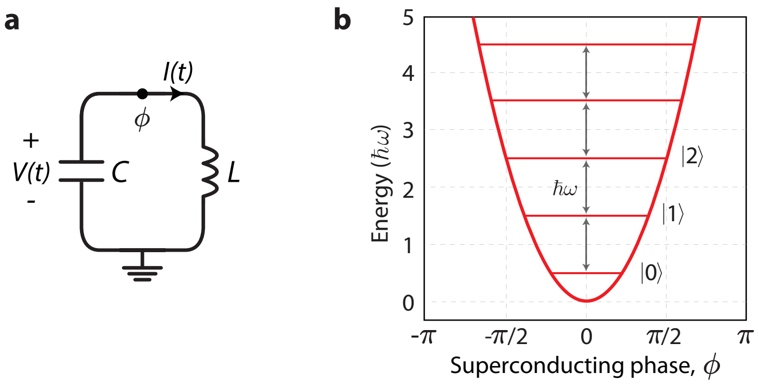

Figure 2-1: **Superconducting LC oscillator circuit and energy potential a)** Parallel LC oscillator circuit schematic. The voltage across the capacitor is denoted as $V(t)$ and the current through the inductor is denoted $I(t)$. The reduced node flux $\phi$ – or the phase across the inductor – is illustrated the node of the circuit. **b)** Energy potential of LC oscillator $U = E_\mathrm{L}\hat{\phi}^2/2$ in terms of the reduced flux, adapted from [34]. The energy levels are equally spaced by the energy quantum of the LC oscillator $\hbar\omega$.

where we define the reduced charge operator $\hat{n} = \hat{Q}/2e$ and reduced flux operator $\hat{\phi} = 2\pi\hat{\Phi}/\Phi_0$; $e$ is the elementary charge and $\Phi_0 = h/2e$ is the magnetic flux quantum. The charging energy $E_\mathrm{C} = e^2/2C$ signifies the energy required to add an electron to the node of the LC circuit. In a superconductor, electrons are effectively attracted to each other and form a condensate of Cooper pairs [35]. The reduced charge operator $\hat{n}$ is the excess number of Cooper-pairs at the node of the LC circuit. The inductive energy is defined as $E_\mathrm{L} = \Phi_0^2/4\pi^2 L$, which means the reduced flux $\hat{\phi}$ is the so-called gauge-invariant phase across the inductor. The commutator of the reduced operators is $[\hat{\phi}, \hat{n}] = i$. We redefine the charge and flux operators in terms of the creation and annihilation operators of the quantum harmonic oscillator

$$\begin{aligned}\hat{\phi} &= \frac{1}{\sqrt{2}}\left(\frac{8E_\mathrm{C}}{E_\mathrm{L}}\right)^{\frac{1}{4}}(\hat{a}^\dagger + \hat{a})\\ \hat{n} &= \frac{i}{\sqrt{2}}\left(\frac{E_\mathrm{L}}{8E_\mathrm{C}}\right)^{\frac{1}{4}}(\hat{a}^\dagger - \hat{a}).\end{aligned} \tag{2.5}$$

We use these relations to rewrite the Hamiltonian of the LC circuit as

$$\hat{H} = \hbar\omega\left(\hat{a}^\dagger\hat{a} + \frac{1}{2}\right), \tag{2.6}$$

where $\omega = \sqrt{8E_\mathrm{C}E_\mathrm{J}} = 1/\sqrt{LC}$ is the resonant frequency of the circuit, and all energy levels of the circuit are evenly spaced by $\hbar\omega$, as illustrated in Fig. 2-1b. There are ideally infinitely many available energy levels in the quantum harmonic oscillator. To excite the oscillator from the ground state $|0\rangle$ to the first excited state $|1\rangle$, we add a photon of energy $\hbar\omega$ to the oscillator. These energy levels are only distinguishable in the low-temperature limit $k_\mathrm{B}T \ll \hbar\omega$ such that there is little ambient thermal photon population. We work with superconducting LC circuits that operate at frequencies around $\omega/2\pi \approx 5$ GHz, which we equate to an effective temperature $T = \hbar\omega/k_\mathrm{B} \approx 240$ mK. Our experiments take place in a dilution refrigerator that cools our devices down to 15 mK, which is well within the low-temperature limit.

Because all energy levels of the quantum harmonic oscillator are equidistantly spaced, there is no uniquely addressable energy transition between two specific levels. This is can be attributed to the linearity of the energy levels as a function of number of photons in the LC oscillator. Therefore, we cannot easily create a qubit from the LC oscillator.

## 2.2 The Josephson Junction

To engineer an individually addressable two-level system with superconducting circuits, we need to introduce nonlinearity to the circuit, which creates anharmonicity in the energy levels. Typically, we use the lowest two energy levels of a system to form a qubit. We define the term anharmonicity $\alpha = \omega_{12} - \omega_{01}$ as the difference between the energies of the $|0\rangle \rightarrow |1\rangle$ and $|1\rangle \rightarrow |2\rangle$ transitions. The quantum harmonic oscillator has zero anharmonicity ($\alpha = 0$) because of the linearity of the system. We use anharmonicity as a metric for the distinguishability of the energy of the two-level system of choice from the energy of the nearest transitions in the system.

The Josephson junction is a nonlinear circuit element composed of two superconducting electrodes separated by a thin layer of insulating material [36, 37]. In this work, all Josephson junctions are composed of aluminum superconducting electrodes separated by aluminum oxide insulators. In each superconducting electrode, the electrons form bosonic Cooper pairs that are indistinguishable from each other and occupy the same ground state. This allows us to treat the Cooper pair fluids in each electrode as having a collective wavefunction with a well-defined superconducting phase [38]. For sufficiently thin insulating barriers, Cooper pairs can tunnel from one electrode to another. The Josephson junction effectively creates a cosine potential for Cooper pairs for small superconducting phases, and the tunneling events can be captured as the hybridization of the wavefunctions of the Cooper pair fluids on each superconducting electrode. The Josephson relations are [38, 39]:

$$\begin{aligned} I(t) &= I_c \sin\phi, \\ V(t) &= \frac{\Phi_0}{2\pi}\frac{d\phi}{dt}, \end{aligned} \tag{2.7}$$

where $I_c$ is the critical current of the junction – or the maximum supercurrent that the junction can support. These relations show how the voltage across and current through the junction depend on the superconducting phase. We define the inductance of the Josephson junction

$$L_{\mathrm{J}} = \frac{V}{\frac{dI}{dt}} = \frac{\Phi_0}{2\pi I_c \cos\phi}. \tag{2.8}$$

The Josephson inductance is nonlinear with current. There is also a small capacitance between the two superconducting metal layers in the Josephson junction, which we usually lump into a larger parallel capacitance in the circuit. Next, we calculate the energy of the junction using the Josephson relations

$$U_{\mathrm{J}} = \int V(t)I(t)dt = -E_{\mathrm{J}}\cos\phi \tag{2.9}$$

where $E_{\mathrm{J}} = \frac{\Phi_0 I_c}{2\pi}$ is defined as the Josephson energy. We can interpret $E_{\mathrm{J}}$ as the coupling between the two superconducting electrodes of the Josephson junction.

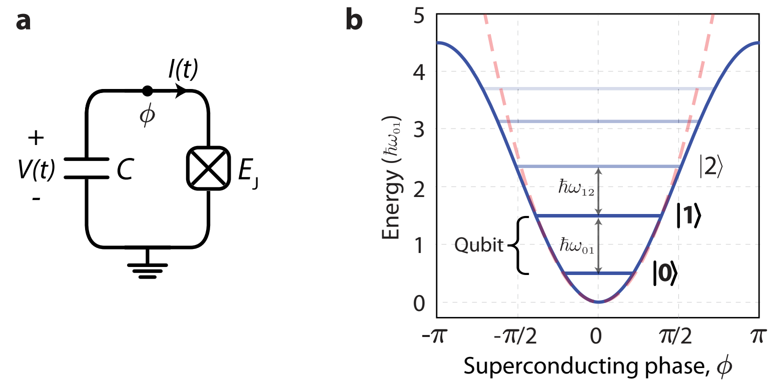

Figure 2-2: **Transmon circuit and energy potential a)** Transmon circuit schematic. The voltage across the capacitor is denoted as $V(t)$ and the current through the Josephson junction is denoted $I(t)$. The reduced node flux $\phi$ – or the phase across the Josephson junction – is illustrated the node of the circuit. **b)** Energy potential of transmon circuit $U = -E_\mathrm{J} \cos \hat{\phi}$ in terms of the reduced flux, adapted from [34]. The nonlinearity introduced by the Josephson junction results in energy levels that are not equally spaced. This allows us to use the lowest energy levels $|0\rangle$ and $|1\rangle$ to form a qubit with transition energy $\hbar\omega_{01}$.

## 2.3 The Transmon Qubit

To create a qubit with an addressable two-level subspace, the inductor in the LC oscillator with the nonlinear Josephson inductance depicted in Fig. 2-2a. We continue to treat the reduced flux of the circuit $\hat{\phi}$ as the position-like variable of the system. Thus, the potential energy of the circuit is $U_\mathrm{J}$ in Eq. 2.9. The Hamiltonian for this system is replaced by

$$\hat{H} = 4E_\mathrm{C}\hat{n}^2 - E_\mathrm{J} \cos \hat{\phi}. \tag{2.10}$$

We work in the limit $E_\mathrm{J} \gg E_\mathrm{C}$ because charge noise sensitivity is suppressed [40] – known as the transmon regime. In practice, we connect the Josephson junction to a larger superconducting electrode that has a shunt capacitance to the ground plane, which we denote as $C$. For large shunt capacitances $C$, the transmon qubit is insensitive to fluctuations in the number of charges on the large superconducting electrode [41].

In the transmon regime, the superconducting phase $\hat{\phi}$ has small zero-point fluctuations, or phase-spread of the transmon wavefunction, $\phi_\mathrm{zpf} = (2E_\mathrm{C}/E_\mathrm{J})^{1/4}$. As a result, the low energy eigenstates of the transmon are well-localized in phase [40]. To approximate the lowest eigenenergies, we use the Taylor expansion for the potential energy $U_\mathrm{J}$, keeping only up to second-order terms [34],

$$\hat{H} = 4E_\mathrm{C}n_\mathrm{J} - E_\mathrm{J}\left(1 - \frac{\hat{\phi}^2}{2!} + \frac{\hat{\phi}^4}{4!}\right). \tag{2.11}$$

We write the charge and flux operators in terms of the creation and annihilation operators of the quantum harmonic oscillator given in Eq. 2.5 and rewrite the transmon Hamiltonian

$$\hat{H} = \hbar\omega_{01}\hat{a}^\dagger\hat{a} + \frac{\hbar\alpha}{2}\hat{a}^\dagger\hat{a}^\dagger\hat{a}\hat{a}, \tag{2.12}$$

where we define the qubit frequency as $\omega_{01} = (\sqrt{8E_\mathrm{J}E_\mathrm{C}} - E_\mathrm{C})/\hbar$ and the anharmonicity as $\alpha = \omega_{12} - \omega_{01} \approx -E_\mathrm{C}$. We design the qubit frequency to be much larger than the aharmonicity ($\omega_{01} \gg |\alpha|$), which allows us treat the transmon as a weakly anharmonic oscillator. The $|1\rangle \rightarrow |2\rangle$ transition is detuned from the $|0\rangle \rightarrow |1\rangle$ transition, so we can effectively treat the transmon as a two-level system:

$$\hat{H} = \frac{\hbar\omega_{01}}{2}\hat{\sigma}_z, \tag{2.13}$$

where $\sigma_z$ is the Pauli-z operator. We use this Hamiltonian throughout the thesis to represent the transmon circuit as a simple two-level system.

## 2.4 Flux-Tunable Transmon Qubit

In this work, we need to control the interaction strength between pairs of qubits, which depends on the difference between their frequencies. Resonant qubits swap energy, while detuned qubits shift each other's frequencies [34, 42]. Detuned and resonant interactions between qubits are resources for the execution of quantum gates, i.e. operations that manipulate qubit states to perform computations. Thus, we need to introduce an external parameter that enables *in situ* qubit frequency tunability.

We use superconducting quantum interference devices (dc-SQUIDs) which consist of two Josephson junctions in parallel, as illustrated in Fig. 2-3a, to introduce an external flux parameter to tune the qubit frequency. To understand the origin of frequency tunability, we consider the dc-SQUID as a superconducting ring. We define the reduced flux across each junction with Josephson energy $E_{\mathrm{J}1/2}$ as $\phi_{1/2}$ referenced to the ground node. Because of the phase coherence of the condensate wavefunction, the phase related to the current around a superconducting ring must be an integer multiple of $2\pi$ – or in other words the total flux is quantized [38]. If we thread the superconducting ring with an external magnetic flux $\Phi_{\mathrm{ext}}$, the total fluxoid around the ring obeys the flux quantization condition

$$\phi_1 - \phi_2 + 2\phi_{\mathrm{ext}} = 2\pi m \tag{2.14}$$

where $m$ is an integer and $\phi_{\mathrm{ext}} = \pi\Phi_{\mathrm{ext}}/\Phi_0$ is the reduced external flux. Using the Josephson relations and Kirchoff's current law, we find the effective current through the dc-SQUID and write the flux-tunable transmon Hamiltonian

$$\hat{H} = 4E_{\mathrm{C}}\hat{n}^2 - (E_{\mathrm{J}1} + E_{\mathrm{J}2})\cos\hat{\phi}\sqrt{\cos^2\phi_{\mathrm{ext}} + d^2\sin^2\phi_{\mathrm{ext}}}, \tag{2.15}$$

where $d = (E_{\mathrm{J}2} - E_{\mathrm{J}1})/(E_{\mathrm{J}2} + E_{\mathrm{J}1})$ is defined as the asymmetry parameter. For $d = 1$, the circuit is effectively a fixed-frequency transmon qubit with a single junction. For $d = 0$, the dc-SQUID is symmetric with $E_{\mathrm{J}1} = E_{\mathrm{J}2}$, providing the maximum qubit frequency tunability range. The reduced external flux bias $\Phi_{\mathrm{ext}}$ changes the effective Josephson energy and therefore the qubit frequency. The qubit frequency now varies as a function of the external flux bias,

$$\omega_{01}(\phi_{\mathrm{ext}}) = \omega_{01,\mathrm{max}}\left[d^2 + (1-d^2)\cos^2(\phi_{\mathrm{ext}})\right]^{\frac{1}{4}} - E_{\mathrm{C}}. \tag{2.16}$$

If there is ambient flux noise, the qubit frequency jitters, resulting in qubit dephasing. Flux-tunable qubits are most sensitive to flux noise where the slope of the spectrum $d\omega/d\phi_{\mathrm{ext}}$ is large, for example $\phi_{\mathrm{ext}} = \pi/4$. For this reason, we choose to operate the qubit near its peak frequency where $d\omega/d\phi_{\mathrm{ext}}$ is near zero. In Fig. 2-3b,

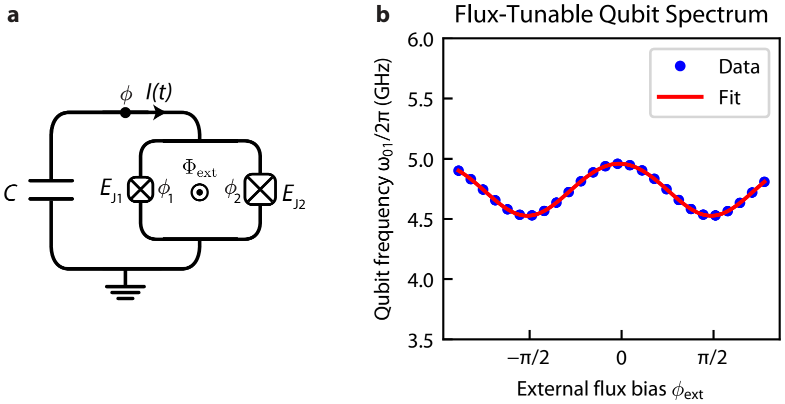

Figure 2-3: **Flux-tunable asymmetric transmon circuit and qubit frequency spectrum.** **a)** Flux-tunable transmon circuit schematic composed of a capacitance $C$ in parallel with a dc-SQUID. The dc-SQUID is composed of two asymmetric Josephson junctions of energies $E_{\mathrm{J1}}$ and $E_{\mathrm{J2}}$ where $E_{\mathrm{J1}} \ll E_{\mathrm{J2}}$. The reduced flux across each junction is $\phi_{1/2}$ **b)** Flux-tunable qubit frequency spectrum. The qubit has charging energy $E_{\mathrm{C}}/h = 268$ MHz and Josephson energies $E_{\mathrm{J1}} = 1.07$ GHz and $E_{\mathrm{J2}} = 11.72$ GHz. For this qubit, the junction asymmetry parameter is $d = 0.834$, indicating that the dc-SQUID is highly asymmetric.

we show an example flux-tunable transmon qubit spectrum, where the dc-SQUID was designed to be highly asymmetric. We designed this qubit to have some range of frequency tunability in order to place multiple qubits near resonance, as discussed in Chapter 5. Because of the large asymmetry, we have a smaller range of frequency tunability as compared to the case of the symmetric dc-SQUID. The slope of the spectrum $d\omega/d\phi_{\mathrm{ext}}$ away from the peak frequency is larger in the case of the symmetric transmon. As a result, by using a highly asymmetric transmon we decrease the sensitivity to flux noise away from the peak frequency, as discussed in Chapter 6.

# Chapter 3

# A Single Qubit on a Waveguide

The formalism of interest for this work is waveguide Quantum Electrodynamics (wQED), which describes atoms coupled to a 1D waveguide. In our platform, superconducting qubits are coupled to a coplanar waveguide, which can host the propagation of electromagnetic modes of a wide range of frequencies. The qubit couples to the 1D continuum of photonic modes in the waveguide. Because of the 1D confinement of these modes and the innately large electric dipole moment of superconducting qubits [31], the strong-coupling regime is readily accessed. The qubit couples more strongly to the 1D continuum of modes in the waveguide than to any other decay channel in the system, which enables us to study light-matter interaction with the wQED formalism.

We begin by describing the interaction of a single qubit with the 1D continuum of modes in the waveguide. We start from an abstract quantum model, comparing a transmon on a waveguide to an atom coupled to the continuum of modes in its environment. Then we employ a classical circuit model for the qubit-waveguide system to study scattering parameters and motivate the idea that a wide range of frequencies can propagate in the waveguide. We then take this circuit model one step further through circuit quantization to derive the wQED Hamiltonian, which describes the interaction of the qubit with modes in the waveguide. To relate the qubit to propagating fields in the waveguide, we introduce a formalism known as input-output theory. Finally, we employ a master equation formalism to the qubit-waveguide system, adding loss

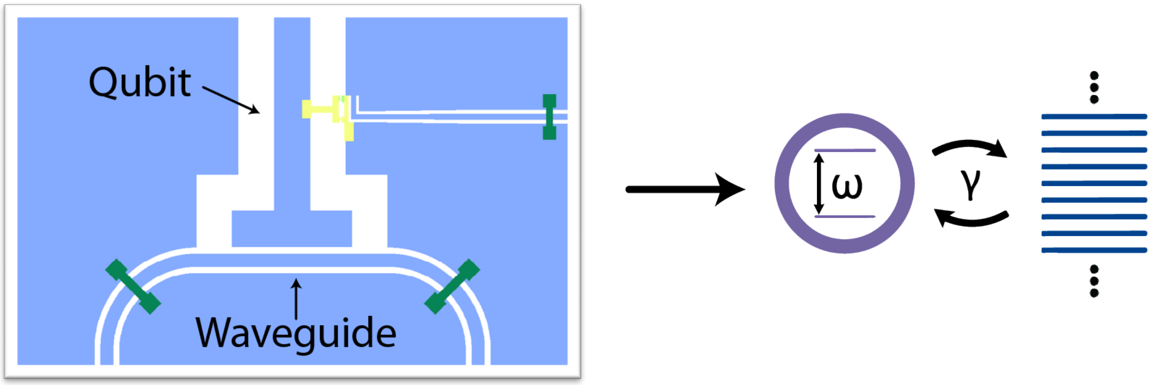

Figure 3-1: **Schematic and abstract quantum model of a single superconducting qubit coupled to a coplanar waveguide.** In the strong-coupling regime, we model this system as an atom of frequency $\omega$ coupled at rate $\gamma$ to a continuum of 1D modes.

mechanisms to the quantum-mechanical model. We derive the scattering parameters of the system from the quantum-mechanical model, and discuss the behavior of a qubit as a mirror to single photons in the waveguide. These are the building blocks of the wQED formalism.

## 3.1 Spontaneous Emission - Fermi's Golden Rule

We model our system of a superconducting qubit coupled to a waveguide as an atom at frequency $\omega$ coupled to a continuum of 1D modes at rate $\gamma$, as pictured in Fig. 3-1. Following the analysis of Ref. [42] using the Wigner-Weisskopf theory of spontaneous emission, we write the system Hamiltonian as

$$\frac{\hat{H}}{\hbar} = \omega_{\mathrm{q}}|1, 0_k\rangle\langle 1, 0_k| + \sum_k \omega_k |0, k\rangle\langle 0, k| + \sum_k \left(g_k |0, k\rangle\langle 1, 0_k| + g_k^* |1, 0_k\rangle\langle 0, k|\right) \quad (3.1)$$

The first two terms describe the energies of the qubit and the modes in the waveguide, respectively. The first index in the bras and kets denotes the state of the qubit, and the second index denotes the state of the $k^{\text{th}}$ mode in the waveguide. The third term describes the interaction between the qubit and the photonic modes. The qubit can emit a photon into the continuum of available modes in the waveguide, and it can also absorb a single photon from the collective fields present in the waveguide. The Rabi frequency $g_k/2\pi$ describes the rate of the coupling interaction between each available mode in the waveguide and the excited state of the qubit. Moving to the frame of the qubit, the Hamiltonian becomes

$$\frac{\hat{H}}{\hbar} = \sum_k (\omega_k - \omega_{\mathrm{q}})|0,k\rangle\langle 0,k| + \sum_k \left(g_k|0,k\rangle\langle 1,0_k| + g_k^*|1,0_k\rangle\langle 0,k|\right) \tag{3.2}$$

To determine the time dynamics of the system, we start with a general time-dependent wavefunction for the system

$$|\psi(t)\rangle = c_1(t)|1,0_k\rangle + \sum_k c_k(t)|0,k\rangle, \tag{3.3}$$

which evolves in time according to the Schrodinger equation,

$$i\hbar\frac{d}{dt}|\psi(t)\rangle = \hat{H}|\psi(t)\rangle. \tag{3.4}$$

This yields the equations of motion for the probability amplitudes

$$\dot{c}_1(t) = i\sum_k g_k^* c_k(t) \tag{3.5}$$

$$\dot{c}_k(t) = i\delta_k c_k(t) + ig_k c_i(t), \tag{3.6}$$

where $\delta_k = \omega_{\mathrm{q}} - \omega_k$ is the detuning of the qubit frequency from the frequency of $k^{\mathrm{th}}$ mode. At time $t = 0$, we place the qubit in the excited state, such that the system is in the initial state $|\psi(0)\rangle = |1,0_k\rangle$ (initial amplitudes $c_1(0) = 1$ and $c_k(0) = 0$). Formally integrating Eq. 3.6, we obtain

$$c_k(t) = ig_k\int_0^t c_1(t')e^{-i\delta_k(t-t')dt'} \tag{3.7}$$

which we then substitute into Eq. 3.5 to arrive at a differential equation that describes the evolution of $c_1(t)$,

$$\dot{c}_1(t) = -\sum_k |g_k|^2 \int_0^t c_1(t')e^{-i\delta_k(t-t')}dt' \tag{3.8}$$

To simplify this, we make a series of approximations. We assume that $c_1(t)$ varies slowly, so that we can set $c_1(t') = c_1(t)$ and pull it out of the time integral. Since we sum over all modes, we include all detunings $\delta_k$. The detunings are both positive, for modes with frequencies $\omega_k$ less than the qubit frequency $\omega$, and negative, for modes with frequencies $\omega_k$ greater than the qubit frequency $\omega$. After summing over all modes, the integral in Eq. 3.8 only survives when $t \approx t'$. This assumption implies that the continuum states impact system dynamics only locally in time. In other words, we can consider the continuum states to be a so-called "Markovian environment", which has the following conditions:

1. The 1D photonic continuum states in the waveguide are not significantly affected by their interaction with the qubit. The continuum states are time-independent/stationary.

2. The bandwidth of the continuum is much larger than the bandwidth of the qubit. The frequency range of the propagating modes in the waveguide is much broader than the qubit-waveguide coupling rate $\gamma$. In the time domain, this corresponds to environment dynamics that are much faster than the dynamics of the qubit-continuum interaction. As a result, the environment has no "memory" of its interaction with the qubit, which consequently renders these interactions irreversible.

Returning to our calculation, we implement a mathematical trick by working in the long-time limit: after summing over all detunings $\delta_k$, the integral in Eq. 3.8 is zero when $t \neq t'$, this enables us to integrate over all time. We take $t \to \infty$ and then use an identity from complex analysis,

$$\lim_{t\to\infty}\int_0^t e^{-i\delta_k(t-t')}dt' = \pi\delta(\delta_k) - P\left[\frac{1}{\delta_k}\right], \tag{3.9}$$

where $P\left[\frac{1}{\delta_k}\right]$ is the principal value taken when integrating over $\delta_k$, and $\delta$ is the Dirac delta function. We rewrite Eq. 3.8 as

$$\dot{c}_1(t) = -c_1(t)\left(\pi\sum_k |g_k|^2\delta(\delta_k) - i\sum_k |g_k|^2 P\left[\frac{1}{\delta_k}\right]\right). \tag{3.10}$$

We define the first term in Eq. 3.10 as $\frac{\gamma}{2} = \pi\sum_k |g_k|^2\delta(\delta_k)$, a real number, which is the decay rate of $c_1(t)$, corresponding to population decay from the excited state of the qubit into the available photonic modes. This expression is equivalent to Fermi's Golden Rule. The matrix element of the Hamiltonian that couples the states $|1, 0_k\rangle$ and $|0, k\rangle$ is $g_k = \langle 1, 0_k|\hat{H}|0, k\rangle$. The density of states into which the qubit can decay is $\sum_k \delta(\delta_k)$, as the qubit will only decay into modes near its frequency ($\delta_k = \omega - \omega_k \approx 0$). The second term in Eq. 3.10 corresponds to an energy shift known as the Lamb shift, $\Delta = \sum_k |g_k|^2 P\left[\frac{1}{\delta_k}\right]$, is a constant that can be incorporated into the problem by redefining the qubit frequency as $\tilde{\omega} = \omega + \Delta$. The solution to Eq. 3.10 is $c_1(t) = e^{-\gamma t/2 + i\Delta t}$ and the population of the qubit is,

$$\rho_{11}(t) = c_1^*(t)c_1(t) = e^{-\gamma t}. \tag{3.11}$$

In the long-time limit, the probability amplitudes of modes in the waveguide are

$$c_k(t) = \frac{i g_k e^{i\delta_k t}}{\gamma/2 + i\delta_k} \tag{3.12}$$

We interpret the resulting state of the fields in the waveguide as a photon wavepacket that is a superposition of continuum states $\sum_k c_k(t)|0, k\rangle$ that move away from the qubit. The modes with frequencies closest to the qubit frequency will have higher population after emission. Revisiting the assumption of Markovianity, when the qubit emits a photon into the 1D waveguide, the excitation is distributed amongst many

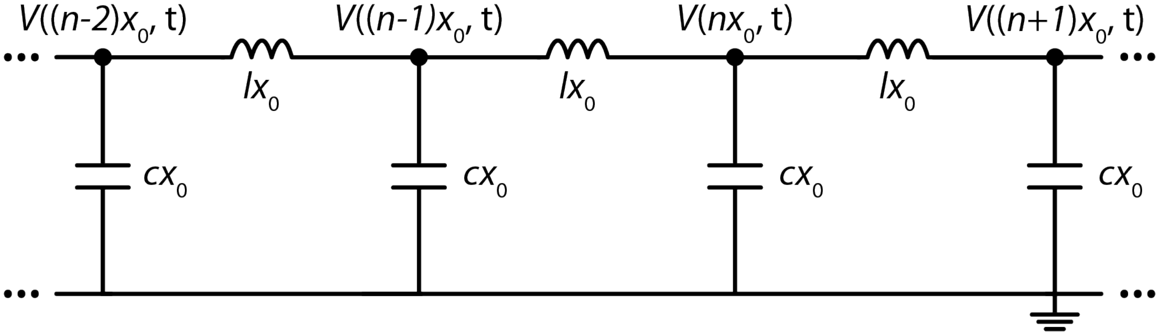

Figure 3-2: **Ideal lumped-element circuit model of an infinite transmission line.** We model the transmission line as a series of unit cells of lumped capacitors and inductors of length $x_0$ with capacitance per unit length $c$ and inductance per unit length $l$. We define time-dependent voltages $V(nx_0, t)$ at each circuit node.

modes. Because there is a quasicontinuum of modes, or in other words, the environment has a large bandwidth compared to the qubit decay rate, the information becomes scrambled, and we lose track of the initial excited state population. In this sense, this process is not time-reversible.

## 3.2 Classical Model: Qubit-Waveguide System

In the model outlined in Sec. 3.1, we stipulated that the qubit is coupled to a continuum of photonic modes in the 1D coplanar waveguide (transmission line). To demonstrate that modes of any frequency can propagate in the line in the ideal, lossless case, we use the lumped-element circuit model for the transmission line shown in Fig. 3-2. We divide the transmission line into small sections of length $x_0$. Each section has a total lumped capacitance $cx_0$ and total lumped inductance $lx_0$, where $c$ and $l$ are the capacitance and inductance per unit length of the transmission line, which are quantities defined by the geometry of the transmission line. First, using Kirchoff's Laws we relate the voltage of each node to the current through each lumped inductance with

$$V(nx_0, t) - V((n+1)x_0, t) = lx_0 \frac{\partial}{\partial t} I(nx_0, t) \tag{3.13}$$

We also relate the current through each lumped capacitance to the node voltage with

$$I(nx_0,t) - I((n+1)x_0,t) = cx_0 \frac{\partial}{\partial t} V(nx_0,t). \tag{3.14}$$

In the limit that $x_0$ approaches zero, we arrive at the telegrapher equations for a lossless transmission line

$$\begin{aligned} \frac{\partial}{\partial x} V(x,t) &= -l \frac{\partial}{\partial t} I(x,t) \\ \frac{\partial}{\partial x} I(x,t) &= -c \frac{\partial}{\partial t} V(x,t). \end{aligned} \tag{3.15}$$

In the Fourier domain, the telegrapher equations are

$$\begin{aligned} \frac{\partial}{\partial x} V(x,t) &= -j\omega l I(x,t) \\ \frac{\partial}{\partial x} I(x,t) &= -j\omega c V(x,t). \end{aligned} \tag{3.16}$$

Combining these equations, we derive 1D scalar wave equations for the voltage and current in an infinite lossless transmission line.

$$\begin{aligned} \left(\frac{\partial^2}{\partial x^2} + \omega^2 lc\right) V(x,t) = 0 \\ \left(\frac{\partial^2}{\partial x^2} + \omega^2 lc\right) I(x,t) = 0. \end{aligned} \tag{3.17}$$

We choose rightward-propagating plane wave solutions $V(k,w) = V_0 e^{-i(kx-\omega t)}$ and $I(k,w) = \frac{V_0}{Z_0} e^{-i(kx-\omega t)}$ without loss of generality, because they can be used in infinite series to construct arbitrary signals. The characteristic impedance of the line is given by $Z_0 = \sqrt{l/c}$. We derive the dispersion relation for the voltage and current waves to be $k^2 = \omega^2 lc$. The speed of these waves in the transmission line is $\nu = 1/\sqrt{lc}$. Note that $l$ and $c$ are fixed by the geometry of the transmission line. From the dispersion relation, a wave of any wavelength $\lambda = 2\pi/k$ can propagate in the waveguide. This falls in line with our model in Sec. 3.1, where we posited that the waveguide hosts a continuum of photonic modes. In other words, in the ideal case of no dielectric loss, the waveguide has infinite bandwidth. Next, we derive the scattering parameters

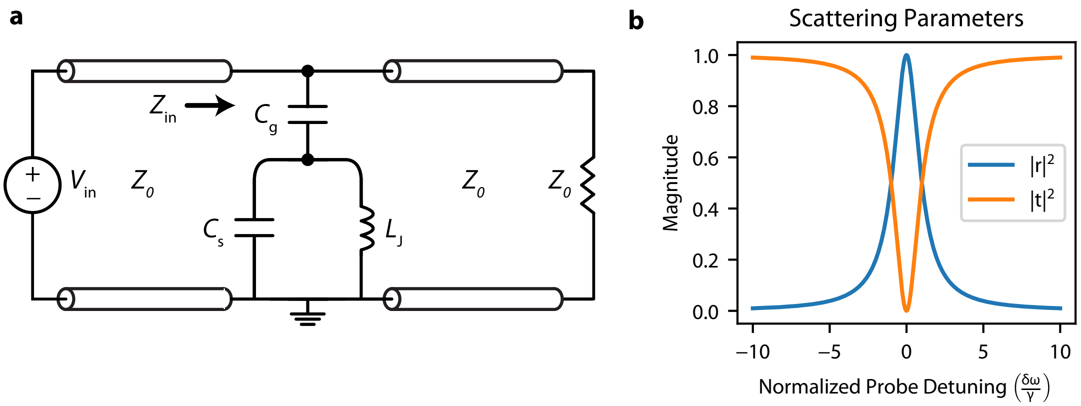

Figure 3-3: **Classical circuit model of qubit-waveguide system composed of a lumped element resonator coupled to a transmission line. a)** Circuit diagram of qubit coupled to transmission line with characteristic impedance of $Z_0$ through coupling capacitance $C_{\mathrm{g}}$. There is a voltage source $V_{\mathrm{in}}$ which sends a signal down the transmission line, which is terminated on the other end with a matched load. The qubit is modeled as a classical LC oscillator, with capacitance $C_{\mathrm{s}}$ and inductance $L_{\mathrm{J}}$. **b)** Transmission and reflection spectra of the circuit shown in (a).

of the qubit-waveguide system, namely reflection and transmission. Based off the approach taken in Ref. [43], we model the qubit as a classical LC circuit with a lumped element shunt capacitance of value $C_{\mathrm{s}}$ and inductance $L_{\mathrm{J}}$ in parallel. The LC circuit is coupled to the transmission line, now modeled as a continuous transmission line with effective impedance $Z_0$ with capacitance $C_{\mathrm{g}}$, as shown in Fig. 3-3.

We consider the coherent scattering of a incident coherent tone through the waveguide. We perform circuit analysis of the classical qubit-waveguide model to extract the modified qubit frequency and the strength of the qubit-waveguide coupling $\gamma$. We treat the circuit as a loaded parallel resonant circuit [44]. We first find the input impedance of the system

$$Z_{\mathrm{in}}(\omega) = Z_0 \;||\; \left( \frac{1}{j\omega C_{\mathrm{g}}} + \left( j\omega C_{\mathrm{s}} + \frac{1}{j\omega L_{\mathrm{J}}} \right)^{-1} \right), \tag{3.18}$$

which we can use to derive the reflection coefficient at the position of the qubit,

$$r = \frac{Z_{\mathrm{in}} - Z_0}{Z_{\mathrm{in}} + Z_0}, \tag{3.19}$$

On resonance, the input impedance of a parallel resonant circuit is maximized, while the input admittance is minimized. We set $\mathrm{Im}(Y_{\mathrm{in}}(\omega)) = 0$ to effectively minimize the input admittance, which yields the loaded resonance frequency of the system

$$\omega_{\mathrm{q}} = \frac{1}{\sqrt{L_{\mathrm{J}}(C_{\mathrm{s}} + C_{\mathrm{g}})}}. \tag{3.20}$$

We see that the coupling capacitance modifies the effective qubit resonance frequency. This can be interpreted as the classical explanation for the Lamb shift. The presence of the waveguide near the qubit loads the resonant circuit and shifts the resonance frequency from the bare frequency $1/\sqrt{L_{\mathrm{J}}C_{\mathrm{s}}}$. In the abstract quantum model, the coupling to a continuum of 1D modes shifts the qubit frequency. These are two sides of the same coin.

Next, we seek to derive $\gamma$ in terms of classical circuit parameters. Near the qubit frequency, the reflection and transmission parameters take the form

$$\begin{aligned} r &\approx \frac{1 - \frac{i\delta\omega}{\gamma}}{1 + \frac{\delta\omega^2}{\gamma^2}} \\ t &\approx 1 - \frac{1 - \frac{i\delta\omega}{\gamma}}{1 + \frac{\delta\omega^2}{\gamma^2}} \end{aligned} \tag{3.21}$$

where the qubit-tone detuning is $\delta\omega = \omega - \omega_{\mathrm{q}}$ and the qubit-waveguide coupling rate from the classical circuit model is

$$\gamma = \frac{\omega_{\mathrm{q}}^2 C_{\mathrm{g}}^2 Z_0}{4(C_{\mathrm{g}} + C_{\mathrm{s}})}. \tag{3.22}$$

We use this expression during the device design process, where we use classical microwave circuit simulators to extract parameters from the device geometry. The transmission and reflection spectra take the form of Lorentzian line-shapes. In the low input field power limit, we measure this transmission spectrum directly with a Vector Network Analyzer. The qubit behaves as a load on the transmission line that reflects input radiation near the qubit frequency.

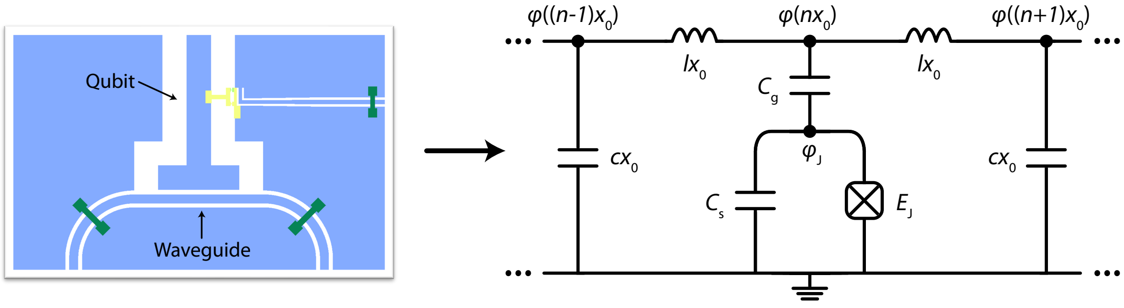

Figure 3-4: **Lumped-element circuit model of a transmon qubit coupled to an infinite transmission line.** We model the transmission line as a series of unit cells of capacitors and inductors of length $x_0$ with capacitance per unit length $c$ and inductance per unit length $l$. The transmon has shunt capacitance $C_{\mathrm{s}}$ and Josephson Energy $E_{\mathrm{J}}$. The transmon's capacitance to the transmission line is $C_{\mathrm{g}}$.

## 3.3 The waveguide QED Hamiltonian

Thus far, we have modeled a qubit coupled to a waveguide as an atom coupled to a continuum of available modes in the environment. This model abstracts the details of the system to help us understand the dynamics, but it is incomplete. From the abstract quantum model, we have derived general expressions for the decay rate of the qubit $\gamma$, which is a function of the single-mode Rabi frequency $g_k$. Then we focused more closely on the qubit-waveguide system and applied classical circuit analysis, and we observed the classical analog of the Lamb shift and arrived at an expression for the qubit-waveguide coupling rate $\gamma$. We also derived the transmission and reflection spectra of the classical model. We will take our analysis one step further by implementing a circuit quantization approach [37] to derive the wQED Hamiltonian, which describes a single transmon coupled to an infinite waveguide, following the discussion outlined in [45, 46].

In the circuit model presented in Fig. 3-4, we divide the transmission line of capacitance per unit length $c$ and inductance per unit length $l$ into $m$ unit cells. We couple the transmon qubit to the transmission line at the $n^{\text{th}}$ unit cell. We define a flux variable at each node, which is the time integral of the instantaneous voltage of the node referenced to ground $\phi(t) = \int_{-\infty}^{t} v(t')dt'$. We choose the flux variable to be position-like as we set up the Langrangian, which is the difference of the kinetic and potential energy of the system, $\mathcal{L} = E_{\text{kin}} - E_{\text{pot}}$. As the fluxes are the position-like variables, the inductive energy of the system will serve as the potential energy and the capacitive energy will serve as the kinetic energy. We write the Langrangian for the qubit-waveguide system,

$$\begin{aligned}\mathcal{L} = \frac{1}{2}C_{\text{s}}\dot{\phi}_{\text{J}}^2 + \sum_m \frac{1}{2}cx_0\dot{\phi}(mx_0)^2 + \frac{1}{2}C_{\text{g}}(\dot{\phi}(nx_0) - \dot{\phi}_{\text{J}})^2 \\ +E_{\text{J}}\cos\frac{2\pi\phi_{\text{J}}}{\phi_0} - \sum_m \frac{1}{2lx_0}(\phi((m+1)x_0) - \phi(mx_0))^2\end{aligned} \tag{3.23}$$

and find the charge (momentum-like) conjugate variables using $q_k = \frac{\partial \mathcal{L}}{\partial \dot{\phi}_k}$.

$$\begin{aligned}q(nx_0) &= C_{\text{g}}(\dot{\phi}(nx_0) - \dot{\phi}_{\text{J}}) + cx_0\dot{\phi}(nx_0) \\ q(mx_0) &= cx_0\dot{\phi}(mx_0) \\ q_{\text{J}} &= C_{\text{s}}\dot{\phi}_{\text{J}} - C_{\text{g}}(\dot{\phi}(nx_0) - \dot{\phi}_{\text{J}})\end{aligned} \tag{3.24}$$

We construct the classical Hamiltonian of the system from the Lagrangian using

$$H = \sum_m q(mx_0)\dot{\phi}(mx_0) + q(nx_0)\dot{\phi}(nx_0) + q_{\text{J}}\dot{\phi}_{\text{J}} - \mathcal{L}. \tag{3.25}$$

We aim to write the quantum Hamiltonian of the system as the sum of the transmon Hamiltonian, the transmission line Hamiltonian, and the interaction Hamiltonian,

$$\hat{H} = \hat{H}_{\text{J}} + \hat{H}_{\text{TX}} + \hat{H}_{\text{int}} \tag{3.26}$$

First, we approximate the transmon qubit as an ideal two-level system with the free-transmon Hamiltonian from Eq. 2.13,

$$\hat{H}_{\text{J}} = \frac{\hbar\omega_{\text{q}}}{2}\hat{\sigma}_z. \tag{3.27}$$

where the qubit frequency is defined as $\omega_{\text{q}} = (\sqrt{8E_{\text{J}}E_{\text{C}}} - E_{\text{C}})/\hbar$. The charging energy is modified by the coupling to the transmission line

$$E_{\mathrm{C}} = \frac{e^2}{2C_{\mathrm{J}}} = \frac{e^2(C_{\mathrm{g}} + cd)}{2[cd(C_{\mathrm{g}} + C_{\mathrm{s}}) + C_{\mathrm{g}}C_{\mathrm{s}}]}. \tag{3.28}$$

Next, we study the transmission line Hamiltonian,

$$\hat{H}_{\mathrm{TX}} = \sum_m x_0 \left[ \frac{q(mx_0)^2}{2c_{\mathrm{TX}}(mx_0)} + \frac{1}{2l} \left( \frac{\phi((m+1)x_0) - \phi(mx_0)}{x_0} \right)^2 \right], \tag{3.29}$$

where we define the effective transmission line capacitance per unit length

$$c_{\mathrm{TX}}(mx_0) = c + \frac{C_{\mathrm{g}}C_{\mathrm{s}}}{(C_{\mathrm{g}} + C_{\mathrm{s}})} \frac{\delta_{nm}}{x_0}. \tag{3.30}$$

Since $q(mx_0)$ and $\phi(mx_0)$ are conjugate variables, we can promote them to quantum operators ($q(mx_0) \to \hat{q}(mx_0)$, $\phi(mx_0) \to \hat{\phi}(mx_0)$) with the commutator

$$[\hat{\phi}(mx_0), \hat{q}(m'x_0)] = i\hbar\delta_{mm'}. \tag{3.31}$$

We move from a lumped-element to a distributed circuit model through the assumption that $x_0$ and the effective qubit length $d$ are much smaller than the wavelength of the modes of interest in the waveguide, which are those near the qubit frequency. To work in the continuum limit, we take $x_0 \to 0$, and the Hamiltonian for the transmission line becomes

$$\hat{H}_{\mathrm{TX}} = \int_{-\infty}^{\infty} dx \left[ \frac{\hat{q}(x)^2}{2c_{\mathrm{TX}}(x)} + \frac{1}{2l} \left( \frac{\partial\hat{\phi}(x)}{\partial x} \right)^2 \right], \tag{3.32}$$

and

$$c_{\mathrm{TX}}(x) = c + \frac{C_{\mathrm{g}}C_{\mathrm{s}}}{(C_{\mathrm{g}} + C_{\mathrm{s}})} \delta(x - x_{\mathrm{J}}) \tag{3.33}$$

where the position of the center of the qubit is $x_{\mathrm{J}}$. As argued in [45], we treat the qubit and coupling capacitances as small perturbations to the total capacitance $cL$ of the transmission line of length L and approximate $c_{\mathrm{TX}}(x) \approx c$.

The discrete-valued charge and flux operators are now continuous operators $\hat{q}(x)$ and $\hat{\phi}(x)$. The commutator $[\hat{\phi}(mx_0), \hat{q}(m'x_0)] = [\hat{\phi}(mx_0), cx_0\dot{\hat{\phi}}(m'x_0)] = i\hbar\delta_{mm'}$ becomes

$$\lim_{x_0 \to 0}\left([\hat{\phi}(mx_0), c\dot{\hat{\phi}}(m'x_0)] = \frac{i\hbar\delta_{mm'}}{x_0}\right) \tag{3.34}$$

$$[\hat{\phi}(x), \hat{q}(x')] = i\hbar\delta(x - x') \tag{3.35}$$

where the continuous charge density operator is $\hat{q}(x) = c\dot{\hat{\phi}}(x)$.

Next, we work in Fourier space,

$$\begin{aligned} \hat{\phi}(x) &= \int_{-\infty}^{\infty} \frac{dk}{\sqrt{2\pi}} \hat{\phi}(k) e^{ikx} \\ \hat{q}(x) &= \int_{-\infty}^{\infty} \frac{dk}{\sqrt{2\pi}} \hat{q}(k) e^{ikx} \end{aligned} \tag{3.36}$$

We take the derivative of the flux variable with respect to position,

$$\frac{\partial\hat{\phi}(x)}{\partial x} = \int_{-\infty}^{\infty} \frac{dk}{\sqrt{2\pi}} ik\hat{\phi}(k) e^{ikx} \tag{3.37}$$

which we substitute into Eq. 3.32,

$$\hat{H}_{\text{TX}} = \int_{-\infty}^{\infty} dk \int_{-\infty}^{\infty} dk' \int_{-\infty}^{\infty} \frac{dx}{2\pi} e^{i(k+k')x} \left[\frac{1}{2c}\hat{q}(k)\hat{q}(k') - \frac{kk'}{2l}\hat{\phi}(k)\hat{\phi}(k')\right]. \tag{3.38}$$

Using the identity $2\pi\delta(k) = \int_{-\infty}^{\infty} dx e^{ikx}$,

$$\hat{H}_{\text{TX}} = \int_{-\infty}^{\infty} dk \int_{-\infty}^{\infty} dk' \delta(k + k') \left[\frac{1}{2c}\hat{q}(k)\hat{q}(k') - \frac{kk'}{2l}\hat{\phi}(k)\hat{\phi}(k')\right]. \tag{3.39}$$

Next, we integrate with respect to $k'$, and integrating over $\delta(k+k')$ results in equating $k' = -k$. We note that $\hat{\phi}(x)$ and $\hat{q}(x)$ are real functions, whose Fourier pairs obey the relation $\hat{\phi}(-k) = \hat{\phi}^*(k)$ and $\hat{q}(-k) = \hat{q}^*(k)$.

$$\hat{H}_{\text{TX}} = \int_{-\infty}^{\infty} dk \left[\frac{|\hat{q}(k)|^2}{2c} + \frac{k^2|\hat{\phi}(k)|^2}{2l}\right]. \tag{3.40}$$

This is the Hamiltonian of a set of simple quantum harmonic oscillators. In the analogy, the mass quantity is the capacitance per unit length $c$, and the frequency of each oscillator is $\omega_k = \frac{k}{\sqrt{lc}}$. This can be interpreted as a continuum of electromagnetic waves in the transmission line propagating at speed $\nu = 1/\sqrt{lc}$. Using second quantization, we write the operators $\hat{q}(k)$ and $\hat{\phi}(k)$ in terms of creation and annihilation operators

$$\begin{aligned} \hat{\phi}(k) &= \sqrt{\frac{\hbar Z_0}{2k}}(\hat{a}^\dagger(-k) + \hat{a}(k)) \\ \hat{q}(k) &= i\sqrt{\frac{\hbar k}{2Z_0}}(\hat{a}^\dagger(-k) - \hat{a}(k)) \end{aligned} \tag{3.41}$$

where $Z_0 = \sqrt{\frac{l}{c}}$ is the characteristic impedance of the transmission line. We rewrite the transmission line Hamiltonian in the eigenbasis of the quantum Harmonic oscillator,

$$\hat{H}_{\mathrm{TX}} = \int_{-\infty}^{\infty} dk \frac{\hbar\omega_k}{2}(\hat{a}^\dagger(k)\hat{a}(k) + a^\dagger(-k)\hat{a}(-k)). \tag{3.42}$$

In the literature, it is common to distinguish leftward and rightward propagating modes to prepare for an input-output theory-style analysis of the system [45–47]. We implement this by using positive wave numbers only, and we write the transmission line Hamiltonian as

$$\hat{H}_{\mathrm{TX}} = \int_{0}^{\infty} dk \hbar\omega_k(\hat{a}^\dagger_{\mathrm{L}}(k)\hat{a}_{\mathrm{L}}(k) + \hat{a}^\dagger_{\mathrm{R}}(k)\hat{a}_{\mathrm{R}}(k)). \tag{3.43}$$

Alternatively, we define the operators as a function of the harmonic oscillator frequency $\omega$.

$$\begin{aligned} \hat{\phi}(\omega) &= \sqrt{\frac{\hbar}{2\omega c}}(\hat{a}^\dagger(-\omega) + \hat{a}(\omega)) \\ \hat{q}(\omega) &= i\sqrt{\frac{\hbar\omega c}{2}}(\hat{a}^\dagger(-\omega) - \hat{a}(\omega)) \end{aligned} \tag{3.44}$$

which leads to an equivalent transmission line Hamiltonian,

$$\hat{H}_{\mathrm{TX}} = \int_{0}^{\infty} d\omega \hbar\omega(\hat{a}^\dagger_{\mathrm{L}}(\omega)\hat{a}_{\mathrm{L}}(\omega) + a^\dagger_{\mathrm{R}}(\omega)\hat{a}_{\mathrm{R}}(\omega)). \tag{3.45}$$

We take the Fourier transform to obtain the charge density and flux operators as a function of position,

$$\begin{aligned}\hat{\phi}(x) &= \sqrt{\frac{\hbar}{4\pi c}}\int_{-\infty}^{\infty}\frac{dk}{\sqrt{\omega_k}}(\hat{a}_{-k}^{\dagger}+\hat{a}_k)e^{ikx} = \sqrt{\frac{\hbar Z_0}{4\pi}}\int_{-\infty}^{\infty}\frac{d\omega}{\sqrt{\omega}}(\hat{a}_{\omega}^{\dagger}e^{-i\frac{\omega x}{\nu}}+\hat{a}_{\omega}e^{i\frac{\omega x}{\nu}}) \\ \hat{q}(x) &= i\sqrt{\frac{\hbar c}{4\pi}}\int_{-\infty}^{\infty}dk\sqrt{\omega_k}(\hat{a}_{-k}^{\dagger}-\hat{a}_k)e^{ikx} = i\sqrt{\frac{\hbar Z_0 c^2}{4\pi}}\int_{-\infty}^{\infty}d\omega\sqrt{\omega}(\hat{a}_{\omega}^{\dagger}e^{-i\frac{\omega x}{\nu}}-\hat{a}_{\omega}e^{i\frac{\omega x}{\nu}}).\end{aligned} \tag{3.46}$$

Finally, returning to the assembly of the Hamiltonian of the qubit-waveguide system initiated in Eq. 3.26, we write the interaction Hamiltonian in terms of the defined quantum operators,

$$\hat{H}_{\text{int}} = \int_{-\infty}^{\infty} d\omega i\hbar g(\omega)\hat{\sigma}_y(\hat{a}_{\omega}e^{i\frac{\omega x_{\text{J}}}{\nu}} - \hat{a}_{\omega}^{\dagger}e^{-i\frac{\omega x_{\text{J}}}{\nu}}) \tag{3.47}$$

where we define the effective coupling capacitance per unit length

$$c_{\text{g}} = \frac{cd(C_{\text{g}}+C_{\text{s}})+C_{\text{g}}C_{\text{s}}}{C_{\text{g}}d} \tag{3.48}$$

and the single-mode coupling rate

$$g(\omega) = \sqrt{\frac{\omega Z_0 e^2 c^2}{2\pi\hbar c_{\text{g}}^2}}\left(\frac{E_{\text{J}}}{8E_{\text{C}}}\right)^{\frac{1}{4}}. \tag{3.49}$$

Finally, we arrive at the the waveguide QED Hamiltonian, derived from the circuit quantization of a transmon qubit coupled to a coplanar waveguide,

$$\frac{\hat{H}}{\hbar} = \frac{\omega_{\text{q}}}{2}\hat{\sigma}_z + \int_{-\infty}^{\infty} d\omega\left(\omega\hat{a}_{\omega}^{\dagger}\hat{a}_{\omega} + ig(\omega)\hat{\sigma}_y(\hat{a}_{\omega}^{\dagger}e^{-i\frac{\omega x}{\nu}} - \hat{a}_{\omega}e^{i\frac{\omega x}{\nu}}\right). \tag{3.50}$$

This Hamiltonian maps directly to the abstract Hamiltonian in Eq. 3.2, which describes a two-level system coupled to a 1D continuum of propagating modes. Distinguishing between leftward and rightward propagating modes in the waveguide and using the rotating wave approximation, the waveguide QED Hamiltonian is

$$\begin{aligned}\frac{\hat{H}}{\hbar} = \frac{\omega_{\mathrm{q}}}{2}\hat{\sigma}_z + \int_0^\infty & d\omega[\omega(\hat{a}^\dagger_{\mathrm{L}}(\omega)\hat{a}_{\mathrm{L}}(\omega) + \hat{a}^\dagger_{\mathrm{R}}(\omega)\hat{a}_{\mathrm{R}}(\omega)) + \\ & g(\omega)(\hat{\sigma}^+\hat{a}_{\mathrm{R}}(\omega)e^{i\frac{\omega x_{\mathrm{J}}}{\nu}} + \hat{\sigma}^-\hat{a}^\dagger_{\mathrm{L}}(\omega)e^{-i\frac{\omega x_{\mathrm{J}}}{\nu}} + h.c.)].\end{aligned} \tag{3.51}$$

We revist the key parameters of the analysis of this Hamiltonian in the Sec. 3.2, the Rabi frequency $g_k$, the decay rate $\gamma$. Following Fermi's Golden Rule, the decay rate $\gamma$ of the qubit population into the waveguide modes depends on the density of states in the waveguide and the coupling rate $g(\omega)$,

$$\gamma = 2\pi\int_{-\infty}^{\infty} d\omega |g(\omega)|^2 \delta(\omega - \omega_{\mathrm{q}}) = \frac{\omega_{\mathrm{q}} e^2 Z_0}{\hbar}\left(\frac{c}{c_{\mathrm{g}}}\right)^2 \left(\frac{E_{\mathrm{J}}}{8E_{\mathrm{C}}}\right)^{\frac{1}{2}}. \tag{3.52}$$

Note that we are working in the continuum limit of modes in the waveguide. We have arrived at an expression for $\gamma$ in terms of circuit parameters. Through circuit quantization of the qubit-waveguide system, we have filled in more details of the quantum model of a single qubit coupled to a waveguide.

## 3.4 Input-Output Theory

We have derived the waveguide QED Hamiltonian, which governs the dynamics of a single qubit coupled to the 1D continuum of modes in the waveguide. Our next goal is to adopt the input-output theory formalism in order to define a relationship between the qubit and propagating fields in the waveguide. This is a preliminary step towards determining the scattering spectra of the qubit-waveguide system. We use the Hamiltonian in Eq. 3.51 and move to the Heisenberg picture to obtain the evolution of the rightward-propagating field operator $\hat{a}_{\mathrm{R}}(\omega)$

$$\frac{d\hat{a}_{\mathrm{R}}(\omega)}{dt} = \frac{1}{i\hbar}[\hat{a}_{\mathrm{R}}(\omega), \hat{H}] = -i\omega\hat{a}_{\mathrm{R}}(\omega) - ig(\omega)\hat{\sigma}^- e^{-i\frac{\omega x_{\mathrm{J}}}{\nu}}. \tag{3.53}$$

Next, through formal integration, the evolution equation becomes

$$\hat{a}_{\mathrm{R}}(\omega,t)e^{i\omega t} = -ig(\omega)\int_{-\infty}^{t}\hat{\sigma}^{-}(t')e^{i\omega(t'-t_0)}dt' \tag{3.54}$$

where we define $t_0 = x_{\mathrm{J}}/\nu$ as a time delay determined by the position of the qubit. We choose time $t = 0$ to be the time at which the qubit begins to interact with the initial field in the waveguide $\hat{a}_{\mathrm{R}}(\omega, 0)$,

$$\hat{a}_{\mathrm{R}}(\omega,t) = \hat{a}_{\mathrm{R}}(\omega,0)e^{-i\omega t} - ig(\omega)\int_{0}^{t}\hat{\sigma}^{-}(t')e^{i\omega(t'-t-t_0)}dt' \tag{3.55}$$

In order to define the time boundary conditions of the input-output relation, we also redefine this equation in terms of a final time $t_f > t$ after the qubit-waveguide interaction

$$\hat{a}_{\mathrm{R}}(\omega,t) = \hat{a}_{\mathrm{R}}(\omega,t_f)e^{-i\omega t} + ig(\omega)\int_{t}^{t_f}\hat{\sigma}^{-}(t')e^{i\omega(t'-t-t_0)}dt'. \tag{3.56}$$

We define the input and output field as functions of time respectively with Fourier transforms

$$\begin{aligned}\hat{a}_{\mathrm{R}}^{\mathrm{in}}(t) &= \int_{0}^{\infty}\frac{d\omega}{\sqrt{2\pi}}\hat{a}_{\mathrm{R}}(\omega,0)e^{-i\omega t}\\ \hat{a}_{\mathrm{R}}^{\mathrm{out}}(t) &= \int_{0}^{\infty}\frac{d\omega}{\sqrt{2\pi}}\hat{a}_{\mathrm{R}}(\omega,t_f)e^{-i\omega t}\end{aligned} \tag{3.57}$$

We set Eq. 3.55 equal to Eq. 3.56 and integrate over $\omega$,

$$\hat{a}_{\mathrm{R}}^{\mathrm{out}}(t) = \hat{a}_{\mathrm{R}}^{\mathrm{in}}(t) - \int_{0}^{\infty}\frac{d\omega}{\sqrt{2\pi}}ig(\omega)\int_{0}^{t_f}\hat{\sigma}^{-}(t')e^{i\omega(t'-t-t_0)}dt'. \tag{3.58}$$

We observe that $g(\omega) \propto \sqrt{\omega}$, which means that higher frequencies will contribute the most to the integral. However, at high frequencies, the integrand oscillates quickly and the contribution of higher frequencies will average to zero. The only time at which the integrand is not an oscillatory function is at $t' = t$. At times $|t' - t| \ll 1/g(\omega)$, we make the approximation that the qubit is evolving freely, i.e. $\hat{\sigma}^{-}(t') \approx \hat{\sigma}^{-}(t)e^{-i\omega_{\mathrm{q}}(t'-t)}$.

Here, we neglect the interaction term of the waveguide QED Hamiltonian in Eq. 3.51. At this time scale, the coupling rate is much slower than the qubit frequency, and we proceed as if the qubit is not coupled to the waveguide at all. This is an implementation of the Markov approximation, see [45] for more details. If $\omega_\mathrm{q} t \gg 1$, we are integrating over many periods of evolution, so we can take the long-time limit $\omega_\mathrm{q} t \to \infty$ [45]. With these simplifications, we have

$$\hat{a}_\mathrm{R}^\mathrm{out}(t) = \hat{a}_\mathrm{R}^\mathrm{in}(t) - i\hat{\sigma}^-(t) \int_0^\infty \frac{d\omega}{\sqrt{2\pi}} g(\omega) e^{-i\omega t_0} \int_0^\infty e^{i(\omega-\omega_\mathrm{q})(t'-t)} dt'. \tag{3.59}$$

Using the identity given in Eq. 3.9, we simplify

$$\hat{a}_\mathrm{R}^\mathrm{out}(t) = \hat{a}_\mathrm{R}^\mathrm{in}(t) - i\hat{\sigma}^-(t) \int_0^\infty \frac{d\omega\sqrt{\pi}}{\sqrt{2}} g(\omega) e^{-i\omega t_0} \delta(\omega - \omega_\mathrm{q}). \tag{3.60}$$

Finally, we arrive at the input-output relations for the qubit coupled to the waveguide. The same analysis for a leftward-propagating field yields a similar expression.

$$\begin{aligned} \hat{a}_\mathrm{R}^\mathrm{out}(t) &= \hat{a}_\mathrm{R}^\mathrm{in}(t) - i\sqrt{\frac{\gamma}{2}} \hat{\sigma}^-(t) e^{-i\frac{\omega_\mathrm{q} x_\mathrm{J}}{\nu}} \\ \hat{a}_\mathrm{L}^\mathrm{out}(t) &= \hat{a}_\mathrm{L}^\mathrm{in}(t) - i\sqrt{\frac{\gamma}{2}} \hat{\sigma}^-(t) e^{i\frac{\omega_\mathrm{q} x_\mathrm{J}}{\nu}}. \end{aligned} \tag{3.61}$$

Alternatively, we will use an equivalent expression where we remove the $-i$ phase in front of the qubit operators. This would imply that during the second quantization of the fields in the waveguide, we chose the charge density operator $\hat{q}(x)$ to be the position-like variable instead of the momentum-like variable, which would result in a $-i$ phase in the single-mode coupling $g(\omega)$ in Eq. 3.49. This choice does not alter the system dynamics. Equivalently, we write the input-output relations for a qubit coupled to a bidirectional waveguide,

$$\begin{aligned} \hat{a}_\mathrm{R}^\mathrm{out}(t) &= \hat{a}_\mathrm{R}^\mathrm{in}(t) + \sqrt{\frac{\gamma}{2}} \hat{\sigma}^-(t) e^{-i\frac{\omega_\mathrm{q} x_\mathrm{J}}{\nu}} \\ \hat{a}_\mathrm{L}^\mathrm{out}(t) &= \hat{a}_\mathrm{L}^\mathrm{in}(t) + \sqrt{\frac{\gamma}{2}} \hat{\sigma}^-(t) e^{i\frac{\omega_\mathrm{q} x_\mathrm{J}}{\nu}}. \end{aligned} \tag{3.62}$$

For the single qubit case, this position parameter $x_\mathrm{J}$ is an arbitrary reference point in a waveguide of effectively infinite length, but will prove important in Chapter 4 in the discussion of the collective effects of multiple qubits coupled to a common waveguide. These equations describe the relationship between the qubit and field amplitudes in the waveguide. We can use them to inject an input field through the waveguide and determine the output field after the qubit-waveguide interaction. We see from these relations that when a qubit emits a photon into the waveguide, on average, the photon will propagate to the right or left with equal probability.

## 3.5 Qubit as a Single Photon Mirror

Now that we have established a model for the quantum dynamics of the qubit-waveguide system, we see that coupling the qubit to the continuum of 1D modes serves as a mechanism of population decay through spontaneous emission at rate $\gamma$. Our next goal is to use the quantum qubit-waveguide model to derive the transmission and reflection spectra of a coherent tone incident on the qubit through the waveguide. By assuming the 1D continuum of modes is a Markovian environment, we can utilize the master-equation formalism for the qubit-waveguide system. A more detailed derivation of a general master equation for qubit-waveguide systems can be found in Sec. 4.2. We assume we are in the strong-coupling regime, where the qubit is more strongly coupled to the waveguide than to any other decay channel in the environment. In other words, the qubit-waveguide coupling rate $\gamma \gg \gamma_\mathrm{nr}$, the non-radiative decay, which we will neglect in this analysis. We add a few more ingredients to our model: a coherent tone in the waveguide incident upon the qubit, the presence of thermal photons, and qubit dephasing, following [48]. The Hamiltonian of the system is the sum of the qubit energy and the coupling to the coherent field in the rotating frame of the qubit,

$$\frac{\hat{H}_\mathrm{q}}{\hbar} = -\frac{\delta}{2}\hat{\sigma}_z + \frac{\Omega_\mathrm{p}}{2}\hat{\sigma}_x, \tag{3.63}$$

where $\omega_\mathrm{p}$ is the input field frequency, $\delta = \omega_\mathrm{p} - \omega_\mathrm{q}$ is the qubit-tone detuning, and $\Omega_\mathrm{p}$ is the Rabi frequency of the coherent tone that probes the qubit. The tone is coherent, producing a field corresponding to that of a classical oscillating dipole [42]. Therefore, the expression for the Rabi frequency is [45]

$$\Omega_{\mathrm{p}} = -2i\langle \hat{a}_{\mathrm{in}} \rangle \sqrt{\frac{\gamma}{2}}, \tag{3.64}$$

where $\hat{a}_{\mathrm{in}}$ corresponds to the coherent input field amplitude. We assume we send a rightward-propagating coherent tone through the waveguide. We also know that the average input field amplitude $\langle \hat{a}_{\mathrm{in}} \rangle = \sqrt{\frac{P}{\hbar\omega_{\mathrm{d}}}}$, where $P$ is the input power, which is obtained from an average power calculation using the charge and flux variables [49]. This allows us to relate the resonant input power to the Rabi frequency

$$\Omega_{\mathrm{p}} = -i\sqrt{\frac{2\gamma P}{\hbar\omega_{\mathrm{q}}}} \tag{3.65}$$

The master-equation that describes the dynamics of the driven qubit coupled to a waveguide is

$$\partial_t \hat{\rho} = \frac{1}{i\hbar}\left[\hat{H}_{\mathrm{q}}, \hat{\rho}\right] + (\bar{n}_{\mathrm{th}} + 1)\gamma D\left[\hat{\sigma}^-\right]\hat{\rho} + \bar{n}_{\mathrm{th}}\gamma D\left[\hat{\sigma}^+\right]\hat{\rho} + \frac{\gamma_\phi}{2} D\left[\hat{\sigma}_z\right]\hat{\rho}, \tag{3.66}$$

where $\rho$ is the density matrix operator of the qubit and $D[\hat{O}] = \hat{O}\hat{\rho}\hat{O}^\dagger - \frac{1}{2}\{\hat{O}^\dagger\hat{O}, \hat{\rho}\}$ is the Lindblad dissipator. The qubit is coupled to a thermal bath of photons present in the waveguide, with temperature $T$ and average photon number $\bar{n}_{\mathrm{th}} = 1/(e^{\frac{\hbar\omega_{\mathrm{q}}}{k_{\mathrm{B}}T}} - 1)$. The pure dephasing rate is denoted by $\gamma_\phi$. There are four processes that contribute to the system dynamics:

1. **Coherent drive** at rate $\Omega_{\mathrm{p}}$ – population transfer between the ground and excited state of the qubit.

2. **Spontaneous emission** at rate $\gamma$ – population decay from the excited state to the photonic modes in the waveguide.

3. **Thermal excitation** at rate $\gamma\bar{n}_{\mathrm{th}}$ – incoherent transitions between the ground and excited states of the qubit in both directions.

4. **Pure dephasing** at rate $\gamma_\phi$ – ambient noise processes decrease the coherences of the density matrix (off-diagonal elements) without affecting populations.

These processes compete with each other, and the resulting system dynamics will depend on their interplay. More precisely, we yield four differential equations for the elements of the qubit's density matrix, $\langle i|\hat{\rho}|j\rangle = \rho_{ij}$, and these are known as the optical Bloch equations

$$\begin{aligned}
\dot{\rho}_{11} &= -\gamma(\bar{n}_{\mathrm{th}}+1)\rho_{11} + \gamma\bar{n}_{\mathrm{th}}\rho_{00} + \frac{i\Omega_{\mathrm{p}}}{2}(\rho_{10}-\rho_{01}) \\
\dot{\rho}_{00} &= \gamma(\bar{n}_{\mathrm{th}}+1)\rho_{00} - \gamma\bar{n}_{\mathrm{th}}\rho_{11} - \frac{i\Omega_{\mathrm{p}}}{2}(\rho_{10}-\rho_{01}) \\
\dot{\rho}_{10} &= [i\delta - \frac{\gamma}{2}(2\bar{n}_{\mathrm{th}}+1) - \gamma_\phi]\rho_{10} + \frac{i\Omega_{\mathrm{p}}}{2}(\rho_{11}-\rho_{00}) \\
\dot{\rho}_{01} &= [-i\delta - \frac{\gamma}{2}(2\bar{n}_{\mathrm{th}}+1) - \gamma_\phi]\rho_{01} - \frac{i\Omega_{\mathrm{p}}}{2}(\rho_{11}-\rho_{00})
\end{aligned} \tag{3.67}$$

Note that only two of these equations are independent, because conservation of probability dictates $\rho_{00} + \rho_{11} = 1$ and the hermiticity of the density matrix requires $\rho_{01} = \rho_{10}^*$. We also define a thermally enhanced decay and dephasing rate, $\gamma_1^{\mathrm{th}} = (2\bar{n}_{\mathrm{th}}+1)\gamma$ and $\gamma_2^{\mathrm{th}} = \gamma_1^{\mathrm{th}}/2 + \gamma_\phi$. We are concerned with the steady state solution of the system dynamics, $\dot{\hat{\rho}} = 0$. This is justified because we will be applying the coherent drive for an undefined amount of time, and our goal is to determine the frequency response of the system from the quantum model. We are interested in the steady state coherence of the qubit

$$\rho_{10} = \frac{-i\Omega_{\mathrm{p}}(1+\delta/\gamma_2^{\mathrm{th}})}{2\gamma_2^{\mathrm{th}}(2\bar{n}_{\mathrm{th}}+1)[1+(\delta/\gamma_2^{\mathrm{th}})^2 + \Omega_{\mathrm{p}}^2/(\gamma_1^{\mathrm{th}}\gamma_2^{\mathrm{th}})]}. \tag{3.68}$$

This coherence $\rho_{01} \equiv \langle\hat{\sigma}^-\rangle$ is the key ingredient in using input-output theory to relate the qubit and field steady state dynamics. We invoke the following input-output relation for a specified field frequency $\omega$, setting the qubit position $x_{\mathrm{J}} = 0$

$$\langle\hat{a}_{\mathrm{out}}\rangle = \langle\hat{a}_{\mathrm{in}}\rangle + \sqrt{\frac{\gamma}{2}}\langle\hat{\sigma}^-\rangle. \tag{3.69}$$

We can use the input-output relations to relate the input tone to the output field after interaction with the qubit. The scattering parameters of the system, transmissivity $t$ (or $S_{21}$) and reflectivity $r = 1 - t$ (or $S_{11}$) through the qubit-waveguide system are defined as

$$\begin{aligned} t &= \frac{\langle \hat{a}_{\text{out}} \rangle}{\langle \hat{a}_{\text{in}} \rangle} \\ r &= 1 - \frac{\langle \hat{a}_{\text{out}} \rangle}{\langle \hat{a}_{\text{in}} \rangle} \end{aligned} \tag{3.70}$$

Finally, we can study the scattering parameters as a function of the coherent tone detuning, or in other words, we have derived the frequency response of the qubit-waveguide system

$$t(\delta) = 1 - \frac{\gamma(1 + i\delta/\gamma_2^{\text{th}})}{2\gamma_2^{\text{th}}(2\bar{n}_{\text{th}} + 1)[1 + (\delta/\gamma_2^{\text{th}})^2 + \Omega_{\text{p}}^2/(\gamma_1^{\text{th}}\gamma_2^{\text{th}})]}. \tag{3.71}$$

The transmission spectrum $|t(\delta)|^2$ takes the shape of a Lorentzian, which was also the case for the spectrum derived from the classical circuit model in Eq. 3.21. The transmission depends on the interplay of competing processes: a coherent drive, spontaneous emission, thermal excitations, and pure dephasing. These parameters are key to understanding the system behavior, and we can extract them with a simple transmission scan with a Vector Network Analyzer (VNA).

We send a coherent tone through the waveguide with the VNA and sweep the frequency of this tone near the qubit frequency. From this transmission curve, we extract the qubit-waveguide coupling rate $\gamma$, the qubit's pure dephasing rate $\gamma_\phi$, and the temperature of the waveguide from $\bar{n}_{\text{th}}$. We must operate in the low field power limit, such that the average photon number $|\alpha| << 1$. This enables us consider the interaction of the qubit with a single photon. We can track all of the energy we put into the system with the coherent tone ($|r|^2 + |t|^2 = 1$), otherwise known as elastic scattering.

Fig. 3-5a depicts the steady-state quantum interference effect of the probed qubit-waveguide system. The coherent tone propagates to the right in the waveguide and

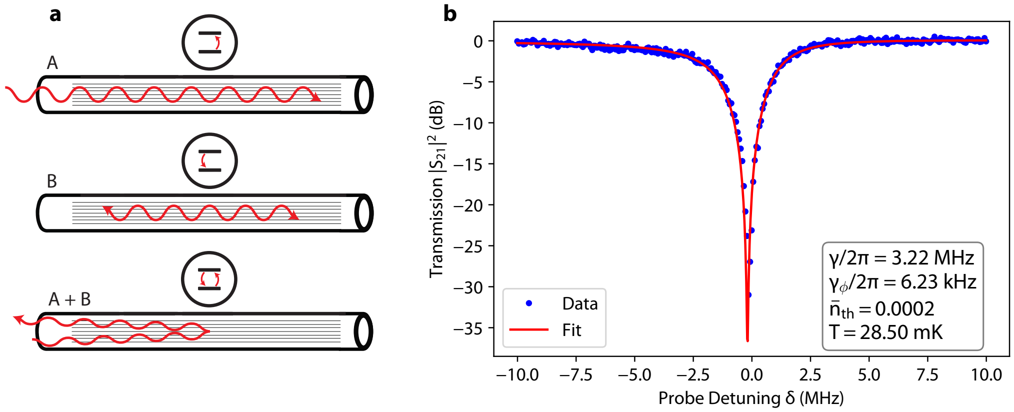

Figure 3-5: **Steady-state interference effect of a qubit driven by a low-power coherent tone in a waveguide.** a) **A** shows the coherent tone propagating to the right, which excites the qubit. **B** shows the qubit decaying into the waveguide. The emission travels in either direction with equal probability. **A** + **B** shows the sum of the excitation and emission events. The coherent tone excites the qubit, and the resulting qubit rightward emission is completely out of phase with the coherent tone. This results in complete destructive interference in the rightward direction, which explains the extinction in transmission at the qubit frequency. b) Transmission data of a qubit-waveguide system. We can extract key parameters of our system from the transmission scan by fitting to Eq. 3.71. We find the qubit-waveguide coupling rate $\gamma/2\pi = 3.22$ MHz, the pure dephasing rate $\gamma_\phi/2\pi = 6.23$ kHz, and the temperature of the waveguide $T = 28.5$ mK.

excites the qubit. The qubit will then emit into the waveguide, sending a photon either to the left or right with equal probability. We can define the emitted photon to be in the superposition state $|\psi_{\mathrm{ph}}\rangle = (|01\rangle + |10\rangle)/\sqrt{2}$, where first index denotes the number of photons propagating to the left, and the second index denotes the number of photons propagating to the right in the waveguide. The emission in either direction picks up a $\pi$ phase shift relative to the input tone as seen in Eq. 3.71. In the event that the qubit emits the photon to the right, the photon will destructively interfere with the coherent tone. Alternatively, if the qubit emits the photon to the left, no radiation will be transmitted through the right-end of the waveguide. As a result, the only possible outcome is the reflection of the coherent tone. This appears in the spectrum as the extinction of the transmission at the qubit frequency, as predicted by Eq. 3.71. The rightward-propagating tone effectively reflects off of the qubit, picking up a $\pi$ phase shift and reversing its direction of propagation in the waveguide. Hence, the qubit acts as a mirror to resonant fields in the waveguide. We note that this analysis applies to single photons in the waveguide incident on the qubit as well. In this case, the interference process is simultaneous with the photon absorption and subsequent reimission. The qubit effectively reflects the photon in the direction opposite of its initial propagation direction.

Possible culprits that diminish the interference effect and cause inelastic scattering are qubit saturation by a high-power field, qubit dephasing, thermal excitations in the waveguide, and non-radiative decay. All of this information is encapsulated in Eq. 3.71, but here, we provide an intuitive picture for each source of imperfection:

1. **Qubit saturation with high coherent field power** – if the average photon number of the coherent tone $|\alpha| \approx 1$, that means sometimes two or more photons are incident upon the qubit from the input field. Because of the anharmonicity of the transmon qubit, the qubit can only interact with one photon at the qubit-frequency at a time. The qubit emission will only fully destructively interfere with one photon in the coherent field, the other photons in the input field will pass by unaffected. This means that the transmission will not become fully extinct at the qubit frequency in cases of high field powers with $|\alpha| \geq 1$.

2. **Qubit dephasing** – the interference effect relies on the $\pi$ phase shift of the qubit emission relative to the coherent tone. If the qubit has a non-negligible dephasing rate, the qubit will dephase during the absorption of the input field and the decay back into the waveguide. As a result, the phase of the qubit emission relative to the input field is no longer well-defined, limiting the interference effect.

3. **Thermal excitations in the waveguide** – Because of the presence of thermal photons, the qubit is no longer only interacting with photons sent from the coherent tone. This randomizes the phase of the emission relative to the input field and also limits the interference effect.

4. **Non-radiative decay** – We did not include non-radiative decay, the loss of qubit population to decay channels other than the waveguide, in our model.

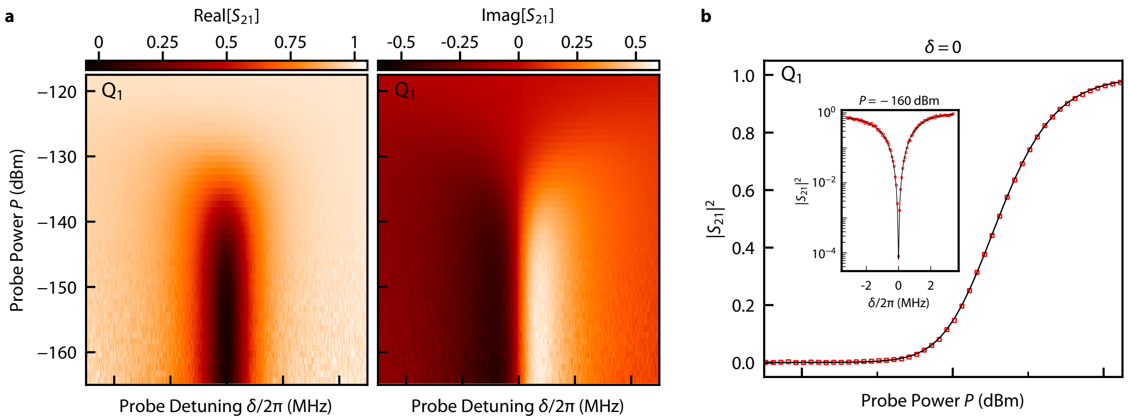

Figure 3-6: **Transmission power scan of qubit-waveguide system.** a) Real (left) and imaginary (right) components of the transmission spectrum of a coherent tone incident on the qubit through the waveguide as a function of the qubit-tone detuning $\delta/2\pi$ and the input power $P$. b) Transmittance $|S_{21}|^2$ as a function of input field power $P$ at zero qubit-tone detuning ($\delta/2\pi = 0$). The measured data is plotted in red, and the theoretical fit is plotted in black. The inset shows the frequency response of the emitter qubit at input field power $P$ = -160 dBm.

> However, we can add it to the model easily by setting the thermally enhanced relaxation rate $\gamma_1^{\text{th}} = (2\bar{\text{n}}_{\text{th}} + 1)(\gamma + \gamma_{\text{nr}})$, where $\gamma_0$. The presence of non-radiative decay means that the excitation of the qubit provided by the input field will not decay back into the waveguide in full. The qubit will absorb the input field and decay into the other channels in the environment, so the emission into the waveguide decreases in amplitude, decreasing the level of extinction in transmission at the qubit frequency.

One more parameter of interest is the absolute field power $P$ incident on the qubit. This is difficult to measure directly because of the attenuators and amplifiers present in the measurement line – we can only measure relative powers. We note that during the fitting process shown in Fig. 3-5b, we omit the Rabi frequency ($\Omega_{\text{p}} = 0$) under the assumption that the field power is very low, and $\Omega_{\text{p}}$ is much slower than other processes in the system. This omission is non-physical, but simplifies the fitting process. Therefore, we do not extract $\Omega_{\text{p}}$ from the transmission scan. Instead, we perform a 2D transmission scan and sweep the input power to perform a 2D fit. We know the step size of power sweep, so we can use the Rabi frequency of the lowest power transmission scan $\Omega_{\mathrm{p0}}$ as a fit parameter to calibrate the power $P$ and confirm the other key fit parameters of Eq. 3.71, as shown in Fig 3-6.

In this chapter, we have discussed several models of a qubit-waveguide system: an abstract quantum model of an atom coupled to a continuum of environmental modes, a classical circuit model, a detailed quantum model through circuit quantization, and a master equation model. Each model helps us gain a different perspective for the same system. We derived the wQED Hamiltonian, and we used input-output theory to relate the qubit dynamics to the dynamics of the fields in the waveguide. We discussed the interaction of a qubit with coherent and single-photon fields in the waveguide. In Chapter 4, we use these tools to discuss the collective, distance-dependent interaction of multiple qubits coupled to a common waveguide.

# Chapter 4

# Multiple Qubits on a Waveguide

Waveguide Quantum Electrodynamics has been explored in the context of atoms coupled to nanofibers [50]. Though the incoming field is sent through the waveguide in one dimension, the atom re-emits the radiation isometrically in three dimensions. This results in poor spatial-mode matching, which is an indication that the atom is not strongly-coupled to the waveguide. This makes it difficult to study interference effects in the waveguide, let alone interactions between atoms coupled to the same waveguide.

Alternatively, the macroscopic nature of superconducting artificial atoms results in natively large electric dipole moments [31], and waveguides confine photonic modes in 1D, increasing the field density. This enables artificial atoms to strongly-couple to the 1D continuum of modes in a waveguide. Thus, artificial atoms coupled to waveguides are ideal for the exploration of waveguide-mediated atom-atom interactions.

In this chapter, we investigate the collective effects that emerge when multiple superconducting qubits are coupled to a common waveguide. First, we discuss interference effects of two qubits coupled to the same continuum of modes with an abstract quantum model. We derive a general master equation for a system of many qubits coupled to the same waveguide. Then, we perform case studies for systems of two qubits coupled to the same waveguide at two key inter-qubit spacings. At the end of this chapter, we highlight wQED experiments in superconducting circuits in recent years.

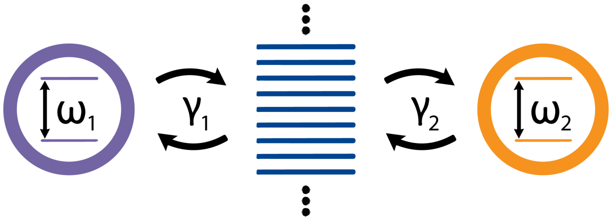

Figure 4-1: **Abstract quantum model of two atoms (qubits) coupled to a common continuum of ambient modes.** Two qubits $Q_1$ and $Q_2$ of frequencies $\omega_1$ and $\omega_2$ coupled to the same continuum, which represents photonic modes in the waveguide, at rates $\gamma_1$ and $\gamma_2$.

Throughout this chapter, we identify the key parameters and interactions of the multiple-qubit waveguide systems, which enable the design of systems to study the effects of choice. We leverage these effects to control qubit-photon interaction in qubit-waveguide systems for applications in long-distance quantum communication.

## 4.1 Interference in Spontaneous Emission

To begin our discussion of multiple-qubit interaction through a continuum of modes in a waveguide, we revisit the abstract quantum model constructed in Sec. 3.1, following the discussion in Ref. [42]. Now we have two qubits, $Q_1$ and $Q_2$, coupled to the same 1D continuum as illustrated in Fig. 4-1. We write the system Hamiltonian

$$\frac{\hat{H}}{\hbar} = \sum_{q=1,2} \omega_q \hat{\sigma}_q^+ \hat{\sigma}_q^- + \sum_k \omega_k \hat{a}_k^\dagger \hat{a}_k + \sum_{q=1,2} \sum_k g_k^* \hat{a}_k^\dagger \hat{\sigma}_q^- + g_k \hat{a}_k \hat{\sigma}_q^+, \tag{4.1}$$

where $\omega_{q=1,2}$ are the qubit frequencies, $\omega_k$ is the mode frequency, and $g_k$ is the single-mode Rabi frequency for each qubit-mode pair. We make the implicit assumption that $g_k$ is the same for each qubit. After rotating frame transformations into the frames of each qubit and all waveguide modes, the interaction Hamiltonian is

$$\frac{\hat{H}_{\text{int}}}{\hbar} = \sum_k \hat{a}_k (g_k e^{-i(\omega_1-\omega_k)t} \hat{\sigma}_1^+ + g_k e^{-i(\omega_2-\omega_k)t} \hat{\sigma}_2^+) + h.c. \tag{4.2}$$

The most general wavefunction of the system in the single-excitation manifold is

$$|\psi(t)\rangle = c_1(t)|1,0,0_k\rangle + c_2(t)|0,1,0_k\rangle + \sum_k c_k(t)|0,0,k\rangle, \tag{4.3}$$

where the first index of the kets denotes the state of $Q_1$, the second index denotes the state of $Q_2$, and the third index denotes the number of excitations in mode $k$. The implementation of the Wigner-Weisskopf theory of spontaneous emission detailed in Sec. 3.1 on this system yields the following equations of motions for the probability amplitudes

$$\begin{aligned} \dot{c}_1(t) &= \left[i(\omega_1 - \omega_2) - \frac{\gamma}{2}\right] c_1(t) - \frac{\gamma}{2} c_2(t) \\ \dot{c}_2(t) &= -\frac{\gamma}{2}(c_2(t) + c_1(t)) \end{aligned} \tag{4.4}$$

where $\gamma = \gamma_1 = \gamma_2$ and $\gamma_2$ is the coupling rate of each qubit to the waveguide. Assuming that at time $t = 0$, $Q_1$ is excited and $Q_2$ is in the ground state. The initial probability amplitudes are $c_1(0) = 1$, $c_2(0) = 0$, and $c_k(0) = 0$. In the case that the qubits are resonant ($|\omega_1 - \omega_2| = 0$), the time-dependent population of each qubit is

$$\begin{aligned} |c_1(t)|^2 &= e^{-\gamma t} \cosh^2\left(\frac{\gamma t}{2}\right) = \frac{1}{4}(e^{-2\gamma t} + 2e^{-\gamma t} + 1) \\ |c_2(t)|^2 &= e^{-\gamma t} \sinh^2\left(\frac{\gamma t}{2}\right) = \frac{1}{4}(-e^{-2\gamma t} + 2e^{-\gamma t} + 1). \end{aligned} \tag{4.5}$$

From these equations, as plotted in Fig. 4-2a, we see several key differences from bare qubit decay due to the presence of $Q_2$ on the same waveguide:

1. $Q_2$ absorbs some of the emission from $Q_1$.

2. $Q_1$ does not fully emit the excitation. In steady state ($t \to \infty$), $Q_1$ and $Q_2$ both have a population of 0.25.

3. The decay from $Q_1$ is enhanced by the presence of $Q_2$ on the same waveguide – that is, $Q_1$ decays more quickly to its steady state value than in the case of individual qubit decay into the waveguide. This effect is called correlated decay.

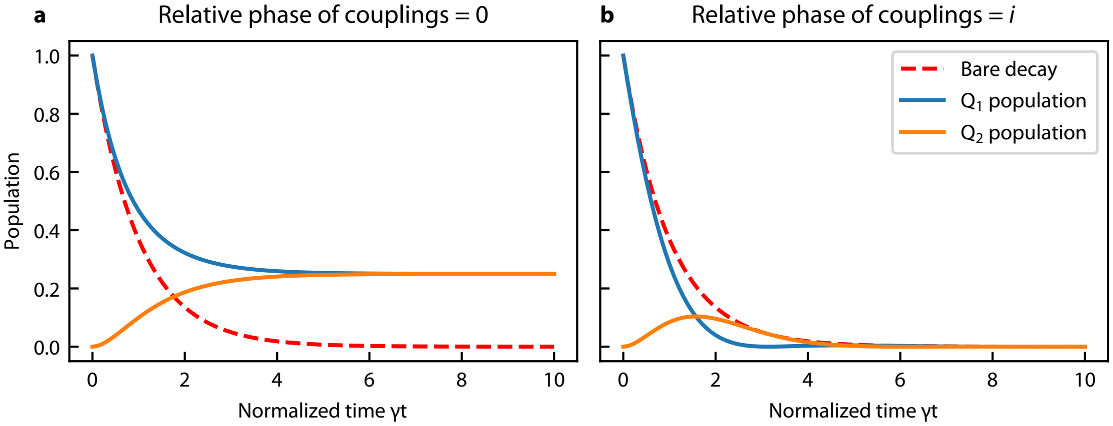

Figure 4-2: **Time dynamics of two qubits coupled to a common continuum of modes.** $Q_1$ is initialized into the excited state. a) Correlated decay of $Q_1$ and $Q_2$ in the waveguide. The qubits have identical single-mode coupling rates. b) Waveguide-mediated coherent exchange of $Q_1$ and $Q_2$. The single-mode coupling rates of the two qubits have a relative phase of $\pi/2$.

Note, we obtained this result by assuming that each qubit is coupled to the waveguide at rate $\gamma$. This was implicit in the interaction Hamiltonian given in Eq. 4.2. Next, we will impose a relative phase of $\pi/2$ between the single-mode Rabi frequencies of each qubit. Though this seems contrived in our abstract model, this phase is a key parameter we can design into our wQED systems by changing the distance between the two qubits. This can be interpreted as the two qubits coupling to the same mode, but because they are spatially separated, they experience the mode at a different phase. The modified interaction Hamiltonian is

$$\frac{\hat{H}_{\text{int}}}{\hbar} = \sum_k \hat{a}_k (g_k e^{-i(\omega_1-\omega_k)t}\hat{\sigma}_1^+ - i g_k e^{-i(\omega_2-\omega_k)t}\hat{\sigma}_2^+) + h.c. \tag{4.6}$$

A similar analysis will yield the population of each qubit as a function of time

$$\begin{aligned} |c_1(t)|^2 &= e^{-\gamma t}\cos^2\left(\frac{\gamma t}{2}\right) \\ |c_2(t)|^2 &= e^{-\gamma t}\sin^2\left(\frac{\gamma t}{2}\right). \end{aligned} \tag{4.7}$$

The time dynamics now resemble decaying Rabi oscillations. In this case, the qubits are exchanging population during the decay process, as shown in Fig. 4-2b. These are the dynamics of a lossy Jaynes-Cummings interaction, or lossy Rabi oscillations [42]. The qubits experience an effective coherent exchange interaction mediated by the waveguide while they decay into the continuum modes. We note that the steady-state population is zero for both qubits, as the emission fully propagates away from the qubits through the waveguide modes.

Through this abstract model of two qubits coupled to a continuum of modes, we have peaked into the two main types of collective, distance-dependent interactions qubits experience when coupled to a common waveguide: correlated decay and coherent exchange. We dive deeper into the details with a master equation approach in the following sections.

## 4.2 Master Equation Derivation

The discussion of the time-dynamics of the system of two qubits coupled to the same continuum helps us gain insight. However, we seek a more general model to capture the collective effects that emerge when multiple qubits share a common waveguide, following the approaches of Refs. [45, 47]. We revisit the Hamiltonian derived in Eq. 3.51, which we extend for two qubits coupled to a common waveguide,

$$\begin{aligned}
\hat{H} &= \hat{H}_{\mathrm{q}} + \hat{H}_{\mathrm{wg}} + \hat{H}_{\mathrm{int}} \\
\hat{H}_{\mathrm{q}} &= \sum_{j=1,2} \hbar\omega_j \hat{\sigma}_j^+ \hat{\sigma}_j^- \\
\hat{H}_{\mathrm{wg}} &= \int_0^\infty dk[\hbar\nu k(\hat{a}_{\mathrm{L}}^\dagger(k)\hat{a}_{\mathrm{L}}(k) + \hat{a}_{\mathrm{R}}^\dagger(k)\hat{a}_{\mathrm{R}}(k))] \\
\hat{H}_{\mathrm{int}} &= \sum_{j=1,2} \int_0^\infty dk[\hbar g(k)(\hat{\sigma}_j^+ \hat{a}_{\mathrm{R}}(k) e^{ikx_j} + \hat{\sigma}_j^- \hat{a}_{\mathrm{L}}^\dagger(k) e^{-ikx_j} + h.c.)].
\end{aligned} \tag{4.8}$$

where $\hat{H}_{\mathrm{q}}$ is the free-qubit Hamiltonian, $\hat{H}_{\mathrm{wg}}$ is the Hamiltonian of the photonic modes in the waveguide, and $\hat{H}_{\mathrm{int}}$ is the interaction Hamiltonian. In the interaction Hamiltonian, the integral over mode $k$ is negligible except near the qubit frequencies, because each qubit only interacts with the photonic modes near the qubit frequency.

Therefore, we can extend the lower bound of the integrals over mode $k$ to $-\infty$. Defining the Fourier pairs,

$$\begin{aligned}\hat{a}_{j,\mathrm{R}} = \hat{a}_{\mathrm{R}}(x_j,t) &= \int_{-\infty}^{\infty} \frac{dk}{\sqrt{2\pi}} \hat{a}_{\mathrm{R}}(k) e^{ikx_j} \\ \hat{a}_{j,\mathrm{L}} = \hat{a}_{\mathrm{L}}(x_j,t) &= \int_{-\infty}^{\infty} \frac{dk}{\sqrt{2\pi}} \hat{a}_{\mathrm{L}}(k) e^{-ikx_j},\end{aligned} \tag{4.9}$$

we rewrite the interaction Hamiltonian as

$$\frac{\hat{H}_{\mathrm{int}}}{\hbar} = \sum_j \sqrt{\frac{\gamma_j}{2}} (\hat{\sigma}_j^+ \hat{a}_{j,\mathrm{R}} + \hat{\sigma}_j^- \hat{a}_{j,\mathrm{L}}^\dagger + \hat{\sigma}_j^- \hat{a}_{j,\mathrm{R}}^\dagger + \hat{\sigma}_j^+ \hat{a}_{j,\mathrm{L}}). \tag{4.10}$$

where $\gamma_j$ is the coupling rate of each qubit to the waveguide, defined in Eq. 3.52. We define an operator $\hat{O}$ that acts only on the subspace of the qubits. Using the Heisenberg equation of motion, we find

$$\frac{d\hat{O}}{dt} = \frac{i}{\hbar}[\hat{H}_q, \hat{O}] + i \sum_{j=1,2} \sqrt{\frac{\gamma_j}{2}} \left[ (\hat{a}_{j,\mathrm{R}}^\dagger + \hat{a}_{j,\mathrm{L}}^\dagger)[\hat{\sigma}_j^-, \hat{O}] + [\hat{\sigma}_j^+, \hat{O}](\hat{a}_{j,\mathrm{R}} + \hat{a}_{j,\mathrm{L}}) \right] \tag{4.11}$$

To obtain the relationship between the two-qubit dynamics and the field dynamics in the waveguide, we use the input-output relations, referencing the location of the first qubit $x_1$ in Eq. 3.61 for zero input field,

$$\begin{aligned}\hat{a}_{1,\mathrm{R}} &= -i\sqrt{\frac{\gamma_1}{2}} \hat{\sigma}_1^- - i\sqrt{\frac{\gamma_2}{2}} \hat{\sigma}_2^- e^{-i\frac{\omega_2 d}{\nu}} \\ \hat{a}_{1,\mathrm{L}} &= -i\sqrt{\frac{\gamma_1}{2}} \hat{\sigma}_1^- - i\sqrt{\frac{\gamma_2}{2}} \hat{\sigma}_2^- e^{i\frac{\omega_2 d}{\nu}}.\end{aligned} \tag{4.12}$$

where we specify the distance between the two qubits along the waveguide as $d = x_2 - x_1$. We note that we have implicitly adopted the assumptions of Markovianity and the long-time limit presented in Sec. 3.4. We assume that $\mathrm{Q}_2$ is further to the right along the waveguide than $\mathrm{Q}_2$ ($x_2 > x_1$), and the corresponding input-output relations at the location of the second qubit $x_2$ are

$$\begin{aligned}\hat{a}_{2,\mathrm{R}} &= -i\sqrt{\frac{\gamma_2}{2}}\hat{\sigma}_2^- - i\sqrt{\frac{\gamma_1}{2}}\hat{\sigma}_1^- e^{i\frac{\omega_1 d}{\nu}} \\ \hat{a}_{2,\mathrm{L}} &= -i\sqrt{\frac{\gamma_2}{2}}\hat{\sigma}_2^- - i\sqrt{\frac{\gamma_1}{2}}\hat{\sigma}_1^- e^{-i\frac{\omega_1 d}{\nu}}.\end{aligned} \tag{4.13}$$

We substitute these operators into Eq. 4.11 and arrive at an evolution equation for $\hat{O}$ in terms of operators that only act on the qubit subspace

$$\begin{aligned}\frac{d\hat{O}}{dt} &= \frac{i}{\hbar}[\hat{H}_q, \hat{O}] + \sum_{j=1,2}\frac{\gamma_j}{2}\left[[\hat{\sigma}_j^+, \hat{O}]\hat{\sigma}_j^- + \hat{\sigma}_j^+[\hat{\sigma}_j^-, \hat{O}]\right] \\ &+ \sum_{j=1,2,m=\bar{j}}\frac{\sqrt{\gamma_1\gamma_2}}{2}\left[[\hat{\sigma}_j^+, \hat{O}]\hat{\sigma}_m^- e^{i\frac{\omega_m d}{\nu}} + \hat{\sigma}_m^+ e^{-i\frac{\omega_m d}{\nu}}[\hat{\sigma}_j^-, \hat{O}]\right]\end{aligned} \tag{4.14}$$

where $m = \bar{j}$ is the index opposite $j$. Next, we denote the total density matrix of the entire system as $\hat{\rho}_\Sigma$. We can obtain the density matrix of the two-qubit system through a partial trace over the photonic modes in the waveguide, i.e. $\hat{\rho} = \mathrm{Tr}_{\mathrm{wg}}[\hat{\rho}_\Sigma]$, where $\hat{\rho}$ is the density matrix of the two-qubit system. Because we know that $\hat{O}$ acts on the subspace of the qubit states only, we use the cyclic invariance of the trace operation to show

$$\frac{d\langle\hat{O}\rangle}{dt} = \mathrm{Tr}\left[\frac{d\hat{O}}{dt}\hat{\rho}_\Sigma\right] = \mathrm{Tr}_q\left[\hat{O}\frac{d\hat{\rho}}{dt}\right]. \tag{4.15}$$

Combining this relation with Eq. 4.14, we arrive at the reduced master equation for the two-qubit system

$$\frac{d\hat{\rho}}{dt} = \frac{i}{\hbar}[\hat{H}_q + \hat{H}_J, \hat{\rho}] + \sum_{j,k=1,2}\gamma_{jk}D[\hat{\sigma}_j^-, \hat{\sigma}_k^-]\hat{\rho}, \tag{4.16}$$

where

$$\hat{H}_J = \hbar(J\hat{\sigma}_1^+\hat{\sigma}_2^- + J^*\hat{\sigma}_2^+\hat{\sigma}_1^-) \tag{4.17}$$

is the waveguide-mediated coherent exchange interaction Hamiltonian between the two qubits of strength

$$J = \frac{\sqrt{\gamma_1\gamma_2}}{2}\left(\frac{e^{i\frac{\omega_2 d}{\nu}} - e^{-i\frac{\omega_1 d}{\nu}}}{2i}\right). \tag{4.18}$$

We specify the individual decay rates of each qubit as $\gamma_{jj} = \gamma_j$, and the correlated decay rate

$$\gamma_{21} = \gamma_{12}^* = \sqrt{\gamma_1\gamma_2}\left(\frac{e^{i\frac{\omega_2 d}{\nu}} + e^{-i\frac{\omega_1 d}{\nu}}}{2}\right). \tag{4.19}$$

Finally, we define the Lindblad superoperator, which is a linear operator that acts on a vector space of operators, $D[\hat{A},\hat{B}]\hat{\rho} = \hat{B}\hat{\rho}\hat{A}^\dagger - \frac{1}{2}\{\hat{B}^\dagger\hat{A},\hat{\rho}\}$. The Lindblad superopertor accounts for the collapse operators/loss mechanisms built into the master equation formalism.

From this analysis, in addition to individual decay from each qubit into the waveguide, we see two key distance-dependent collective effects emerge when two qubits are coupled to a common waveguide: coherent-exchange mediated by the modes in the waveguide and correlated decay between the qubits. This equation governs the time-dynamics of the two-qubit system in the presence of the waveguide modes. In practice, we use this matrix differential equation to construct analytical models of the populations and coherences of each qubit, as demonstrated in Sec. 3.5.

This master equation can be extended to include an indefinite number of qubits

$$\frac{d\hat{\rho}}{dt} = \frac{i}{\hbar}[\hat{H}_q + \hat{H}_J + \hat{H}_d, \hat{\rho}] + \sum_{j,k}\gamma_{jk}D[\hat{\sigma}_j^-, \hat{\sigma}_k^-]\hat{\rho}, \tag{4.20}$$

with the waveguide-mediated coherent exchange Hamiltonian,

$$\hat{H}_J = \sum_{j,k}\hbar(J_{j,k}\hat{\sigma}_j^+\hat{\sigma}_k^- + J_{j,k}^*\hat{\sigma}_k^+\hat{\sigma}_j^-). \tag{4.21}$$

We add a coherent drive through the waveguide by including a general drive term in the system Hamiltonian

$$\hat{H}_d = \sum_j \hbar d_j(t)(\hat{\sigma}_j^+ + \hat{\sigma}_j^-) \tag{4.22}$$

where the drive amplitude is

$$d_j(t) = \sqrt{\frac{2\gamma_j}{\hbar\omega_j}} \left[\sqrt{P_{\mathrm{L}}} \sin\left(\omega_d\left(t + \frac{x_j}{\nu} + \theta_{\mathrm{L}}\right)\right) + \sqrt{P_{\mathrm{R}}} \sin\left(\omega_d\left(t - \frac{x_j}{\nu} + \theta_{\mathrm{R}}\right)\right)\right], \tag{4.23}$$

which accommodates coherent drives traveling towards the left and right of frequency $\omega_d$, phase $\theta_{\mathrm{L/R}}$, and power $P_{\mathrm{L/R}}$. We assume the input field takes the form of a scaled coherent field $|\alpha\rangle$, where $|\alpha|^2$ is the average photon number [49],

$$\hat{a}_{\mathrm{L/R}}(\omega, 0)|\alpha\rangle = \sqrt{\frac{P_{\mathrm{L/R}}}{\hbar\omega_d}} e^{-i\omega_d\theta_{\mathrm{L/R}}} \delta(\omega - \omega_d)|\alpha\rangle \tag{4.24}$$

We take the Fourier transform using the definition in Eq. 3.57 to find a general time-dependent amplitude of the input field

$$\hat{a}^{\mathrm{in}}_{\mathrm{L/R}}(t)|\alpha\rangle = \sqrt{\frac{P_{\mathrm{L/R}}}{\hbar\omega_d}} e^{-i\omega_d(t+\theta_{\mathrm{L/R}})}|\alpha\rangle. \tag{4.25}$$

In practice, we assume that our drive is resonant with the qubit frequencies $\omega_d \approx \omega_q$ such that the probe power and Rabi frequency are approximately constant over the qubit linewidths $\gamma$. The derivation of the master equation in this section can be distilled to the single driven qubit case shown in Sec. 3.5.

In the following sections, we use this master equation formalism to study resonant two-qubit systems coupled to a common waveguide at integer multiples of two key inter-qubit distances: $d = \lambda/2$ and $d = \lambda/4$, where $\lambda = 2\pi\nu/\omega$ is the wavelength of the qubit emission in the waveguide. Each inter-qubit distance highlights a collective effect that emerges in the two-qubit waveguide system – correlated dissipation and waveguide-mediated exchange respectively.

## 4.3 Superradiance and Subradiance

We consider a system of two resonant, identical qubits $\mathrm{Q}_1$ and $\mathrm{Q}_2$ of frequency $\omega$ and decay rate $\gamma$ coupled to a common waveguide at a separation of $d = \lambda/2$, where

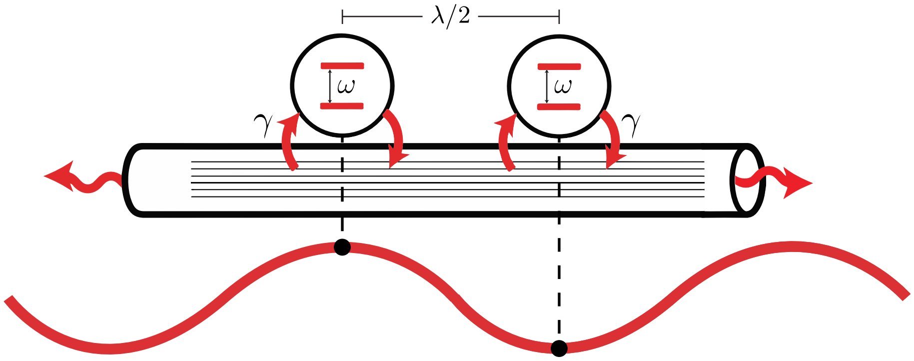

Figure 4-3: **Illustration of two resonant qubits of frequency $\omega$ coupled to a waveguide with inter-qubit distance $d = \lambda/2$.** Below the qubit-waveguide system we draw a field of wavelength $\lambda$ to elucidate the inter-qubit distance. The qubits always couple to the resonant field at points of equal and opposite amplitudes.

$\lambda = 2\pi\nu/\omega$ is the wavelength of the qubit emission. This system is illustrated in Fig. 4-3. The position of $Q_2$ is to the right of the position of $Q_1$ ($x_2 > x_1$). We assume the non-radiative decay is negligible ($\gamma_{\text{nr}} = 0$). The waveguide-mediated coherent exchange interaction between the two-qubits from Eq. 4.18 is

$$J = \frac{\gamma}{2}\sin\left(\frac{\omega d}{\nu}\right) = 0, \tag{4.26}$$

and the correlated decay rate from Eq. 4.19 is

$$\gamma_{21} = \gamma\cos\left(\frac{\omega d}{\nu}\right) = -\gamma. \tag{4.27}$$

We see that for an inter-qubit distance of $d = \lambda/2$, there is no waveguide-mediated exchange interaction and the correlated decay strength is maximized. The master equation for the dynamics of this two-qubit system in the frame of the rightward-propagating drive frequency $\omega_d$ is

$$\frac{d\hat{\rho}}{dt} = \frac{i}{\hbar}[\hat{H}_q + \hat{H}_d, \hat{\rho}] + \gamma\left(D[\hat{\sigma}_1^-] + D[\hat{\sigma}_2^-]\right)\hat{\rho} - \gamma\left(D[\hat{\sigma}_1^-, \hat{\sigma}_2^-] + D[\hat{\sigma}_2^-, \hat{\sigma}_1^-]\right)\hat{\rho}, \tag{4.28}$$

where the free-qubit Hamiltonian is

$$\hat{H}_q = \hat{\hbar}(\omega - \omega_d)(\hat{\sigma}_1^+\hat{\sigma}_1^- + \hat{\sigma}_2^+\hat{\sigma}_2^-), \tag{4.29}$$

the drive Hamiltonian is

$$\hat{H}_d = \sum_{j=1,2} \hbar(\Omega\hat{\sigma}_j^+ + \Omega^*\hat{\sigma}_j^-), \tag{4.30}$$

with drive strength/Rabi frequency

$$\Omega = -i\sqrt{\frac{\gamma}{2}}\langle \hat{a}_{\mathrm{R}}^{\mathrm{in}}\rangle e^{-i\frac{\omega_d x_j}{\nu}}, \tag{4.31}$$

and $D[\hat{A},\hat{B}]\hat{\rho} = \hat{B}\hat{\rho}\hat{A}^\dagger - \frac{1}{2}\{\hat{B}^\dagger\hat{A},\hat{\rho}\}$ is the Lindblad superoperator. To elucidate the dynamics of the system with correlated decay, we move from the standard basis of qubit states to the dressed basis composed of a dark ($D$) and bright ($B$) state. We rewrite the master equation of Eq. 4.28 following [45],

$$\frac{d\hat{\rho}}{dt} = \frac{i}{\hbar}[\hat{H}_q + \hat{H}_d, \hat{\rho}] + \sum_{i=B,D} \Gamma_i D[\hat{\sigma}_i^-]\hat{\rho}, \tag{4.32}$$

where we define the correlated decay rates $\Gamma_B = 2\gamma$ and $\Gamma_D = 0$. The dressed lowering operators are

$$\begin{aligned} \hat{\sigma}_B^- &= \frac{1}{\sqrt{2}}(\hat{\sigma}_1^- - \hat{\sigma}_2^-) \\ \hat{\sigma}_D^- &= -\frac{1}{\sqrt{2}}(\hat{\sigma}_1^- + \hat{\sigma}_2^-). \end{aligned} \tag{4.33}$$

The bright and dark states $|B/D\rangle$ are defined by $\hat{\sigma}_{B/D}^-|B/D\rangle = 0$. In the standard qubit basis $|q_1 q_2\rangle$, where the first index denotes the state of $\mathrm{Q}_1$ and the second index denotes the state of $\mathrm{Q}_2$, the bright and dark states are

$$\begin{aligned} |B\rangle &= \frac{1}{\sqrt{2}}(|ge\rangle - |eg\rangle) \\ |D\rangle &= \frac{1}{\sqrt{2}}(|ge\rangle + |eg\rangle). \end{aligned} \tag{4.34}$$

The presence of the bright state $|B\rangle$ is a phenomenon known as superradiance, as population in this state decays at double the individual qubit decay rate. Alternatively, the presence of the dark state $|D\rangle$ is a phenomenon known as subradiance, as there is zero radiative decay from this state into the waveguide.

We revisit the time dynamics of our abstract model in Sec. 4.1. The qubit populations over time for the analogous system are presented in Fig. 4-1a. The initial condition of this system in the standard qubit basis was $|q_1q_2\rangle = |eg\rangle$. In the dressed basis, the initial state of the system is $|\psi(t=0)\rangle = (|D\rangle - |B\rangle)/\sqrt{2}$. This means that the system is in a superposition of dressed states at $t = 0$. We can clearly see the dynamics of superradiance and subradiance superimposed in Fig. 4-1a. At early times, we see the bright state decay at a rate faster than the individual qubit decay. As $t \to \infty$, we see that the system is in a mixed state composed of the dark state and the joint ground state, which explains why the steady-state population in the excited states of both qubits is non-zero, while the steady state system coherences are zero ($c_1(t \to \infty)^* c_2(t \to \infty) = 0$) following from Eq. 4.5.

We note that the example in Fig. 4-1a is analogous to a pair of qubits that are spaced $d = \lambda$ along the waveguide. In this section, the inter-qubit distance is $d = \lambda/2$. The population dynamics are identical for all $d = n\lambda/2$, where $n$ is any integer, however, the coherences of the dark and bright states will alternate signs for even and odd $n$.

Next, we study the system's response to a resonant drive. We rewrite the drive Hamiltonian in the dressed basis

$$\hat{H}_d = \hbar(\Omega_B \hat{\sigma}_B^+ + \Omega_B^* \hat{\sigma}_B^-), \tag{4.35}$$

where the bright state is driven with strength

$$\Omega_B = -i\sqrt{\gamma}\langle \hat{a}_{\mathrm{R}}^{\mathrm{in}} \rangle e^{-i\frac{\omega_d x_j}{\nu}}. \tag{4.36}$$

We see that the state $|D\rangle$ is "dark" to the drive Hamiltonian $\hat{H}_d$, i.e. $\hat{H}_d|D\rangle = 0$. This means that we cannot drive the dark state through the waveguide. We also see that $\Omega_B = \sqrt{2}\Omega$, which means the bright state couples more strongly to the modes in the waveguide than in the single-qubit case. The effective drive power incident on the bright state doubles.

To study the limitations of superradiance and subradiance, we consider the energy level diagram shown in Fig 4-4a. The dark state cannot be populated through the waveguide, as the corresponding matrix element between the joint ground state and the dark state is zero. The joint excited state $|ee\rangle$ can be reached from the bright state $|B\rangle$ with a strong drive through the waveguide, opening up pathways for populating the dark state $|D\rangle$. We will see imperfect subradiance and superradiance due to:

1. **Non-negligible non-radiative decay** – the $|ee\rangle$ state is populated with a strong drive through the waveguide. Spontaneous emission of either qubit from the excited state to the ground state into external environmental modes populates the dark state. Non-radiative decay can be added as an ingredient to this model by modifying the the correlated decay rates $\Gamma_D = \gamma_{\text{nr}}$ and $\Gamma_B = 2\gamma - \gamma_{\text{nr}}$.

2. **Mismatched decay rates** – if the decay rates of the qubits are not symmetric ($\gamma_1 \neq \gamma_2$), the coupling between the $|ee\rangle$ and $|D\rangle$ states is non-zero. The matrix element $\langle D|\hat{\sigma}_B^-|ee\rangle$ is proportional to $(\gamma_1 - \gamma_2)/(\gamma_1 + \gamma_2)$. Once there is population in the $|ee\rangle$ state, strongly driving the bright state through the waveguide will also populate the dark state. The effect of this asymmetry can be counteracted by tuning the qubit frequencies to match decay rates more precisely, however, this will modify the effective inter-qubit distance $d = \lambda/2$ and break previous assumptions.

3. **Qubit dephasing** – the dark state can be populated via qubit dephasing caused by ambient flux noise. This can be visualized with the two-qubit Bloch sphere, where the $\pm z$ axes are single-qubit excited states and the $\pm x$ are the dark and bright states as illustrated in Fig. 4-4b. If the system is prepared into the bright state, the state vector lies on the equator of the Bloch sphere. Fluctuations of the qubit frequencies due to environmental variables cause this Bloch vector to gradually rotate towards the dark state during system evolution.

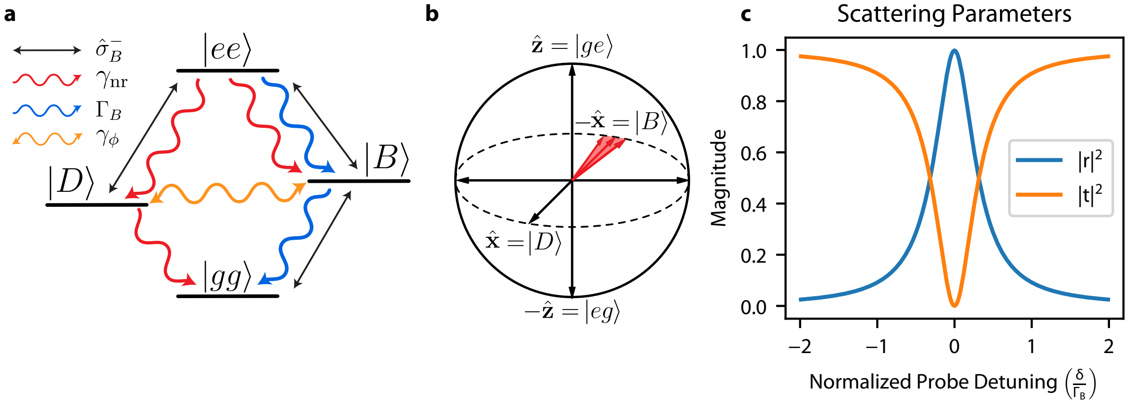

Figure 4-4: **Steady-state dynamics and scattering parameters of a two-qubit system spaced $d = \lambda/2$ along a common waveguide. a)** 4-level energy diagram of resonant two-qubit system coupled to a common waveguide. For an inter-qubit distance along the waveguide of $d = \lambda/2$, the qubits experience superradiance and subradiance, resulting in the presence of a bright $|B\rangle$ and dark state $|D\rangle$. The qubits can only be driven from the joint ground state to the bright state, as denoted by the black arrow labeled $\hat{\sigma}_B^-$. Drives with strong powers can populate the joint excited state $|ee\rangle$, which will decay into the bright state at rate $\Gamma_B$, denoted with a blue curvy arrow. In the presence of non-radiative decay of strength $\gamma_{\text{nr}}$, pictured as a red curvy arrow, the joint excited state decays into both the dark and bright states. For mismatched decay rates ($\gamma_1 \neq \gamma_2$), the dark state couples to the joint excited state, also denoted by $\hat{\sigma}_b^-$. The dark state can also be populated directly from the bright state through dephasing, as pictured with an orange curvy arrow. **b)** Two-qubit Bloch sphere representation of the system in the single-excitation subspace. If the system is prepared in $|B\rangle$, dephasing due to environmental fluctuations illustrated by the blurred red arrow populates the dark state during system evolution. **c)** Simulated scattering parameters, transmission and reflection, for the two-qubit system. The transmission matches the spectrum of a single qubit coupled to a waveguide with a linewidth $\Gamma_B$, which is twice the decay rate $\gamma$ of each individual qubit.

Our next goal is to evaluate the scattering parameters of a coherent probe incident on the two-qubit system. We see that from the perspective of the waveguide, the two-qubit system is effectively a single two-level system coupled to the waveguide at rate $\Gamma_B$. In other words, the waveguide only "sees" the bright state. Therefore, we can write the input-output relations to relate the qubit emission to the fields in the waveguide in the absence of non-radiative decay and dephasing using Eq. 3.62,

$$\hat{a}_{\text{L/R}}^{\text{out}} = \hat{a}_{\text{L/R}}^{\text{in}} \mp i\sqrt{\gamma}\hat{\sigma}_B^-. \tag{4.37}$$

We are interested in the steady-state dynamics of the system, so we set $\dot{\hat{\rho}} = 0$. We use the steady-state density matrix to evaluate the coherence $\langle \hat{\sigma}_B^- \rangle = \mathrm{Tr}[\hat{\rho}\sigma_B^-]$. We assume the probe is propagating to the right and $\langle \hat{a}_{\mathrm{L}}^{\mathrm{in}} \rangle = 0$. To first order of the input amplitude $\langle \hat{a}_{\mathrm{R}}^{\mathrm{in}} \rangle$, we evaluate the transmission and reflection coefficients

$$\begin{aligned} t &= \frac{\langle \hat{a}_{\mathrm{R}}^{\mathrm{out}} \rangle}{\langle \hat{a}_{\mathrm{R}}^{\mathrm{in}} \rangle} = 1 + \frac{i\Gamma_B}{2\delta - i\Gamma_B} \\ r &= \frac{\langle \hat{a}_{\mathrm{L}}^{\mathrm{out}} \rangle}{\langle \hat{a}_{\mathrm{R}}^{\mathrm{in}} \rangle} = \frac{-i\Gamma_B}{2\delta - i\Gamma_B}, \end{aligned} \tag{4.38}$$

where $\delta = \omega - \omega_d$ is the qubit-drive detuning. Notably, these scattering parameters correspond to those of a single qubit-waveguide system, as first demonstrated in [32]. Because the probe is low power and the model is ideal, we see full extinction in the transmission for a resonant probe. To include imperfections in the model such as high probe power, non-radiative decay, thermal photons, and qubit dephasing, we can apply the same analysis demonstrated in Sec. 3.5 for a single qubit coupled to a waveguide.

## 4.4 Waveguide-Mediated Exchange Interaction

Next, we study a system of two identical resonant qubits $\mathrm{Q}_1$ and $\mathrm{Q}_2$ of frequency $\omega$. The qubits are strongly coupled to a common waveguide ($\gamma_{\mathrm{nr}} = 0$) with an inter-qubit distance $d = \lambda/4$, as shown in Fig. 4-5. For this inter-qubit distance, the waveguide-mediated coherent exchange interaction is maximized, as follows from the derivation in Sec. 4.2 (Eq. 4.18)

$$J = \frac{\gamma}{2} \sin\left(\frac{\omega d}{\nu}\right) = \frac{\gamma}{2}, \tag{4.39}$$

The two qubits do not experience correlated decay as given by Eq. 4.19

$$\gamma_{21} = \gamma \cos\left(\frac{\omega d}{\nu}\right) = 0. \tag{4.40}$$

We see that the qubits exchange population at rate $J = \gamma/2$ while they each individually decay into the waveguide at rate $\gamma$. This situation is analogous to the example

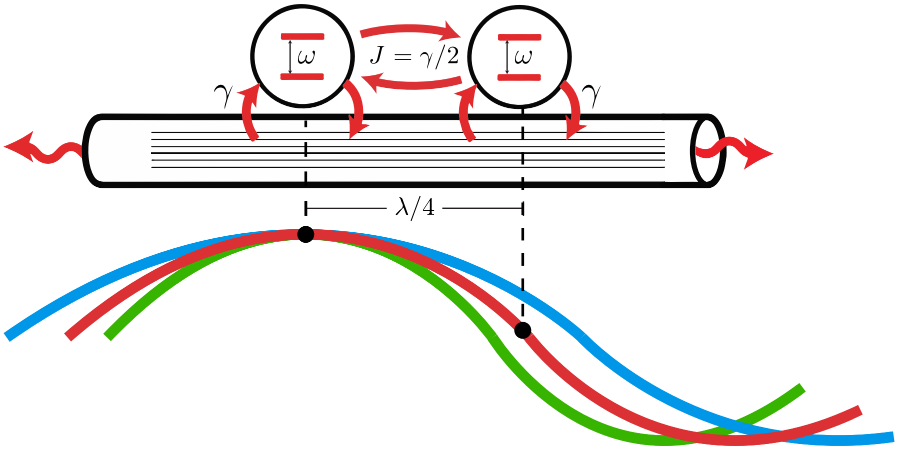

Figure 4-5: **Illustration of two resonant qubits of frequency $\omega$ coupled to a waveguide at distance $d = \lambda/4$.** Below the qubit-waveguide system we draw a resonant field of wavelength $\lambda$ in red to compare and highlight the inter-qubit distance of $d = \lambda/4$. The qubits experience a waveguide-mediated coherent exchange interaction of strength $J = \gamma/2$, due to virtual interaction mediated by the detuned modes colored in blue and green.

discussed in Fig. 4-2b – the lossy Jaynes-Cummings interaction. Recall that we achieved this result in the abstract quantum model of Sec. 4.1 by assuming a relative phase of $\pi/2$ between the single-mode couplings $g_k$ of each qubit. We implement this relative phase physically by choosing an inter-qubit distance of $d = \lambda/4$. The master equation that describes the qubit time dynamics in the frame of a rightward drive at frequency $\omega_d$ is

$$\frac{d\hat{\rho}}{dt} = \frac{i}{\hbar}[\hat{H}_q + \hat{H}_J + \hat{H}_d, \hat{\rho}] + \gamma\left(D[\hat{\sigma}_1^-] + D[\hat{\sigma}_2^-]\right)\hat{\rho}. \tag{4.41}$$

We write the waveguide-mediated exchange Hamiltonian,

$$\hat{H}_J = \frac{\hbar\gamma}{2}(\hat{\sigma}_1^+\hat{\sigma}_2^- + \hat{\sigma}_2^+\hat{\sigma}_1^-), \tag{4.42}$$

the free-qubit Hamiltonian,

$$\hat{H}_q = \hat{\hbar}(\omega - \omega_d)(\hat{\sigma}_1^+\hat{\sigma}_1^- + \hat{\sigma}_2^+\hat{\sigma}_2^-), \tag{4.43}$$

and the drive Hamiltonian,

$$\hat{H}_d = \sum_{j=1,2} \hbar(\Omega\hat{\sigma}_j^+ + \Omega^*\hat{\sigma}_j^-), \tag{4.44}$$

with drive strength/Rabi frequency is

$$\Omega = -i\sqrt{\frac{\gamma}{2}}\langle\hat{a}_{\mathrm{R}}^{\mathrm{in}}\rangle e^{-i\frac{\omega_d x_j}{\nu}}. \tag{4.45}$$

The Lindblad dissipator is defined as $D[\hat{A}]\hat{\rho} = \hat{A}\hat{\rho}\hat{A}^\dagger - \frac{1}{2}\{\hat{A}^\dagger A, \hat{\rho}\}$.

We provide an intuitive explanation for the waveguide-mediated exchange interaction by extending the interaction term of the wQED Hamiltonian in Eq. 3.51 for two qubits,

$$\hat{H}_{\mathrm{int}} = \int_0^\infty d\omega_k \hbar g(\omega_k)(\hat{\sigma}_1^+\hat{a}_{\mathrm{R}}(\omega_k) + \hat{\sigma}_1^-\hat{a}_{\mathrm{L}}^\dagger(\omega_k) + i\hat{\sigma}_2^+\hat{a}_{\mathrm{R}}(\omega_k) - i\hat{\sigma}_2^-\hat{a}_{\mathrm{L}}^\dagger(\omega_k) + h.c.). \tag{4.46}$$

We know from Sec. 3.3, in the single-qubit case, this interaction Hamiltonian gives rise to the decay of a *real* photon into the resonant modes and the detuned modes only contribute in the form of a Lamb shift. However, in the two-qubit case, the detuned modes can mediate virtual/Raman interactions between the two qubits of strength $J(\omega_k) = g_1(\omega_k)g_2(\omega_k)/(\omega_k - \omega)$ [42]. In other words, $\mathrm{Q}_1$ can emit a *virtual* photon at a detuned frequency that $\mathrm{Q}_2$ can absorb. The rough effective virtual interaction Hamiltonian between the two qubits through all of the detuned modes ($\omega \neq \omega_k$) in the waveguide is

$$\hat{H}_J = \int_{-\infty}^\infty d\omega_k \frac{i\hbar g^2(\omega_k)}{\omega_k - \omega}(\hat{\sigma}_1^-\hat{\sigma}_2^+ - \hat{\sigma}_1^+\hat{\sigma}_2^-), \tag{4.47}$$

which takes the form of a Jaynes-Cummings style coherent exchange interaction through each detuned mode $\omega_k$ in the waveguide. In the formal master equation approach, these virtual exchange interactions form the final waveguide-mediated exchange Hamiltonian in Eq. 4.42 [45]

We show a clear picture for the origin of the exchange interaction between two-qubits spaced $d = \lambda/4$ along a common waveguide in Fig. 4-5. The qubit on the right, $\mathrm{Q}_2$, couples to the fields with wavelengths greater than $\lambda$, represented in blue, at points of positive amplitude in the instance of the illustration. The detuning of the blue field $\delta_\mathrm{b} = \omega - \omega_\mathrm{b}$, from the qubit frequency is positive, which yields a positive interaction strength $J(\omega_\mathrm{b}) = g^2(\omega_\mathrm{b})/\delta_\mathrm{b} > 0$. For fields with wavelengths less than $\lambda$, represented in green, $\mathrm{Q}_2$ couples to the fields at points of negative amplitude. The field shown in green has a negative detuning $\delta_\mathrm{g}$ from the qubit frequency, also yielding a positive interaction strength $J(\omega_\mathrm{g}) = g^2(\omega_\mathrm{g})/\delta_\mathrm{g} > 0$. The total exchange interaction strength results from an integral of $J(\omega_k)$ over all detuned modes ($\omega_k \neq \omega$). Because all detuned modes will have a virtual coupling of the same sign, we arrive at a net finite interaction strength of $J = \gamma/2$ between the two qubits.

We note that the dynamics of the system are identical for inter-qubit distances of $d = n\lambda/4$, where n is an odd integer. In the case of an inter-qubit distance of $d = \lambda/2$ discussed in Sec. 4.3, the virtual couplings have opposite signs for modes greater/less than the qubit frequency. The total exchange interaction after integration over all virtual couplings $J$ is zero. Next, we evaluate the scattering parameters, specifically the transmission and reflection coefficients, of a coherent probe incident upon the two-qubit system through the waveguide. Referencing the position of $\mathrm{Q}_1$ to $x_1 = 0$, the input-output relations from Eq. 3.62 are

$$\begin{aligned} \hat{a}_\mathrm{R}^\mathrm{out}(t) &= \hat{a}_\mathrm{R}^\mathrm{in}(t) + \sqrt{\frac{\gamma}{2}}(\hat{\sigma}_1^- - i\hat{\sigma}_2), \\ \hat{a}_\mathrm{L}^\mathrm{out}(t) &= \hat{a}_\mathrm{L}^\mathrm{in}(t) + \sqrt{\frac{\gamma}{2}}(\hat{\sigma}_1^- + i\hat{\sigma}_2). \end{aligned} \tag{4.48}$$

We use the steady-state density matrix to evaluate the coherences $\langle\hat{\sigma}_{1/2}^-\rangle = \mathrm{Tr}[\hat{\rho}\sigma_{1/2}^-]$. Assuming our input probe propagates to the right and $\langle\hat{a}_\mathrm{L}^\mathrm{in}\rangle = 0$, to first order of the input amplitude $\langle\hat{a}_\mathrm{R}^\mathrm{in}\rangle$, the transmission and reflection coefficients are

$$\begin{aligned} t &= \frac{\langle\hat{a}_\mathrm{R}^\mathrm{out}\rangle}{\langle\hat{a}_\mathrm{R}^\mathrm{in}\rangle} = \frac{J^2 - \delta^2 - (\gamma/2)^2}{J^2 - (\delta - i\gamma/2)^2} \\ r &= \frac{\langle\hat{a}_\mathrm{L}^\mathrm{out}\rangle}{\langle\hat{a}_\mathrm{R}^\mathrm{in}\rangle} = \frac{-|J|\gamma}{J^2 - (\delta - i\gamma/2)^2}, \end{aligned} \tag{4.49}$$

where $\delta = \omega - \omega_d$ is the qubit-drive detuning. For $J = \gamma/2$, we predict full extinction

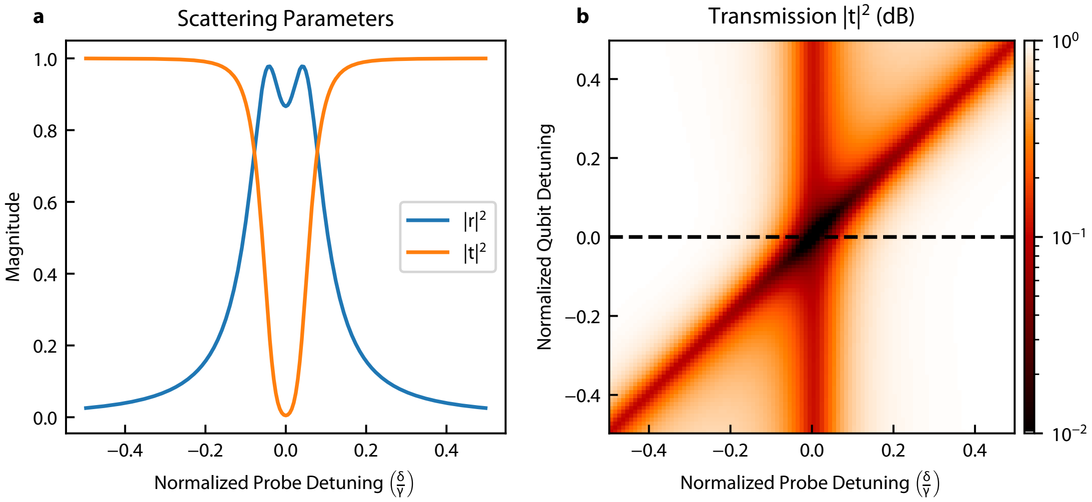

Figure 4-6: **Scattering parameters of two qubits coupled a waveguide at a distance of $d = \lambda/4$. a)** Simulated transmission and reflection of a coherent probe incident on the two qubits through the waveguide. In the ideal model without dephasing, non-radiative decay, or thermal photons, we should see perfect extinction in transmission. In this master equation simulation, we include a low, but non-zero, probe power that dresses the system, as reflected by the doublet structure in the reflection spectrum. **b)** Transmission simulation of the coherent probe as a function of probe detuning $\delta$ and qubit detuning $\Delta$ to visualize an avoided crossing of splitting $2J = \gamma$. Because the splitting is equal to the linewidth of each qubit frequency in the spectrum, the waveguide-mediated exchange interaction strength $J$ is difficult to resolve through avoided crossing spectroscopy. The dashed line for zero qubit detuning highlights the trace shown in (a).

in transmission for a resonant probe, as plotted in Fig. 4-6a. We see imperfect extinction and reflection in our master equation simulation, which we attribute to the non-zero probe power that dresses the two-qubit system.

Each qubit decays into the waveguide, and therefore appears in the spectrum as a Lorentzian curve with a linewidth of $\gamma$. Because the resonant qubits are coupled with strength $J$, we predict a splitting of the energy eigenstates $2J = \gamma$. In the dressed basis, the energy of the two eigenstates that describe the system differ by $2\sqrt{(\Delta/2)^2 + J^2}$, where $\Delta = \omega_2 - \omega_1$ is the qubit detuning. We simulate the eigenspectrum as a function of probe detuning $\delta$ and qubit detuning $\Delta$, shown in Fig. 4-6b. Because the qubit frequencies are split by $\gamma$, and they both have linewidth $\gamma$, the avoided crossing on resonance is difficult to resolve. Therefore, avoided crossing spectroscopy is not a precise method to measure the waveguide-mediated exchange coupling $J$ for any inter-qubit distance.

## 4.5 Timeline of wQED Experiments

Now that we have established the formalism to discuss qubit-waveguide interactions, we provide background on wQED experiments with superconducting circuits. We note that this is survey does not cover every relevant experiment in the last decade, but we discuss those that are most closely related to this thesis. While expanding fundamental quantum optics in a superconducting platform, these experiments build off of each other towards robust and extensible quantum computation and communication systems.

The first scattering measurements of a coherent probe incident on a superconducting qubit through a 1D coplanar waveguide, as discussed throughout Chapter 3, were demonstrated by Astafiev et al. in 2010 [32]. In this work, they observe resonance fluoresence, the absorption and reimmision of electromagnetic waves, with an artificial atom known as a flux qubit. This was a big step for the field of wQED in general, because the authors achieve efficient spatial-mode matching in the superconducting circuit platform and observe the interference effects discussed in Fig. 3-5. They also study inelastic scattering by measuring the power spectral density of the signal under a strong resonant drive through the waveguide. They observe the Mollow Triplet in the power spectrum, which highlights the transitions between the dressed states of the system [51]. Similarly, Abdumalikov et al. measure the time dynamics of a flux qubit coupled to a waveguide in 2011 [52]. They characterize the qubit-waveguide system by measuring the evolution of its coherent and incoherent emission. They send pump and readout pulses directly through the waveguide to measure population decay and coherence as a function of time.

The first demonstration of experimental state tomography of propagating microwave photons – a key measurement technique for wQED experiments – was conducted by Eichler et al. in 2011 [53]. Instead of coupling a transmon qubit directly to a single-ended waveguide, the authors use a transmission line resonator as an intermediary between the qubit and the waveguide. To prepare a single photon, the transmon qubit is excited when its frequency is far-detuned from the resonator. The qubit is then tuned to the resonator frequency for half of a Rabi oscillation, resulting in photon transfer to the resonator. The resonator decays into the single-ended waveguide, which routes the emitted photon to a phase-insensitive amplifier and quadrature amplitude detector. The authors establish a method to separate the amplified signal from the amplified noise and reconstruct the single-photon Fock states by analyzing the moments of the measured amplitude distribution. This is a key tool in experimental wQED and it is used throughout many future experiments to characterize the states of microwave photons.

In 2011, Hoi et al. extended the work of Astafiev et al. to demonstrate a microwave single-photon router using electromagnetically-induced transparency (EIT) [54]. The authors strongly couple a floating transmon qubit to a coplanar waveguide and input a weak coherent probe at the qubit frequency through the waveguide. They also apply a control tone at the frequency of the $|1\rangle \rightarrow |2\rangle$ transition of the transmon to determine whether their input probe is reflected or transmitted. If the control pulse is off, the input probe is reflected due to the interference effect we discuss in Fig. 3-5. A strong control tone dresses the qubit states, a phenomenon known as Autler-Townes splitting, and as a result, the authors observe full transmission of the input probe.

In 2012, Hoi et al. used the same device to study the statistics of the resonant field reflected by the transmon qubit [55]. They demonstrate that the scattered field is nonclassical with a Hanbury Brown and Twiss-type measurement, a classic experiment of quantum optics at with photons at visible wavelengths [56] and single-mode electrons [57]. The waveguide is effectively a beamsplitter for the qubit emission. By measuring the power at each end of the waveguide, the authors measure the second-order correlation between the two powers to verify the quantum nature of the reflected field.

In 2013, van Loo et al. demonstrate the interactions between two qubits coupled to a common waveguide mediated by both real and virtual photons [58]. This work implements the case studies discussed in this chapter of inter-qubit distances along the waveguide of $d = \lambda$ and $d = 3\lambda/4$ with two flux-tunable transmon qubits coupled to a common coplanar waveguide. To change the inter-qubit distance, the authors tune the qubit frequency. The authors measure the transmission, reflection, and power spectra of the system for both configurations of the inter-qubit distance. For $d = \lambda$, the authors observe superradiance in the transmission spectrum, as simulated in Fig. 4-4c. For $d = 3\lambda/4$, the authors also measure the expected transmission of the system and the avoided crossing we discuss in Fig. 4-6a/b respectively.

In 2015, Hoi et al. couple a transmon qubit to a waveguide terminated in a short circuit to create a mirror [59]. The qubit is physically located a specified distance away from the short circuit, and they can effectively tune this distance by changing the qubit frequency. This mirror creates a standing wave because of interference between the incoming and reflected field, with a voltage node at the short circuit of the waveguide. This voltage amplitude varies periodically along the waveguide, altering the structure of the continuum modes. The qubit decay rate into the waveguide varies as a function of the distance from the mirror. The authors measure the decay rate by probing the reflection spectrum as a function of qubit frequency. They show that when the qubit is coupled to a voltage node, the qubit is no longer coupled to the waveguide. The authors effectively shape the modes of the continuum with a mirror and demonstrate tunable qubit-waveguide coupling.

Extending upon the work in [59], Forn-Diaz et al. demonstrate a generator of shaped, single, microwave photons by coupling a fixed-frequency transmon qubit to a semi-infinite, or single-ended, transmission line [60] in 2017. The authors use a circuit set up similar to [59], except they use a dc-SQUID as a tunable inductive shunt at the end of the transmission line a certain distance away from the qubit. By tuning the flux through the dc-SQUID, they change the transmon-waveguide coupling by modifying the structure of the photonic continuum in the waveguide. To release a photon, they park the qubit at a voltage node of the standing wave determined by the boundary condition imposed by the dc SQUID, excite the transmon, and increase the transmon-waveguide coupling as a function of time to shape the released photon. This technical paper illustrates a theme/goal in the general quantum optics community of executing precise control over the wave-packet and propagation direction of single-photons. Microwave single-photons show promise as information carriers in quantum networks for robust quantum computation.

Following the theme of single-ended waveguides, in 2017, Gasparinetti et al. develop an excitation scheme for the emission of multiple correlated photons. They drive the two-photon $|0\rangle \rightarrow |2\rangle$ transition of a transmon coupled to a semi-infinite waveguide to generate two correlated photons at frequencies $\omega_{12}$ and $\omega_{01}$. The emission of the transmon in the waveguide is routed with an on-chip switch with a tunable center frequency to separate the two emitted photons by frequency into different paths. The authors measure power correlations between the two paths under a continuous drive at frequency $\omega_{02}$. The authors also measure the temporal wave-packet of of the individual photons and conduct photon state tomography following the scheme of [53] to fully characterize the quantum nature of the emitted photons.

In 2020, Mirhosseini et al. extend upon the work in [58] by designing a system of two qubits spaced at a distance of $d = \lambda/2$ apart along a waveguide. They insert a probe qubit halfway between the two qubits, such that the probe qubit is $d = \lambda/4$ away from each qubit along the waveguide. The probe qubit couples to the dark state formed by the two neighboring qubits at rate $J = \sqrt{\gamma\gamma_p/2}$ where $\gamma_p$ is the decay rate of the probe qubit into the waveguide. The dark state behaves as a cavity-like mode that couples to the qubit but does not decay into the waveguide. They perform transmission spectroscopy and time-domain measurements, such as Rabi oscillations between the probe qubit and the dark state, to characterize the three-qubit system. This work is a step towards exploring correlated decay at the many-body level.

In 2020, Besse et al. also use a qutrit to generate photonic states in a semi-infinite waveguide [61]. Their system is composed of a qutrit tunably coupled to an emitter qubit which decays directly into the single-ended waveguide. Through a sequence of single-qubit gates on the qutrit and two-qubit gates between the qutrit and the emitter, they generate a family of entangled states of photons, including cluster states, GHZ states, and W states. They perform photon state tomography to visualize the density matricies of these entangled states. This work has direct applications in cluster state-based quantum computation and state teleportation and communication with with GHZ and W states.

Since the onset of experimental wQED with superconducting circuits, these experiments continued to explore fundamental quantum optics in addition to their applications in quantum communication. In 2020, Kannan et al. design giant atoms by coupling a transmon qubit to a common waveguide at several specified locations/coupling points [62]. This approach implements an interference phenomenon that protects the qubit from decay into the waveguide while preserving waveguide-mediated exchange interactions. The authors find a decoherence-free frequency for a single giant atom, despite the qubit's interaction with the continuum of photonic modes in the bidirectional waveguide. Configurations of multiple qubits braided at different coupling points of the waveguide enable two-qubit gates to entangle the qubits. With this architecture, the mode of operation can be switched between a protected mode for high-fidelity qubit state preparation and an emissive mode for photon emission and applications in communication.

In 2020, Kannan et al. generate spatially entangled itinerant photons by coupling three emitter qubits to a common waveguide in [63]. They operate the device with two qubits at a time, in a configuration of an inter-qubit distance of either $d = 3\lambda/4$ or $d = \lambda/2$. The authors prepare both qubits in the excited state and study the distance-dependent interference of the simultaneous emission the qubits in the waveguide. Implementing the techniques in [53], the authors show a reconstructed density matrix of a variety of photonic entangled states.

Most of the wQED experiments thus far were conducted with 1D coplanar waveguides. In 2022, Zanner et al. coupled four floating transmon qubits to a three-dimensional rectangular waveguide. There are two pairs of qubits spaced $d = \lambda/2$ along the waveguide, where each qubit in a pair share a spatial location. Each pair is addressed with its own drive port to adjust the relative phase in the preparation of collective dark states. The two qubits in each pair have an effective inter-qubit distance of $d = 0$ and will form a bright and dark state, in addition to their local exchange interaction. Non-local pairs of qubits with an inter-qubit distance of $d = \lambda/2$ form bright and dark states as discussed in Sec. 4.3. The authors prepare a variety of many-body bright and dark states by exploiting local and waveguide-mediated interactions. They demonstrate long coherence times of many-body states in the presence of an open quantum system.

Throughout the last decade, wQED experiments have explored the interaction between superconducting qubits and the photonic modes in a continuum. Multiple qubits interact with each other through the common photonic continuum. Qubit-qubit interactions have been manipulated to generate propagating photons in waveguides, and photon state tomography has been developed to characterize photonic states and wQED systems. To control the propagation direction of photon emission, most of the experiments discussed rely on single-ended waveguides. The goal of the work in this thesis is to build off these ideas, and use qubit-waveguide systems to shape and direct propagating microwave photons in a bidirectional waveguide. We develop a device module that is in principle capable of photon directional photon emission and absorption, such that it forms the unit cell of an all-to-all, tileable quantum communication network.

# Chapter 5

# Directional Emission

## 5.1 Introduction

In recent years, directional emission into a waveguide has become a new sub-field of research known as chiral waveguide QED [9]. The chiral regime is naturally accessible within a nanophotonics platform, because the transverse confinement of light in optical nanowaveguides links the propagation direction of an emitted photon to the local polarization of an atom [9, 64]. This effect has been leveraged to achieve directional emission of optical photons in photonic waveguides and nanofibers [5–8]. However, to the best of our knowledge, directional emission of microwave photons into chiral waveguides for integration with circuit QED systems has not yet been demonstrated experimentally.

In this work, we experimentally demonstrate on-demand directional photon emission based on the quantum interference of indistinguishable photons emitted by a giant artificial molecule [33]. We arrange qubits that are spatially separated along a bidirectional waveguide to form a giant artificial molecule that can emit photons in a chosen direction [46, 47, 65, 66]. Effectively, we create a chiral waveguide by linking the propagation direction of an emitted photon to the relative phase of a two-qubit entangled state of the giant artificial molecule. We use quadrature amplitude detection to obtain the moments of the two output fields of the waveguide. Using these moments, we reconstruct the state of the photon and quantify its fidelity. The

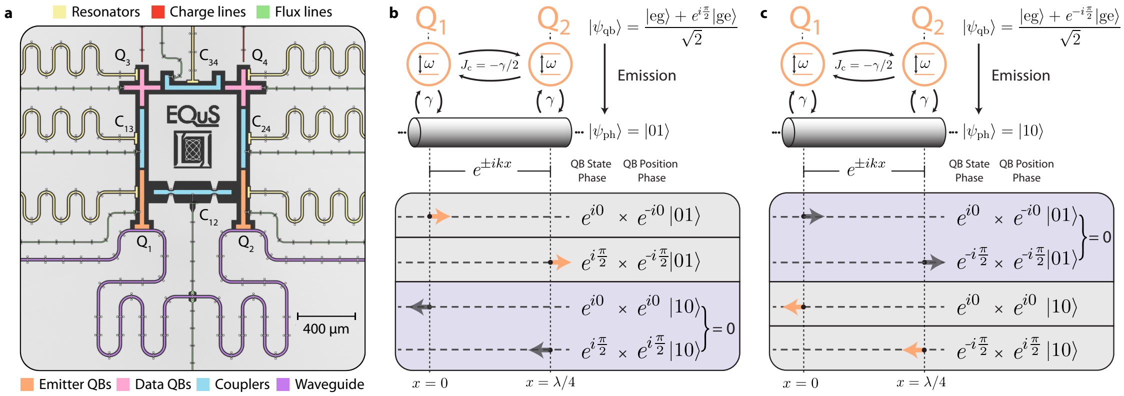

Figure 5-1: **Directional emission in a waveguide QED architecture. a)** A false-colored optical micrograph of the device. The state of the data qubits (pink) is transferred into the emitter qubits (orange) via an exchange interaction mediated by tunable couplers (blue). The emitter qubits continuously emit any population into the waveguide (purple). **b)** Schematic diagram of the two resonant emitter qubits $Q_1$ and $Q_2$ coupled to a common waveguide with equal strength $\gamma$ and inter-qubit distance $\lambda/4$. The phase delay for photons in the waveguide is given by $e^{\pm ikx}$, where $k = 2\pi/\lambda$ is the photon wavevector and $\lambda$ is the photon wavelength. The sign of this phase delay is determined by the propagation direction of the photon (+ for leftward, and − for rightward). An external coupler-mediated exchange interaction of strength $J_c = -\gamma/2$ is applied to fully cancel the waveguide mediated interaction between the qubits. The four possible coherent pathways for qubit emission into the left/right travelling modes of the waveguide are shown below. Each pathway obtains a phase from the initial state $|\psi_{\rm qb}\rangle$ and position $x$ of the qubit that emits the photon. When the qubits are initialized into $|\psi_{\rm qb}\rangle = (|eg\rangle + e^{i\pi/2}|ge\rangle)/\sqrt{2}$, the emitted photon only propagates towards the right due to destructive interference between the left-propagating pathways. **c)** The same setup as (b), but with the initial qubit state $|\psi_{\rm qb}\rangle = (|eg\rangle + e^{-i\pi/2}|ge\rangle)/\sqrt{2}$. In this case, the right-propagating pathways destructively interfere, and the emitted photon only propagates towards the left.

architecture realized here can be used for both photon emission and absorption [47], thus this demonstration is the first step towards implementing an interconnect for an extensible quantum network.

## 5.2 Model and Protocol

Our device comprises four frequency-tunable transmon qubits [40] and four tunable transmon couplers [67,68] between each neighboring qubit pair, as shown in Fig. 5-1a. The artificial molecule is composed of two identical resonant qubits $Q_1$ and $Q_2$, with frequencies $\omega_1/2\pi = \omega_2/2\pi = 4.93$ GHz and decay into a common waveguide at the rate $\gamma/2\pi = 3.2$ MHz. The qubits are spatially separated along the waveguide by a distance $\Delta x = \lambda/4$, where $\lambda$ is the wavelength of the emitted photon, following the model described in Sec. 4.4. The other two qubits, $\mathrm{Q}_3$ and $\mathrm{Q}_4$, serve as data qubits that are not subject to direct dissipation into the waveguide. These qubits would function as the interface between a quantum processor and the emitter qubits within a computational node in a quantum network. Because the data qubits are distant from the waveguide, the state of $\mathrm{Q}_3$ and $\mathrm{Q}_4$ can be prepared with high fidelity with a combination of single- and two-qubit gates. We generate photons by transferring the state of the data qubits $\mathrm{Q}_{3/4}$ to the emitter qubits $\mathrm{Q}_{1/2}$ via an exchange interaction mediated by the couplers $\mathrm{C}_{13/24}$.

The directional emission protocol relies on the dynamics of the sub-system of the emitter qubits $\mathrm{Q}_{1/2}$ and the waveguide. From the derivation of Eq. 4.42 in Sec. 4.4, the master equation governing the time dynamics of the resonant emitter qubits with identical decay rates into the waveguide $\gamma$ and inter-qubit distance $\Delta x = \lambda/4$ [45,47]:

$$\frac{\partial \hat{\rho}}{\partial t} = -i\big[\hat{H}_{\mathrm{qb}} + \hat{H}_{\mathrm{c}}, \hat{\rho}\big] + \gamma \sum_{j}^{2} D\big[\hat{\sigma}_j^-\big]\hat{\rho}, \tag{5.1}$$

where $\hat{\rho}$ is the density matrix of the sub-system, $D[\hat{O}] = \hat{O}\hat{\rho}\hat{O}^\dagger - \frac{1}{2}\{\hat{O}^\dagger\hat{O}, \hat{\rho}\}$ is the Lindblad dissipator, $\hat{H}_{\mathrm{qb}} = \sum_j^2 \omega_j \hat{\sigma}_j^+\hat{\sigma}_j^-$ is the free-qubit Hamiltonian of the emitters, setting $\hbar$ to unity for simplicity, and $\hat{\sigma}_j^\pm$ are the raising and lowering Pauli operators of each qubit with $j \in \{1, 2\}$.

Finally, $\hat{H}_{\mathrm{c}} = (\gamma/2 + J_{\mathrm{c}})(\hat{\sigma}_1^+\hat{\sigma}_2^- + \hat{\sigma}_2^+\hat{\sigma}_1^-)$ is the total coherent exchange interaction Hamiltonian between the emitters. There are two sources coherent emitter-emitter coupling:

1. A static waveguide-mediated interaction of strength $\gamma/2$. This coherent coupling of qubits through the modes in the waveguide is characteristic of resonant, identical two-qubit systems with inter-qubit distance $\Delta x = \lambda/4$ along a common waveguide, as seen in Eq. 4.39.

2. A tunable-coupler-mediated interaction between the emitter qubits (via $\mathrm{C}_{12}$) of strength $J_\mathrm{c}$. The tunability in $J_\mathrm{c}$ is used to cancel the waveguide-mediated interaction such that the emitters are decoupled from each other and the exchange Hamiltonian $\hat{H}_\mathrm{c} = 0$. The emitter qubits must not exchange population during emission into the waveguide to avoid disrupting the interference effect that enables the directional emission protocol illustrated in Fig. 5-1b/c.

The final state of the photons emitted by $\mathrm{Q}_1$ and $\mathrm{Q}_2$ depends on the interference between their simultaneous emission. Specifically, when the initial state of the emitter qubits is

$$|\psi^\pm\rangle = \frac{|eg\rangle + e^{\pm i\frac{\pi}{2}}|ge\rangle}{\sqrt{2}}, \tag{5.2}$$

the artificial atom emits a single photon that propagates either leftward or rightward, depending on the sign of the relative phase of the initial entangled state. To see this, consider the emitter qubits initialized to $|\psi_\mathrm{qb}\rangle = |\psi^+\rangle$, as shown in Fig. 5-1b. For simplicity, we define the positions of $\mathrm{Q}_1$ and $\mathrm{Q}_2$ along the waveguide to be $x = 0$ and $x = \Delta x$, respectively. Here, $k = 2\pi/\lambda$ is the wavevector of the emitted photon, and the sign of the phase $e^{\pm ikx}$ is determined by the propagation direction of the photon (+ for leftward, and − for rightward). We denote the state of the emission from the emitter qubits as $|\psi_\mathrm{ph}\rangle = |n_\mathrm{L} n_\mathrm{R}\rangle$, where $n_\mathrm{L(R)}$ is the number of photons propagating to the left (right) in the waveguide. There are four possible emission pathways from the initial state $|\psi_\mathrm{qb}\rangle = |\psi^+\rangle$ as shown in Fig. 5-1b, each involving one of the emitter qubits, $\mathrm{Q}_1$ or $\mathrm{Q}_2$, releasing a photon that propagates towards the left or the right:

1. If $\mathrm{Q}_1$ emits a rightward-propagating photon, the emission accumulates phases from both the relative phase of $e^{i0}$ from the state $|\psi^+\rangle$ and a phase $e^{-ikx} = e^{-i0}$ given by the position of $\mathrm{Q}_1$ at $x = 0$. The resulting state of the photon emission is $|\psi_\mathrm{ph}\rangle = e^{i0}|01\rangle$.

2. If $\mathrm{Q}_2$ emits a rightward-propagating photon, the emission accumulates the relative phase of $e^{i\pi/2}$ from the state $|\psi^+\rangle$ and a phase $e^{-ikx} = e^{-i\pi/2}$ given by the position of $\mathrm{Q}_2$ at $x = \lambda/4$. The total phase accumulated by the rightward emission from $\mathrm{Q}_2$ is also $e^{i0}$, resulting in the state $|\psi_\mathrm{ph}\rangle = e^{i0}|01\rangle$.

3. If $Q_1$ emits a leftward-propagating photon, the state phase and position phase are both $e^{i0}$, and the resulting state of the emission is $|\psi_{\mathrm{ph}}\rangle = e^{i0}|10\rangle$.

4. If $Q_2$ emits a leftward-propagating photon, the emission accumulates the relative state phase of $e^{i\pi/2}$ and a position phase of $e^{+ikx} = e^{i\pi/2}$. The total phase accumulated by the leftward emission from $Q_2$ is $e^{i\pi}$, resulting in the state $|\psi_{\mathrm{ph}}\rangle = e^{i\pi}|10\rangle$.

These additional phases result in the total constructive interference between rightward emission pathways and the total destructive interference between leftward emission pathways. Therefore, when the qubits are initialized into $|\psi^+\rangle$ , the emitted photon always propagates to the right, as described by the state $|\psi_{\mathrm{ph}}\rangle = |01\rangle$. If the emitter qubits are instead initialized into the state $|\psi_{\mathrm{qb}}\rangle = |\psi^-\rangle$, a similar analysis, as shown in Fig. 5-1c, results in a leftward propagating photon in the state $|\psi_{\mathrm{ph}}\rangle = |10\rangle$.

The directional emission of photons from this system of entangled emitter qubits can be formally verified using the input-output relations for leftward- and rightward-propagating modes in the waveguide, as discussed in the derivation of Eq. 4.48: [45]

$$\begin{aligned}\hat{a}_{\mathrm{L}} &= \hat{a}_{\mathrm{L}}^{\mathrm{in}} + \sqrt{\frac{\gamma}{2}}(\hat{\sigma}_1^- + \hat{\sigma}_2^- e^{ik\Delta x}) = \hat{a}_{\mathrm{L}}^{\mathrm{in}} + \sqrt{\frac{\gamma}{2}}(\hat{\sigma}_1^- + i\hat{\sigma}_2), \\ \hat{a}_{\mathrm{R}} &= \hat{a}_{\mathrm{R}}^{\mathrm{in}} + \sqrt{\frac{\gamma}{2}}(\hat{\sigma}_1^- + \hat{\sigma}_2^- e^{-ik\Delta x}) = \hat{a}_{\mathrm{R}}^{\mathrm{in}} + \sqrt{\frac{\gamma}{2}}(\hat{\sigma}_1^- - i\hat{\sigma}_2^-).\end{aligned} \tag{5.3}$$

Here, $\hat{a}_{\mathrm{L(R)}}^{\mathrm{in}}$ represents the input field of photons propagating to the left (right) in the waveguide. From these relations, the number of photons in either mode of the waveguide, or the photon flux, $\langle \hat{n}_{\mathrm{L(R)}} \rangle = \langle \hat{a}_{\mathrm{L(R)}}^\dagger \hat{a}_{\mathrm{L(R)}} \rangle$, can be directly related to the state of the qubits. For zero input field ($\hat{a}_{\mathrm{L(R)}}^{\mathrm{in}} = 0$), the number of photons emitted to either the left or right in the waveguide is

$$\begin{aligned}\langle \hat{n}_{\mathrm{L}} \rangle &= \frac{\gamma}{2}(\langle \sigma_1^+ \sigma_1^- \rangle + \langle \sigma_2^+ \sigma_2^- \rangle - i\langle \sigma_2^+ \sigma_1^- \rangle + i\langle \sigma_1^+ \sigma_2^- \rangle) \\ \langle \hat{n}_{\mathrm{R}} \rangle &= \frac{\gamma}{2}(\langle \sigma_1^+ \sigma_1^- \rangle + \langle \sigma_2^+ \sigma_2^- \rangle + i\langle \sigma_2^+ \sigma_1^- \rangle - i\langle \sigma_1^+ \sigma_2^- \rangle)\end{aligned} \tag{5.4}$$

For the emitter qubit state $|\psi_{\mathrm{qb}}\rangle = |\psi^+\rangle$, we find the leftward photon flux $\langle \hat{n}_{\mathrm{L}} \rangle = 0$

and rightward photon flux $\langle \hat{n}_{\mathrm{R}} \rangle = \gamma$. Alternatively, for $|\psi_{\mathrm{qb}}\rangle = |\psi^-\rangle$, we find $\langle \hat{n}_{\mathrm{R}} \rangle = 0$ and $\langle \hat{n}_{\mathrm{L}} \rangle = \gamma$, formally verifying the discussion in Fig. 5-1b/c. These photon fluxes encapsulate the physics of the directional emission protocol.

Given that the emitters are initialized into $|\psi_{\mathrm{qb}}\rangle = |\psi^{\pm}\rangle$, the interference described above is only perfect when $\Delta x = (2m+1)\lambda/4$, where $m$ is an integer, and the external tunable coupling $J_{\mathrm{c}} = -\gamma/2$. The first condition ensures that the interfering emission pathways are fully in/out of phase. In our system, we choose $m = 0$ such that the emitter qubits have an inter-qubit distance along the waveguide of $\Delta x = \lambda/4$. The propagation directions of the photons emitted by the states $|\psi_{\mathrm{qb}}\rangle = |\psi^{\pm}\rangle$ alternate for even and odd $m$. Additionally, for this inter-qubit distances $\Delta x$, the qubits do not experience correlated dissipation [45], which would further disrupt the interference during the emission process. The second condition on the external tunable coupling, $J_{\mathrm{c}} = -\gamma/2$, prevents any population transfer between the qubits during the emission process by setting the exchange Hamiltonian $\hat{H}_{\mathrm{c}}$ to zero.

## 5.3 Device Calibration

The strong and always-on dissipation into the waveguide makes it difficult to measure the strength of the coupling between the emitters, $J_{\Sigma} = \gamma/2 + J_{\mathrm{c}}$. The typical methods, such as observations of avoided crossings in qubit spectroscopy as discussed in Fig. 4-6b, or population exchange in time domain as simulated in Fig. 4-1b, are limited in resolution for small total emitter coupling $J_{\Sigma} < \gamma$. To go beyond this limit, we infer the value of $J_{\Sigma}$ by measuring the elastic scattering of a weak input probe tone incident on the emitter qubits through the waveguide. Specifically, we measure the transmission amplitude $S_{21}$ of a coherent tone as a function of the detuning between the emitter qubit frequencies, $\Delta = \omega_2 - \omega_1$, and the detuning between the probe and $\mathrm{Q}_1$ frequencies, $\delta = \omega_p - \omega_1$, as shown in Fig. 5-2a. When the qubits are detuned ($\Delta > \gamma$), they will each act as a mirror to single photons at their respective frequencies (see discussion in Sec. 3.5) [32, 48, 54], such that there are two dips in $|S_{21}(\delta)|$. This is a consequence of the destructive interference between the probe and the forward-

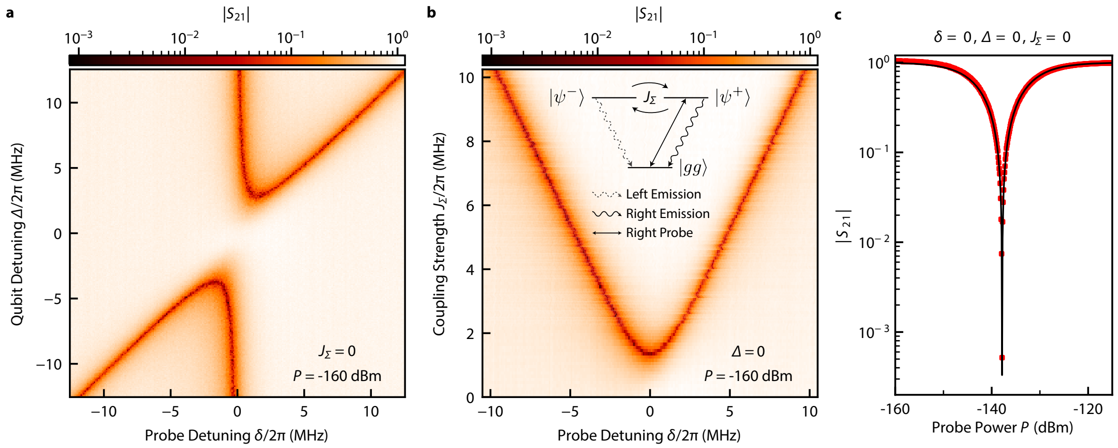

Figure 5-2: **Verifying protocol conditions via elastic scattering. a)** The transmittance $|S_{21}|$ of an input probe tone incident upon the two emitter qubits $\mathrm{Q}_1$ and $\mathrm{Q}_2$ through the waveguide. $|S_{21}|$ is plotted as a function $\Delta$, the detuning of $\mathrm{Q}_2$ from $\mathrm{Q}_1$, and $\delta$, the detuning between the probe and $\mathrm{Q}_1$. In the case of far detuned emitters ($\Delta > \gamma$), each qubit acts as a mirror ($|S_{21}| \ll 1$) to a resonant probe ($\delta = 0$ or $\delta = \Delta$), as discussed in Sec. 3.5. However, for resonant emitters ($\Delta = 0$), the transmittance returns to unity and the emitters are effectively transparent to fields in the waveguide. **b)** $|S_{21}|$ as a function of the total coupling strength $|J_\Sigma|$ and $\delta$ while $\mathrm{Q}_1$ and $\mathrm{Q}_2$ are resonant, using the same probe power as in (a). The level diagram of the three states $|gg\rangle$, $|\psi^+\rangle$, and $|\psi^-\rangle$ is shown as an inset ($|ee\rangle$ is ignored for weak probes). The rightward-propagating probe used to obtain this data only couples the states $|gg\rangle \leftrightarrow |\psi^+\rangle$, and a finite exchange interaction between the emitters will couple $|\psi^+\rangle \leftrightarrow |\psi^-\rangle$. The state $|\psi^+\rangle$ can only emit a rightward-propagating photon and $|\psi^-\rangle$ can only emit a leftward-propagating photon. We observe two dips in the transmission at $\delta = \pm J_\Sigma$, corresponding to the energy splitting from the hybridization of $|\psi^\pm\rangle$. When $|J_\Sigma| \to 0$, the transmission approaches unity for all $\delta$ because the probe can only excite the $|\psi^+\rangle$ state, which can only emit in the same direction (right) as the probe. This measurement is used to set $|J_\Sigma| = 0$. **c)** The measured $|S_{21}|$ (red points) as a function of the probe power with $\Delta = 0$, $\delta = 0$, and $J_\Sigma = 0$. The data agrees well with a fit (black curve) to a simulation of the master equation in Eq. 5.1.

propagating, out-of-phase emission of the driven qubit. Therefore, $|S_{21}|$ is suppressed for weak coherent inputs (average photon number $\ll 1$) that are resonant with either qubit.

The elastic scattering behavior changes when the emitter qubits are resonant ($\Delta = 0$). First, given that the qubits are equally coupled to the waveguide at rate $\gamma$, the input probe tone will only drive the $|gg\rangle \leftrightarrow |\psi(\phi)\rangle$ and $|\psi(\phi)\rangle \leftrightarrow |ee\rangle$ transitions, where $|\psi(\phi)\rangle = (|eg\rangle + e^{i\phi}|ge\rangle)/\sqrt{2}$. The sign of $\phi = \pm k\Delta x$ is determined by the propagation direction of the probe. Furthermore, the transition to the joint excited state $|ee\rangle$ can be ignored for low probe powers $P$, as it requires an appreciable population in $|\psi(\phi)\rangle$ to play a role. Therefore, if $\Delta x = \lambda/4$ and $\hat{H}_{\mathrm{c}} = 0$, the state of the qubits are driven into a mixture of only $|gg\rangle$ and either $|\psi^{+}\rangle$ or $|\psi^{-}\rangle$, depending on the direction of the probe. However, these states can only re-emit photons in the same direction as the input, as depicted in the level-diagram in Fig. 5-2b for a rightward-propagating probe. This ideally results in perfect transmission, $|S_{21}(\Delta = 0)| = 1$, and the emitters are effectively transparent to fields in the waveguide.

The magnitude of the transmission deviates from unity if the emitters experience non-zero coupling, $\hat{H}_{\mathrm{c}} \neq 0$, as any population transfer between $|\psi^{+}\rangle \leftrightarrow |\psi^{-}\rangle$ causes part of the qubit emission to propagate in the direction opposite to that of the probe. To verify this, we measure $|S_{21}(\Delta = 0)|$ as a function of $|J_{\Sigma}|$ in Fig. 5-2b. For $|J_{\Sigma}| > \gamma/2$ we see two dips in the transmission at $\delta = \pm J_{\Sigma}$, which now correspond to the hybridized energy splitting of $|\psi^{+}\rangle$ and $|\psi^{-}\rangle$. For $|J_{\Sigma}| < \gamma/2$, the energy splitting is within the linewidth of the qubits, which is set by $\gamma$. However, as described above, we observe the $|S_{21}(\delta)| \to 1$ as $J_{\Sigma} \to 0$. Therefore, we can use the transmission as a metric to set $J_{\Sigma} = 0$ and ensure the emitter qubits are uncoupled despite the large decay rate $\gamma$ of these qubits.

Finally, in Fig. 5-2c we show the transmission $|S_{21}(\Delta = 0, \delta = 0, J_{\Sigma} = 0)|$ as a function of the probe power. Here, we clearly see $|S_{21}| \approx 1$ for low powers, as previously discussed. We observe that $|S_{21}|$ slightly exceeds unity for low probe powers, which we attribute to impedance mismatches in our experimental setup

We use a master equation model to simulate the steady-state dynamics of both emitter qubits $\mathrm{Q}_1$ and $\mathrm{Q}_2$ of frequencies $\omega_1$ and $\omega_2$ at positions $x_1$ and $x_2$ along the waveguide. In order to calibrate the device, we perform a series of elastic scattering measurements discussed in Fig. 5-2. In the frame of the probe, the system Hamiltonian is [45]

$$\hat{H} = \hat{H}_{\mathrm{qb}} + \hat{H}_{\mathrm{p}} + \hat{H}_{\mathrm{c}} = \sum_{j}^{2} [\delta_j \hat{\sigma}_j^{+} \hat{\sigma}_j^{-} + \Omega_{\mathrm{p}} (\hat{\sigma}_j^{+} e^{-ikx_j} + \hat{\sigma}_j^{-} e^{ikx_j})] + J_{\Sigma} (\hat{\sigma}_1^{+} \hat{\sigma}_2^{-} + \hat{\sigma}_2^{+} \hat{\sigma}_1^{-}) \quad (5.5)$$

where $\delta_j = \omega_j - \omega_{\mathrm{p}}$ is the probe detuning from each qubit frequency. The total emitter-emitter coupling is $J_\Sigma = \gamma/2 + J_{\mathrm{c}}$, where $J_{\mathrm{c}}$ is the coupling induced by tunable coupler $\mathrm{C}_{12}$ as discussed in the main text. We define the positions of the emitters as $x_1 = 0$ and $x_2 = \lambda/4$, where $\lambda$ is the wavelength of the qubit emission in the waveguide. The master equation of the driven qubit system is

$$\partial_t \hat{\rho} = -i\big[\hat{H}, \hat{\rho}\big] + \sum_j^2 \left(\gamma D\big[\hat{\sigma}_j^-\big]\hat{\rho} + \frac{\gamma_{\phi,j}}{2} D\big[\hat{\sigma}_{z,j}\big]\hat{\rho}\right). \tag{5.6}$$

For a rightward-propagating input probe with average field amplitude $\langle \hat{a}_{\mathrm{R}}^{\mathrm{in}} \rangle = \sqrt{\frac{P}{\hbar\omega_{\mathrm{p}}}}$, the input-output relations of the driven two-qubit system are

$$\begin{aligned} \langle \hat{a}_{\mathrm{L}} \rangle &= \sqrt{\frac{\gamma}{2}} \left(\langle \hat{\sigma}_1^- \rangle + i\langle \hat{\sigma}_2^- \rangle\right), \\ \langle \hat{a}_{\mathrm{R}} \rangle &= \langle \hat{a}_{\mathrm{R}}^{\mathrm{in}} \rangle + \sqrt{\frac{\gamma}{2}} \left(\langle \hat{\sigma}_1^- \rangle - i\langle \hat{\sigma}_2^- \rangle\right). \end{aligned} \tag{5.7}$$

We use numerical master equation simulations to determine the transmission amplitude $S_{21} = \langle \hat{a}_{\mathrm{R}} \rangle / \langle \hat{a}_{\mathrm{R}}^{\mathrm{in}} \rangle$ as a function of probe detuning $\delta$, emitter detuning $\Delta$, and the total emitter-emitter coupling $J_\Sigma$ as shown in Fig. **??**. We also simulate the transmission of a resonant probe as a function of probe power as shown in Fig. 5-2c. The simulations mirror our calibration spectroscopic experiments, indicating that this model captures the steady-state dynamics of the driven two-qubit system.

We experimentally find the $|J_\Sigma| = 0$ point by varying the frequency of the tunable coupler $C_{12}$, which in turn adjusts the net interaction between the two emitter qubits. In particular, we measure $|S_{21}|$ for when the input probe is resonant with both emitter qubits $\delta = 0$ while sweeping the frequency of $C_{12}$, as shown in Fig. 5-3a. The frequency for which $|S_{21}|$ is maximized corresponds to the operating point when $|J_\Sigma|$ is minimized, and is ideally zero. To see this more clearly, we map the frequency of $C_{12}$ onto $J_\Sigma$ (see Refs. [67,68]) in Fig. 5-3b. For the plotted range ($J_\Sigma \in [-\gamma/2, \gamma/2]$, we can clearly see that $|S_{21}|$ is maximized when $J_\Sigma = 0$. Note that the $|S_{21}|$ slightly exceed unity at its maximum value, which we attribute to impedance mismatches

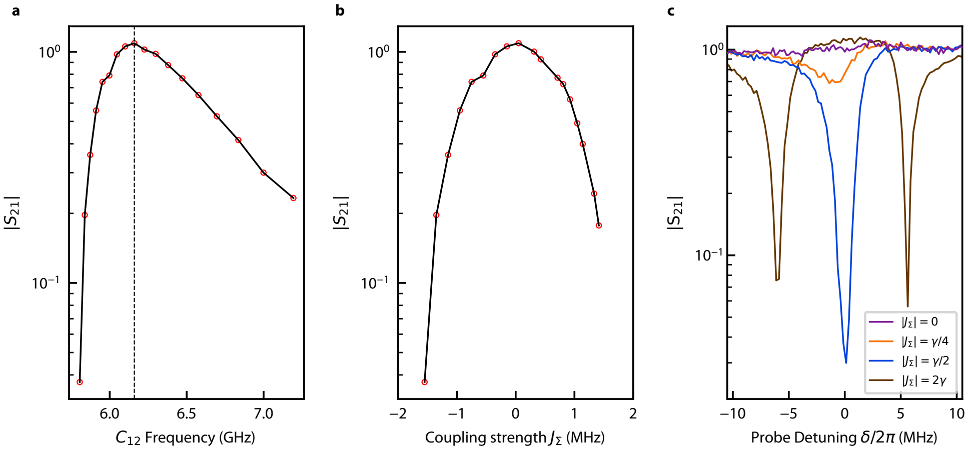

Figure 5-3: **Cancelling coupling between emitter qubits. a)** The transmission $|S_{21}|$ as a function of the frequency of the tunable coupler $C_{12}$ for resonant emitters. The coupling between the two emitter qubits is tuned via the frequency $C_{12}$, and the point of highest $|S_{21}|$ corresponds to the point of operation for a net-zero interaction between these qubits. **b)** The same data presented in (a), but with the frequency of $C_{12}$ mapped onto the net coupling strength $J_\Sigma$. For the range $J_\Sigma \in [-\gamma/2, \gamma/2]$, $|S_{21}|$ is maximal at $J_\Sigma = 0$. **c)** Four representative traces of $|S_{21}|$ as a function of the detuning $\delta$ between the probe and resonant emitter qubits. A clear splitting splitting can be seen for $|J_\Sigma| = 2\gamma$. The $|S_{21}|$ approaches unity for all $\delta$ as $|J_\Sigma|$ approaches 0.

in our experimental setup [69, 70]. Finally, we plot $|S_{21}|$ as a function of the probe detuning $\Delta$ from the emitter qubits in Fig. 5-3c. We show four representative traces for different values of $|J_\Sigma|$. When $|J_\Sigma| > \gamma/2$, we observe a splitting from the hybridization of the qubits. However, when $|J_\Sigma| < \gamma/2$ we simply observe a single dip that shallows as the coupling decreases.

## 5.4 Photon Generation and Measurement

Now that we have met the conditions required to observe directional photon emission, we now run the full protocol using the pulse sequence shown in Fig. 5-4a. The emitter qubits continuously dissipate into the waveguide resulting in low coherence and low-fidelity state preparation. Instead of directly preparing the initial state of the emitter qubits into $|\psi^\pm\rangle$, we initialize the data qubits $Q_3$ and $Q_4$. The data qubits have longer lifetimes because they are not directly coupled to the waveguide, and we can

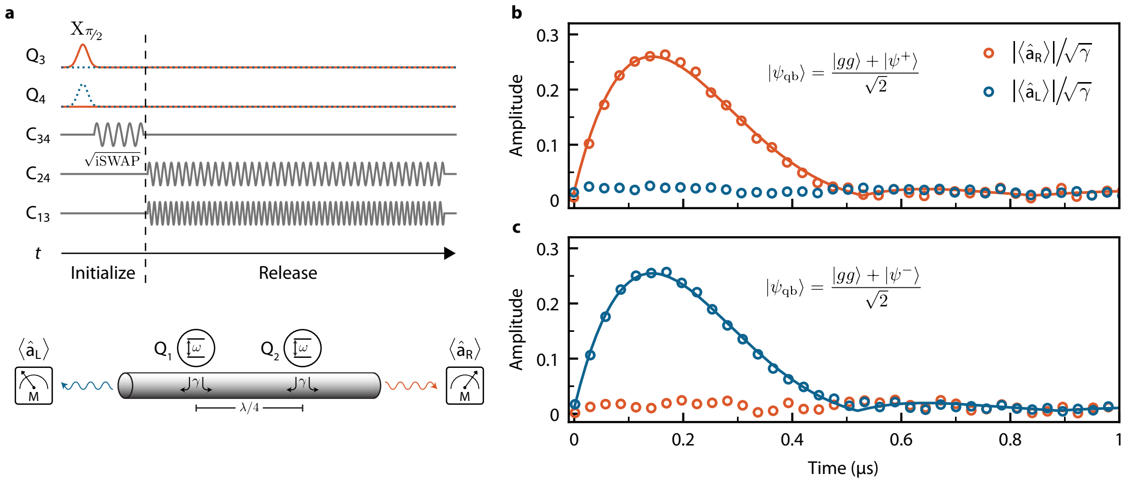

Figure 5-4: **Pulse sequence and time-domain measurements.** **a)** The pulse sequence for generating a photon. The qubit state initialization begins by exciting either Q$_3$ (orange solid curve) or Q$_4$ (blue dashed curve). These qubits are then entangled via a $\sqrt{\text{iSWAP}}$ gate by parametrically modulating the frequency of the tunable coupler C$_{34}$ at the detuning of Q$_3$ and Q$_4$. Finally, a photon is released via a parametric exchange interaction between the data qubits Q$_{3/4}$ and the emitter qubits Q$_{1/2}$. The measurement schematic below the pulse-sequence shows that the field amplitudes $\hat{a}_{\text{L/R}}$ are measured at both outputs of the waveguide. **b)** The measured (circles) time-dependent field amplitudes for a photon emitted towards the right. The data is fit (solid curve) using the solution to the master equation in Eq. 5.8. The initial state of the data qubits is $|\psi_{\text{qb}}\rangle = (|gg\rangle + |\psi^+\rangle)/\sqrt{2}$. The field amplitude of the leftward emission channel is nearly zero. This data is averaged over $1.5 \times 10^7$ repetitions. **c)** The same measurement as (b), but with $|\psi_{\text{qb}}\rangle = (|gg\rangle + |\psi^-\rangle)/\sqrt{2}$ such that the emitted photon now propagates to the left.

faithfully prepare them into an entangled state with high fidelity. We describe the directional photon emission pulse sequence:

1. Detune data qubits - we first detune Q$_3$ and Q$_4$ ($\Delta_{34} = |\omega_3 - \omega_4|$) such that they are decoupled. Both data qubits are detuned from the emitters ($\Delta_{13} = |\omega_1 - \omega_3|$ and $\Delta_{24} = |\omega_2 - \omega_4|$).

2. Introduce excitation - we excite Q$_3$ with a $\pi$-pulse to emit a photon to the right. To emit a photon to the left, we excite Q$_4$ with a $\pi$-pulse instead.

3. Entangle data qubits - we implement a parametric $\sqrt{\text{iSWAP}}$ gate between Q$_3$ and Q$_4$ by modulating the frequency of the tunable coupler C$_{34}$ at the detuning $\Delta_{34}$ to prepare the entangled state $|\psi^{\pm}\rangle$ [71]. We note that we prepare the data

qubits into the state $|\psi^+\rangle$ when we excite $\mathrm{Q}_3$, or $|\psi^-\rangle$ when we excite $\mathrm{Q}_4$ in step 2.

4. Transfer $|\psi^\pm\rangle$ to the emitter qubits - we execute parametric exchange interactions with the tunable couplers $\mathrm{C}_{13}$ and $\mathrm{C}_{24}$. We modulate the frequency of the tunable couplers at the detunings $\Delta_{13}$ and $\Delta_{24}$ respectively. The shape of the emitted photon is determined by both the parametrically induced coupling $g_{\mathrm{eff}}$ between the qubit pairs $\mathrm{Q}_{1/2} \leftrightarrow \mathrm{Q}_{3/4}$ and the emitter-waveguide coupling strength $\gamma$.

5. Emission and interference in the waveguide - the interference process described in Fig. 5-1 results in a photon propagating in the direction of choice.

In the following sections, we study the temporal dynamics of the photon field amplitudes. We also dig deeper into the details of the parametric exchange interactions that are key the directional emission protocol.

### 5.4.1 Temporal Dynamics

Next, we seek to study the temporal dynamics of the photon by measuring the field amplitude at each end of the waveguide $\hat{a}_{\mathrm{L/R}}(t)$ as illustrated in Fig. 5-4a. In practice, we measure amplified voltage signals in the time-domain which are proportional to the field amplitudes $\hat{a}_{\mathrm{L/R}}(t)$. The average field amplitudes are zero for the single-photon Fock state that results from the emission protocol $\langle 1_{\mathrm{L/R}}|\hat{a}_{\mathrm{L/R}}(t)|1_{\mathrm{L/R}}\rangle = 0$. This is because the photon is emitted with random phase, which averages to zero upon repeated measurements. The average field amplitude is only non-zero when there is finite coherence between the vacuum state $|00\rangle$ and a single photon state $|01\rangle$ or $|10\rangle$. Therefore, to measure non-zero field amplitudes, we initially excite $\mathrm{Q}_3$ ($\mathrm{Q}_4$) with a $\frac{\pi}{2}$-pulse, such that the emitted photon will be in the state $|\psi_{\mathrm{ph}}\rangle = [|00\rangle + |01\rangle]/\sqrt{2}$ ($|\psi_{\mathrm{ph}}\rangle = [|00\rangle + |10\rangle]/\sqrt{2}$). We can now observe the temporal envelope of the photon wavepacket, as shown in Figs. 5-4b and 5-4c. The amplitude of the photon is non-zero in the direction determined by the phase in the initial state of $\mathrm{Q}_3$ and $\mathrm{Q}_4$. This is a signature of the controlled directional emission.

Next, we seek to derive an analytical form of the temporal envelope of the photon when we prepare the data qubits in the state $|\psi^{\pm}_{\text{qb}}\rangle = (|gg\rangle + |\psi^{\pm}\rangle)/\sqrt{2}$. The state of the data qubits is then transferred to the emitter qubits with parametric exchange interactions as part of the photon release protocol. The four-qubit master equation that describes this system is written as

$$\partial_t \hat{\rho} = -i[\hat{H}, \hat{\rho}] + \sum_{k=1,2} \hat{c}_k \hat{\rho} \hat{c}_k^{\dagger} - \frac{1}{2}\{\hat{c}_k^{\dagger}\hat{c}_k, \hat{\rho}\}, \tag{5.8}$$

where

$$\hat{H} = g_{\text{eff}}\,(\hat{\sigma}_3^{-}\hat{\sigma}_1^{+} + \hat{\sigma}_3^{+}\hat{\sigma}_1^{-}) + g_{\text{eff}}\,(\hat{\sigma}_4^{-}\hat{\sigma}_2^{+} + \hat{\sigma}_4^{+}\hat{\sigma}_2^{-}), \tag{5.9}$$

is the system's Hamiltonian and

$$\hat{c}_k \in \{\sqrt{\gamma}\hat{\sigma}_1^{-}, \sqrt{\gamma}\hat{\sigma}_2^{-}\}, \tag{5.10}$$

are the collapse operators, which represent the decay of the emitter qubits into the waveguide. The raising and lowering operators of each qubit $\mathrm{Q}_i$ is denoted as $\hat{\sigma}_i^{\pm}$, where $i \in \{1, 2, 3, 4\}$ is the qubit number.

We work in the superoperator representation of Eq. 5.8. Vectorizing the density matrix as $\hat{\rho} \to |\rho\rangle\rangle$, we rewrite the master equation as

$$\partial_t |\rho\rangle\rangle = \hat{\mathcal{L}} |\rho\rangle\rangle, \tag{5.11}$$

where $\hat{\mathcal{L}}$ is the Liouvillian superoperator [72]

$$\hat{\mathcal{L}} = -i\left(\mathbb{1} \otimes \hat{H} - \hat{H}^{T} \otimes \mathbb{1}\right) + \sum_k \hat{c}_k^{*} \otimes \hat{c}_k - \frac{1}{2}\left(\mathbb{1} \otimes \hat{c}_k^{\dagger}\hat{c}_k + \hat{c}_k^{T}\hat{c}_k^{*} \otimes \mathbb{1}\right) \tag{5.12}$$

We can formally express the solution to Eq. 5.11 as

$$|\rho(t)\rangle\rangle = \hat{S}(t)|\rho(0)\rangle\rangle, \tag{5.13}$$

where $\hat{S}(t) = \exp(\hat{\mathcal{L}}\,t)$ is the quantum channel described by the original master equa-

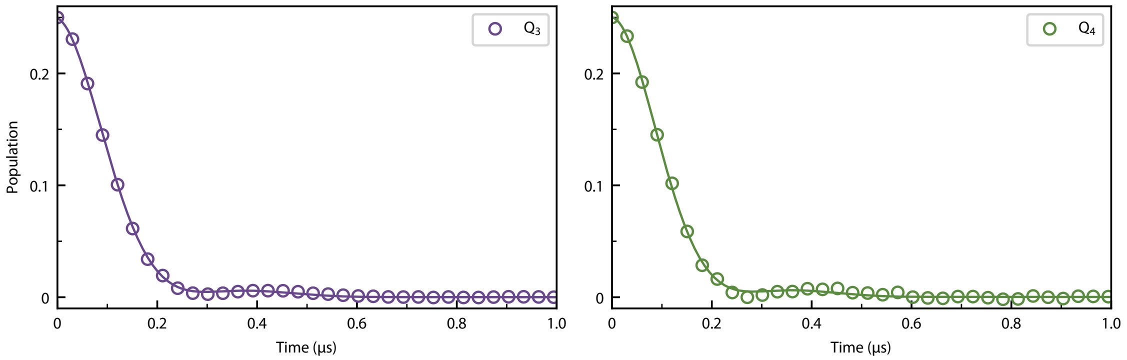

Figure 5-5: **Excited state population of data qubits during photon emission.** We utilize dispersive readout to measure the population of the data qubits during the photon release protocol immediately after the initialization of the data qubits into the state $|\psi^{\pm}_{\mathrm{qb}}\rangle = |gg\rangle/\sqrt{2} + (|eg\rangle + e^{\pm i\frac{\pi}{2}}|ge\rangle)/2$. The theoretical fit of the population is presented as a solid line in both plots.

tion in superoperator form. In this simplified model, the subspace formed by $\mathrm{Q}_1$ and $\mathrm{Q}_3$ is not coupled to the subspace formed by $\mathrm{Q}_2$ and $\mathrm{Q}_4$, which allows us to write the Liouvillian superoperator as $\hat{\mathcal{L}} = \hat{\mathcal{L}}_{13} + \hat{\mathcal{L}}_{24}$, where $\hat{\mathcal{L}}_{13(24)}$ is the Liouvillian superoperator of each two-qubit subsystem. Because $\hat{\mathcal{L}}_{13}$ and $\hat{\mathcal{L}}_{24}$ commute, we can factorize the quantum channel as

$$\hat{S}(t) = \exp(\hat{\mathcal{L}}_{13}\, t) \cdot \exp(\hat{\mathcal{L}}_{24}\, t). \tag{5.14}$$

We solve for the density matrix of the four-qubit system $\hat{\rho}$, which we use to compute system observables, i.e. $\langle \hat{O} \rangle = \mathrm{Tr}[\hat{\rho}\hat{O}]$.

To obtain the temporal wavepacket of the photon field amplitude, we use the input-output relations from Eq. 5.3:

$$\begin{aligned} \langle \hat{a}_{\mathrm{L}} \rangle &= \sqrt{\frac{\gamma}{2}} \left( \langle \hat{\sigma}_1^- \rangle + i \langle \hat{\sigma}_2^- \rangle \right), \\ \langle \hat{a}_{\mathrm{R}} \rangle &= \sqrt{\frac{\gamma}{2}} \left( \langle \hat{\sigma}_1^- \rangle - i \langle \hat{\sigma}_2^- \rangle \right). \end{aligned} \tag{5.15}$$

Here, we assume that there is no input into the waveguide $\langle \hat{a}^{\mathrm{in}}_{\mathrm{L/R}} \rangle = 0$. Using the solution to the master equation, we compute the wavepacket shape, given the initial state of the emitter qubits:

$$\begin{aligned}
|\psi^-_{\mathrm{qb}}\rangle &= \frac{|gg\rangle + |\psi^-\rangle}{\sqrt{2}} &\rightarrow\quad \langle\hat{a}_{\mathrm{L}}\rangle &= -\frac{g_{\mathrm{eff}}\sqrt{\gamma}}{\Gamma}e^{-\frac{\gamma}{4}t}\sinh\left(\frac{\Gamma}{2}t\right), &\langle\hat{a}_{\mathrm{R}}\rangle &= 0,\\
|\psi^+_{\mathrm{qb}}\rangle &= \frac{|gg\rangle + |\psi^+\rangle}{\sqrt{2}} &\rightarrow\quad \langle\hat{a}_{\mathrm{R}}\rangle &= \frac{g_{\mathrm{eff}}\sqrt{\gamma}}{\Gamma}e^{-\frac{\gamma}{4}t}\sinh\left(\frac{\Gamma}{2}t\right), &\langle\hat{a}_{\mathrm{L}}\rangle &= 0,
\end{aligned} \tag{5.16}$$

where we define $\Gamma = 2\sqrt{\left(\frac{\gamma}{4}\right)^2 - g_{\mathrm{eff}}^2}$. We use these expressions to fit the photon field amplitudes in Fig. 5-4b/c and extract the effective coupling between each emitter/data qubit pair $g_{\mathrm{eff}}/2\pi \approx 1.28$ MHz.

Next, we examine the data qubit population as a function of time during the photon release. Using the calculated system density matrix $\hat{\rho}$, we obtain the analytical expression for the excited state population of each data qubit as a function of time:

$$\rho^{(d)}_{33}(t) = \rho^{(d)}_{44}(t) = \frac{e^{-\frac{\gamma}{2}t}}{16\Gamma^2}\left[(\gamma^2 - 8g_{\mathrm{eff}}^2)\cosh(\Gamma t) + 2\gamma\Gamma\sinh(\Gamma t) - 8g_{\mathrm{eff}}^2\right], \tag{5.17}$$

We use Eq. 5.17 to fit the dispersive readout measurement of the data qubits during the photon release protocol, shown in Fig. 5-5. The decay in population here corresponds to to transfer into the emitter qubits and subsequent release into the waveguide.

### 5.4.2 Parametric Exchange Interactions

The exchange interactions used to execute the directional emission protocol are mediated by the parametric modulation of the tunable coupler frequencies. To see this, consider two qubits at frequencies $\omega_i$ and $\omega_j$, and a tunable coupler at frequency $\omega_c$, as illustrated in Fig. 5-6a. Each qubit is capacitively coupled to the tunable coupler at rates $g_{ic}$ and $g_{jc}$, and to each other at rate $g_{ij}$. The coupler is far-detuned from both qubit frequencies $\omega_c - \omega_{i/j} \gg g_{ic}, g_{jc}, g_{ij}$, and the qubits are slightly detuned by $\Delta = \omega_j - \omega_i$. The Hamiltonian of the system in the rotating frame of the qubit Q$_i$ is [67]

$$\hat{H} = \Delta\hat{\sigma}^+_j\hat{\sigma}^-_j + \left(\frac{g_{ic}g_{jc}}{\delta} + g_{ij}\right)(\hat{\sigma}^+_i\hat{\sigma}^-_j + \hat{\sigma}^-_i\hat{\sigma}^+_j), \tag{5.18}$$

where $\delta = 2\left(\frac{1}{\omega_i - \omega_c} + \frac{1}{\omega_j - \omega_c}\right)^{-1} = 2\left(\frac{1}{\delta_i} + \frac{1}{\delta_j}\right)^{-1}$. The coupling rates $g_{ic}, g_{jc}$, and $g_{ij}$ are determined by the the qubit frequencies and the capacitances $C_{ij}$, $C_c$, $C_i/C_j$, and $C_{j,c}/C_{i,c}$ as defined in Fig. 5-6a:

$$\begin{aligned} g_{ij} &\approx \frac{1}{2}\left(\frac{C_{ij}}{\sqrt{C_i C_j}} + \frac{C_{i,c}C_{j,c}}{\sqrt{C_i C_j C_c^2}}\right)\sqrt{\omega_i \omega_j} = \frac{\tilde{C}_{ij}}{2}\sqrt{\omega_i \omega_j}, \\ g_{nc} &\approx \frac{C_{n,c}}{2\sqrt{C_n C_c}}\sqrt{\omega_n \omega_c} = \frac{\tilde{C}}{2}\sqrt{\omega_n \omega_c} \qquad\qquad n = i, j. \end{aligned} \tag{5.19}$$

Here, we assume that $\mathrm{Q}_i$ and $\mathrm{Q}_j$ are identical qubits, with equal self-capacitances $C_i = C_j$ and capacitances to the coupler $C_{i,c} = C_{j,c}$. Substituting these expressions for the coupling rates into the Hamiltonian gives

$$\hat{H} = \Delta \hat{\sigma}_j^+ \hat{\sigma}_j^- + \sqrt{\omega_i \omega_j}\left(\frac{\tilde{C}^2 \omega_c}{4\delta} + \frac{\tilde{C}_{ij}}{2}\right)(\hat{\sigma}_i^+ \hat{\sigma}_j^- + \hat{\sigma}_i^- \hat{\sigma}_j^+). \tag{5.20}$$

Next, we modulate the frequency of the tunable coupler $\omega_c = \omega_{c0} + A\cos\Delta t$. In practice, this is realized by modulating the flux applied into the SQUID loop of the coupler. Since $\omega_c \gg \omega_i, \omega_j$, we can approximate the total detuning as $\delta \approx \delta_i = \omega_i - \omega_c$. Assuming the amplitude of the coupler frequency modulation $A \ll \delta_i$, we separate the qubit coupling into a static component and a time-varying component,

$$\hat{H} = \Delta \hat{\sigma}_j^+ \hat{\sigma}_j^- + \sqrt{\omega_i \omega_j}\left(\frac{\tilde{C}^2 \omega_{c0}}{4\delta} + \frac{\tilde{C}_{ij}}{2} + \frac{\tilde{C}^2 A\cos\Delta t}{4\delta}\right)(\hat{\sigma}_i^+ \hat{\sigma}_j^- + \hat{\sigma}_i^- \hat{\sigma}_j^+). \tag{5.21}$$

Finally, we rotate into the frame of the qubit detuning $\Delta$ and neglect the fast rotating terms. This approximation holds as long as the effective coupling rate $g_{\text{eff}} \ll \Delta$. The final time-independent Hamiltonian is given by

$$\hat{H} = \frac{A\tilde{C}^2\sqrt{\omega_i \omega_j}}{8\delta}(\hat{\sigma}_i^+ \hat{\sigma}_j^- + \hat{\sigma}_i^- \hat{\sigma}_j^+). \tag{5.22}$$

This Hamiltonian shows that the two detuned qubits $\mathrm{Q}_i$ and $\mathrm{Q}_j$ are effectively coupled at rate $g_{\text{eff}} = A\tilde{C}^2\sqrt{\omega_i \omega_j}/8\delta$. We show in Fig. 5-6c measurements of the chevron pattern for population exchange between qubits $\mathrm{Q}_3$ and $\mathrm{Q}_4$ mediated by a parametric

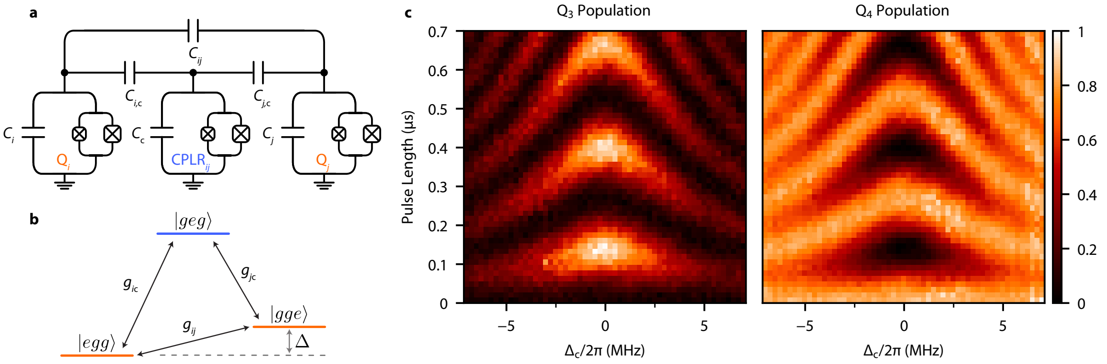

Figure 5-6: **Parametric interactions with a tunable coupler. a)** The circuit diagram of a system with a tunable coupler CPLR$_{ij}$ capacitively coupled two tunable transmon qubits Q$_i$ and Q$_j$. The coupling capacitance between the qubits is $C_{ij}$ and the coupling capacitances between each qubit and the coupler is $C_{i,c}$ ($C_{j,c}$). **b)** The single-excitation manifold level diagram of the system. The coupler frequency $\omega_c$ is far-detuned from the frequencies of the qubits $\omega_i$ and $\omega_j$, and the two qubits are slightly detuned from each other by $\Delta = \omega_j - \omega_i$. The capacitance between the qubits $C_{ij}$ mediates a direct coupling with strength $g_{ij}$. The capacitances between the coupler and each qubit give rise to couplings between each qubit-coupler pair at the rates $g_{ic}$ and $g_{jc}$. **c)** The measured population exchange between qubits Q$_3$ and Q$_4$ as a function of the parametric modulation pulse length and frequency offset $\Delta_c = \delta_c - \Delta$, where $\delta_c$ is the frequency of the modulation.

exchange interaction. Note that we can also vary we vary the effective coupling rate as a function of time by varying the frequency modulation amplitde $A(t)$. This feature can be used to shape the wavepacket of the emitted photon, which will be necessary in future work for perfect absorption of the emitted photons [20, 47, 60, 73].

## 5.5 Heterodyne Detection Scheme

Until this point, we have spoken vaguely about measuring photons in the form of time-dependent voltage signals. To study quantum properties of the emission, we must measure higher order signal correlations, as first demonstrated in [53, 74]. While single-photon detectors are common in optical experiments in the form of avalanche photodetectors, the smaller energy of microwave photons makes them difficult to measure. Microwave photon detectors in superconducting systems are an active area

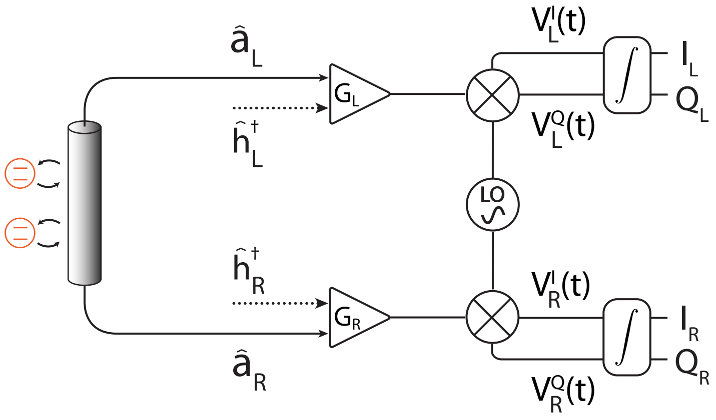

Figure 5-7: **Linear, phase-insensitive amplification and heterodyne detection scheme used to measure photon field amplitudes.** The emitter qubits shown in orange are coupled to a waveguide. Each end of the waveguide is connected to series of linear, phase-insensitive amplifiers, which we simplify as one amplifier with gain $G_{\text{L/R}}$. The phase-insensitive amplifier introduces noise ($\hat{h}_{\text{L/R}}$) to the output field amplitudes ($\hat{a}_{\text{L/R}}$). The amplified noisy voltage signals at the qubit frequency $f = \omega/2\pi$ are routed to an IQ mixer, where they are down-converted with a local oscillator at frequency $f_{\text{LO}}$ to an intermediate frequency $f_{\text{IF}} = f \pm f_{\text{LO}}$. These signals are low-pass filtered such that only signals at the difference frequency are digitized, further demodulated to baseband, and integrated over time to output a complex number at each end of the waveguide $S_{\text{L/R}} = I_{\text{L/R}} + iQ_{\text{L/R}}$.

of research [75, 76]. The detection scheme we use in this experiment is composed of a chain of linear amplifiers and analog-to-digital converters (ADCs), as illustrated in Fig. 5-7.

For single emitters, the waveguide behaves as a beamsplitter for radiation, and the set-up we use is the microwave analog of the Hanbury Brown and Twiss experiment [56]. The directional emission protocol allows us effectively to tune the transmission and reflection coefficients of the beamsplitter *in situ* for single-photons. At each end of the waveguide, we represent a series of linear, phase-insensitive amplifiers with a single amplifier of gain $G_{\text{L/R}}$. Because our amplification chain is phase-insensitive, noise represented by the field amplitude $\hat{h}_{\text{L/R}}$ is introduced to the output field amplitudes $\hat{a}_{\text{L/R}}$ at the amplifier. Phase-insensitive amplifiers act equally on both quadratures of a signal $\hat{a}_{\text{L/R}} = \hat{a}^{(1)}_{\text{L/R}} + i\hat{a}^{(2)}_{\text{L/R}}$, where we define the signal quadratures $\hat{a}^{(1)}_{\text{L/R}} = \text{Re}[\hat{a}_{\text{L/R}}]$ and $\hat{a}_{\text{L/R}}(2) = \text{Im}[\hat{a}_{\text{L/R}}]$.

Ideally, we want to measure both quadratures of $\hat{a}_{\mathrm{L/R}}$ simultaneously to characterize the output fields efficiently. However, the quadratures do not commute and cannot be measured simultaneously. Because the phase-insensitive amplifer adds additional noise to the system, which is always *at least* in the vacuum state, we can measure the amplified signals

$$\hat{S}_{\mathrm{L/R}} = \sqrt{G_{\mathrm{L/R}}}\hat{a}_{\mathrm{L/R}} + \sqrt{G_{\mathrm{L/R}} - 1}\hat{h}^{\dagger}_{\mathrm{L/R}} \tag{5.23}$$

simultaneously while preserving Heisenberg's uncertainty principle. To clarify, for the large gain $G >> 1$ in our measurement chain, we can rewrite this equation for the normalized signals as

$$\hat{S}'_{\mathrm{L/R}} = \frac{\hat{S}_{\mathrm{L/R}}}{\sqrt{G_{\mathrm{L/R}}}} \approx \hat{a}_{\mathrm{L/R}} + \hat{h}^{\dagger}_{\mathrm{L/R}}. \tag{5.24}$$

In the large gain limit, we see that the quadratures of $\hat{S}'_{\mathrm{L/R}}$ commute and can therefore be measured simultaneously. Once we amplify the field phase-insensitively, at least the vacuum noise is added to the measurement regardless of whether we measure one or both quadratures simultaneously [77]. Thus, it is natural to detect both quadratures with the heterodyne detection scheme shown in Fig. 5-7 [77, 78].

The IQ mixer splits both the input signal $V_{\mathrm{L/R}}(t)$ at frequency $f$ and a local oscillator at frequency $f_{\mathrm{LO}}$ equally into two branches, namely the in-phase ($I$) branch and the quadrature ($Q$) branch. In the $I$-branch, the input signal is multiplied by the local oscillator, while in the $Q$-branch, the phase of the local oscillator is shifted by $\pi/2$ before multiplication with the input signal. Multiplication of these signals results in ouptput signals at intermediate frequencies $f_{\mathrm{IF}} = f \pm f_{\mathrm{LO}}$, which are sent through a low-pass filter such that only the difference frequency arrives at the analog-to-digital converters (ADCs). See [34] for more details about the IQ-demodulation scheme. The signal in each branch is digitized, demodulated once again to baseband with digital signal processing techniques, and then integrated over time with custom FPGA code. The output of this measurement is a complex number

$$S_{\mathrm{L/R}} = I_{\mathrm{L/R}} + iQ_{\mathrm{L/R}} = \int_0^{t_0} dt (V^I_{\mathrm{L/R}}(t) + iV^Q_{\mathrm{L/R}}(t)) \tag{5.25}$$

at each end of the waveguide for each photon measurement, where $t_0$ is the integration time of our measurement. The temporal envelopes in Fig. 5-4b/c are the amplified voltage signals of the emitted directional photons before time-integration.

## 5.6 Photon State Tomography

The signal we measure at the ADCs is noisy, and we seek to extract the signal field amplitude $\hat{a}_{\mathrm{L/R}}$. Our goal is to use these signals to measure higher-order correlations to fully characterize the state of the emitted photon. Following the prescription described by [53, 63, 74, 77], we repeat the directional emission protocol to construct a 4D probability distribution $D(S_{\mathrm{L}}, S_{\mathrm{L}}^*, S_{\mathrm{R}}, S_{\mathrm{R}}^*, )$ we can use to obtain the moments of $S_{\mathrm{L}}$ and $S_{\mathrm{R}}$,

$$\langle \hat{S}_{\mathrm{L}}^{\dagger w} \hat{S}_{\mathrm{L}}^{x} \hat{S}_{\mathrm{R}}^{\dagger y} \hat{S}_{\mathrm{R}}^{z} \rangle = \int d^2 S_{\mathrm{L}} d^2 S_{\mathrm{R}} S_{\mathrm{L}}^{*w} S_{\mathrm{L}}^{x} S_{\mathrm{R}}^{*y} S_{\mathrm{R}}^{z} D(S_{\mathrm{L}}, S_{\mathrm{L}}^*, S_{\mathrm{R}}, S_{\mathrm{R}}^*), \tag{5.26}$$

where $w, x, y, z \in \{0, 1, 2, ...\}$. The measured signals $S_{\mathrm{L/R}}$ are composed of both the field of interest at each end of the waveguide $\hat{a}_{\mathrm{L/R}}$ as well as noise added by the amplification chain as described by the input-output relation for the amplified signal for large gain (Eq. 5.23). Employing the Binomial theorem, and assuming the signal and noise fields are uncorrelated, we can write the moments of the normalized signals as

$$\begin{gathered}\langle \hat{S}_{\mathrm{L}}^{\prime\dagger n} \hat{S}_{\mathrm{L}}^{\prime m} \hat{S}_{\mathrm{R}}^{\prime\dagger k} \hat{S}_{\mathrm{R}}^{\prime l} \rangle = \sum_{w=0}^{n} \sum_{x=0}^{m} \sum_{y=0}^{k} \sum_{z=0}^{l} \binom{n}{w} \binom{m}{x} \binom{k}{y} \binom{l}{z} \\ \langle \hat{a}_{\mathrm{L}}^{\dagger w} \hat{a}_{\mathrm{L}}^{x} \hat{a}_{\mathrm{R}}^{\dagger y} \hat{a}_{\mathrm{R}}^{z} \rangle \langle \hat{h}_{\mathrm{L}}^{\dagger n-w} \hat{h}_{\mathrm{L}}^{m-x} \hat{h}_{\mathrm{R}}^{\dagger k-y} \hat{h}_{\mathrm{R}}^{l-z} \rangle.\end{gathered} \tag{5.27}$$

We rewrite Eq. 5.26 in terms of the normalized signals

$$\langle \hat{S}_{\mathrm{L}}^{\prime\dagger w} \hat{S}_{\mathrm{L}}^{\prime x} \hat{S}_{\mathrm{R}}^{\prime\dagger y} \hat{S}_{\mathrm{R}}^{\prime z} \rangle = \int d^2 S_{\mathrm{L}} d^2 S_{\mathrm{R}} S_{\mathrm{L}}^{*w} S_{\mathrm{L}}^{x} S_{\mathrm{R}}^{*y} S_{\mathrm{R}}^{z} D(S_{\mathrm{L}}, S_{\mathrm{L}}^*, S_{\mathrm{R}}, S_{\mathrm{R}}^*) G_{\mathrm{L}}^{-\frac{n+m}{2}} G_{\mathrm{R}}^{-\frac{k+l}{2}}. \tag{5.28}$$

In realistic measurements, the noise field is in the thermal state,

$$\hat{\rho}_h = \sum_i \frac{n_{\text{noise}}^i}{(1+n_{\text{noise}})^{i+1}} |i\rangle\langle i|, \tag{5.29}$$

where the average number of photons in the noise field $n_{\text{noise}}$ is related by the noise temperature $T_{\text{noise}}$ by the Bose-Einstein distribution $n_{\text{noise}} = 1/(e^{\hbar\omega/k_\text{B}T_{\text{noise}}} - 1)$. To measure the moments of the noise signals $\langle \hat{h}_\text{L}^{\dagger n} \hat{h}_\text{L}^m \hat{h}_\text{R}^{\dagger k} \hat{h}_\text{R}^l \rangle$, we can repeatedly measure $S_\text{L}$ and $S_\text{R}$ while leaving the emitter qubits in their ground states such the emitted photon field is in the state $|\psi_{\text{ph}}\rangle = |n_\text{L} n_\text{R}\rangle = |00\rangle$. The assumption that the signal field is in the vacuum state is valid for low system temperatures $T$ such that $k_\text{B}T \ll \hbar\omega$, and as a result the moments of the vacuum signal fields are

$$\langle \hat{a}_\text{L}^{\dagger w} \hat{a}_\text{L}^x \hat{a}_\text{R}^{\dagger y} \hat{a}_\text{R}^z \rangle_{|00\rangle} = \begin{cases} 1 & \text{if } w, x, y, z = 0 \\ 0 & \text{otherwise} \end{cases}. \tag{5.30}$$

This helps us simplify Eq. 5.27 to obtain the moments of the noise field directly from measurements of the normalized signal fields

$$\langle \hat{h}_\text{L}^{\prime \dagger n} \hat{h}_\text{L}^{\prime m} \hat{h}_\text{R}^{\prime \dagger k} \hat{h}_\text{R}^{\prime l} \rangle = \langle \hat{S}_\text{L}^{\prime \dagger n} \hat{S}_\text{L}^{\prime m} \hat{S}_\text{R}^{\prime \dagger k} \hat{S}_\text{R}^{\prime l} \rangle_{|00\rangle}. \tag{5.31}$$

We interleave these noise measurements with measurements of the desired (non-vacuum) signals to account for system drifts.

Before collecting statistics of the fields emitted by the directional emission protocol, we must characterize the effective gain of the measurement chain from the emitter qubits to each end of the waveguide. In our experiment, we calibrate the gain in three ways, which yield similar results in practice:

1. We repeatedly measure $S_{\text{L/R}}$ after preparing a single emitter qubit in the superposition state $|\psi_{\text{qb}}\rangle = (|g\rangle + |e\rangle)/\sqrt{2}$. Because the photon is released into both propagation directions with equal probability, the emitted photon state will be $|\psi_{\text{ph}}\rangle = |n_\text{L} n_\text{R}\rangle = |00\rangle/\sqrt{2} + (|01\rangle + |10\rangle)/2$. After measuring the moments of the noise fields with Eq. 5.31, we calculate the signal first and second order

moments directly with the obtained probability distribution $D(S_{\mathrm{L}}, S_{\mathrm{L}}^{*}, S_{\mathrm{R}}, S_{\mathrm{R}}^{*},)$. The first and second order moments for the field amplitude have the relation $\langle \hat{a}_{\mathrm{L/R}} \rangle_{|\psi_{\mathrm{ph}}\rangle} = \sqrt{2} \langle \hat{a}_{\mathrm{L/R}}^{\dagger} \hat{a}_{\mathrm{L/R}} \rangle_{|\psi_{\mathrm{ph}}\rangle}$. By inverting the normalized signal amplification input-output relation in Eq. 5.24, we back out the effective gain of each measurement chain. Though the measurement is the simplest, it is the least precise because of error in the measurement of the signal moments.

2. We measure the absolute power delivered to an emitter qubit by the VNA through both ends of the waveguides, using the method discussed in Fig. 3-6. We send a resonant tone at this power with the VNA, and then we measure the power of the signal that arrives at the ADCs in Fig. 5-7. The ratio of these signals is the gain $G = P_{\mathrm{out}}/P_{\mathrm{in}}$.

3. We send a high power coherent tone resonant with one of the emitter qubits through one end of the waveguide and measure the power spectral density at the other end. We also calibrate the absolute power delivered to the emitter with the VNA and measure the power at the ADCs as a function of demodulation frequency. We observe the Mollow Triplet, a signature of strong coupling of the emitter and the probe field [51], which we fit to theory and master equation simulation to calibrate the effective gain of each measurement chain [61, 73].

Now we have all the information we need to proceed with the measurement of repeated directional photon emission experiments. After measuring both $\langle \hat{h}_{\mathrm{L}}^{\prime\dagger n} \hat{h}_{\mathrm{L}}^{\prime m} \hat{h}_{\mathrm{R}}^{\prime\dagger k} \hat{h}_{\mathrm{R}}^{\prime l} \rangle$ and $\langle \hat{S}_{\mathrm{L}}^{\prime\dagger n} \hat{S}_{\mathrm{L}}^{\prime m} \hat{S}_{\mathrm{R}}^{\prime\dagger k} \hat{S}_{\mathrm{R}}^{\prime l} \rangle$ separately, we can solve for $\langle \hat{a}_{\mathrm{L}}^{\prime\dagger w} \hat{a}_{\mathrm{L}}^{\prime x} \hat{a}_{\mathrm{R}}^{\prime\dagger y} \hat{a}_{\mathrm{R}}^{\prime z} \rangle$ by inverting a system of linear equations. We define the vectors $\vec{S}$ and $\vec{a}$, where each element is a different moment defined by $\langle \hat{S}_{\mathrm{L}}^{\prime\dagger n} \hat{S}_{\mathrm{L}}^{\prime m} \hat{S}_{\mathrm{R}}^{\prime\dagger k} \hat{S}_{\mathrm{R}}^{\prime l} \rangle$ and $\langle \hat{a}_{\mathrm{L}}^{\prime\dagger w} \hat{a}_{\mathrm{L}}^{\prime x} \hat{a}_{\mathrm{R}}^{\prime\dagger y} \hat{a}_{\mathrm{R}}^{\prime z} \rangle$ respectively for all combinations of $n, m, k, l \leq N$ and $w, x, y, z \leq N$, where $N = 2$ is the highest order of the moments under consideration. The vectors each have length $(N+1)^4$ and are related by the noise field matrix $H$, such that $\vec{S} = H\vec{a}$. By inverting $H$, we can solve for the moments of the field amplitude $\hat{a}_{\mathrm{L/R}}$ with $\vec{a} = H^{-1}\vec{S}$. Note that for a certain ordering of moments in the vectors $\vec{S}$ and $\vec{a}$, the matrix $H$ is lower triangular and the system can be solved efficiently with back substitution [63].

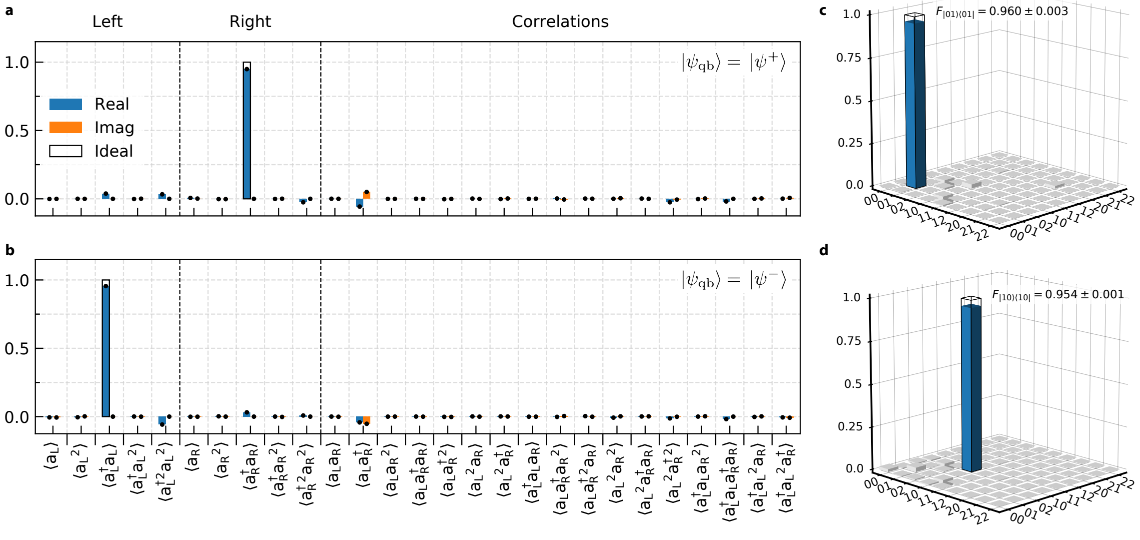

Figure 5-8: **Photon state tomography.** **a)** The moments and correlations of the left and right propagating channels of the waveguide up to 4th order with $|\psi_{\rm qb}\rangle = |\psi^+\rangle$. All moments are nearly zero, except $\langle \hat{a}_{\rm R}^\dagger \hat{a}_{\rm R}\rangle \approx 0.95$. This data is averaged over $5 \times 10^8$ repetitions **b)** The same as (a) but with $|\psi_{\rm qb}\rangle = |\psi^-\rangle$. All moments are once again nearly zero, except $\langle \hat{a}_{\rm L}^\dagger \hat{a}_{\rm L}\rangle \approx 0.95$. **c)** The real part of the density matrix of the photon emitted to the right based on the moments shown in (a) with a state fidelity of $F_{|01\rangle\langle 01|} = 0.96 \pm 0.003$. The Hilbert space of the emitted photon is truncated to $N \leq 2$ photons. **d)** The real part of the density matrix of the photon emitted to the left based on the moments shown in (b) with a state fidelity of $F_{|10\rangle\langle 10|} = 0.954 \pm 0.001$.

The moments of and correlations between $\hat{a}_{\rm L}$ and $\hat{a}_{\rm R}$ for the photons we generate with the directional emission protocol are shown in Fig. 5-8a and 5-8b up to fourth order. When $\rm Q_3$ and $\rm Q_4$ are initialized to $|\psi^+\rangle$, we obtain $\langle \hat{a}_{\rm R}^\dagger \hat{a}_{\rm R}\rangle \approx 1$ as the only appreciably non-zero moment, as expected for a single photon which only propagates towards the right. Similarly, we measure $\langle \hat{a}_{\rm L}^\dagger \hat{a}_{\rm L}\rangle \approx 1$ as the only non-zero moment for the leftward-propagating photon emitted when the qubits are initialized to $|\psi^-\rangle$. All third and fourth order moments are nearly zero (maximum magnitude of 0.05), demonstrating the single-photon nature of the emission process.

Finally, we use these moments and their respective standard deviations $\nu_{n,m}$ to obtain the density matrices of the emitted photons, shown in Figs. 5-8c/d, using maximum likelihood estimation. Here, we truncate the Hilbert space to $N \leq 2$ photons. Assuming each calculated moment is normally-distributed with standard deviation

$\nu_{n,m}$, the conditional probability of measuring the expected moment $\langle \hat{a}^{\dagger n}_{\mathrm{L/R}} \hat{a}^{m}_{\mathrm{L/R}} \rangle$ given a density matrix $\hat{\rho}_{\mathrm{L/R}}$ for leftward/rightward emission respects a normal distribution via the central limit theorem

$$p(\langle \hat{a}^{\dagger n}_{\mathrm{L/R}} \hat{a}^{m}_{\mathrm{L/R}} \rangle | \hat{\rho}_{\mathrm{L/R}}) \propto e^{-|\langle \hat{a}^{\dagger n}_{\mathrm{L/R}} \hat{a}^{m}_{\mathrm{L/R}} \rangle - \mathrm{Tr}[\hat{\rho}_{\mathrm{L/R}} \hat{a}^{\dagger n}_{\mathrm{L/R}} \hat{a}^{m}_{\mathrm{L/R}}]| / \nu^2_{n,m}} \tag{5.32}$$

We maximize the log-likelihood function with respect to the elements of the density matrix $\hat{\rho}_{\mathrm{L/R}}$ [77, 79],

$$\mathcal{L}_{\mathrm{Log}} = -\sum_{n,m} \frac{1}{\nu^2_{n,m}} |\langle \hat{a}^{\dagger n}_{\mathrm{L/R}} \hat{a}^{m}_{\mathrm{L/R}} \rangle - \mathrm{Tr}[\hat{\rho}_{\mathrm{L/R}} \hat{a}^{\dagger n}_{\mathrm{L/R}} \hat{a}^{m}_{\mathrm{L/R}}]|^2 \tag{5.33}$$

We use the properties that $\hat{\rho}_{\mathrm{L/R}} \geq 0$ and $\mathrm{Tr}[\hat{\rho}_{\mathrm{L/R}}] = 1$ as constraints in the maximization of Eq. 5.33 to obtain the density matrix $\hat{\rho}_{\mathrm{L/R}}$ that best represents measured set of moments. From these density matrices, we obtain a state fidelity of $F = 0.960 \pm 0.003$ and $F = 0.954 \pm 0.001$ for the rightward- and leftward-propagating photons, respectively. We observe a small, non-zero number of photons in the right (left) output of the waveguide when the qubits are initialized to $|\psi^+\rangle$ ($|\psi^-\rangle$). This infidelity is the result of imperfect interference between the emission pathways caused by qubit decoherence during emission and small deviations from necessary conditions $\Delta x = \lambda/4$ and $J_\Sigma = 0$.

## 5.7 Conclusions

Our results demonstrate that quantum interference between emitters in a waveguide QED architecture can be used to realize a directional single photon source. While we have only performed photon generation in this work, the time-reverse of the emission protocol can be used to capture photons with this same architecture if the wavepacket of the incoming photon is symmetric in time [20–22, 47]. Note that the wavepacket of the generated photon can be shaped arbitrarily, in principle, by varying the time-dependence of the coupling between the data and emitter qubits [20–22, 47, 60, 73, 80, 81]. Looking forward, we envision building a quantum network by tiling devices with the presented architecture in series and applying our protocol for both photon generation and capture. Such a network will enable entanglement distribution and information shuttling with high fidelity in support of extensible quantum information processing.

# Chapter 6

# Directional Absorption

To date, we have used a superconducting wQED architecture to implement directional emission of itinerant photons on demand. This module is a potential building block of distributed, modular quantum computation within a network comprised of distant, non-local nodes [82, 83]. The next step to perform simple quantum communication is to absorb the photon and receive the transmitted quantum information. The directional emission module can be operated as an absorber module for itinerant photons.

## 6.1 A Quantum Interconnect

Two modules tiled along the same waveguide as shown in Fig. 6-1 comprise the simplest quantum interconnect in this architecture. The most basic communication protocol in this architecture requires only two modules: the emitter module sends a single photon along the waveguide towards the absorber module, which captures the photon.

We note that the devices presented in Fig. 6-1 are modified versions of the original device used for directional emission shown in Fig. 5-1a. We increase the emitter-waveguide coupling rate to $\gamma/2\pi = 17.2$ MHz, which is the upper bound on the rate of decay of the photon from the module into the waveguide. By increasing $\gamma$, we lessen the impact of dephasing due to environmental flux noise on the directional

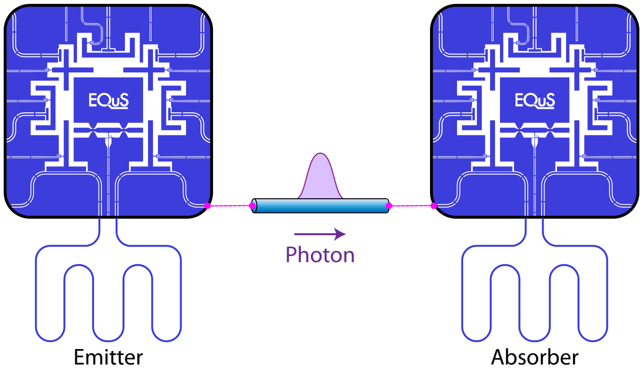

Figure 6-1: **The simplest bidirectional quantum interconnect with superconducting wQED.** Two identical modules interface with the same bidirectional waveguide: the emitter module (left) sends a photon to the right towards the absorber module (right). This is the simplest form of quantum communication in this architecture.

emission protocol. We also increase the asymmetry of the Josephson junctions in the dc-SQUIDs of the data and emitter qubits to decrease the frequency range of the qubits to reduce sensitivity to flux noise away from the peak frequency, as discussed in Chapter 2.4. We also increase the range of tunable coupling strength between qubit pairs by decreasing the distance between qubit pairs. These modifications grant more flexibility in shaping the wavepacket of emitted photon, which is critical to the efficiency of the absorption protocol.

## 6.2 Photon Shaping

As discussed throughout Chapter 5, we use the data qubits to prepare the desired entangled state $|\psi_{\mathrm{qb}}\rangle$ for directional photon emission. We can faithfully prepare this state because the data qubits are not directly coupled to the waveguide and do not experience the associated loss. We use parametric exchange interactions (see Sec. 5.4.2) to transfer the state $|\psi_{\mathrm{qb}}\rangle$ to the emitter qubits. The effective data-emitter coupling strength $g_{\mathrm{eff}}$ is proportional to the amplitude of the pulse used to drive the couplers. Tuning the amplitude of the coupler pulse shapes the temporal envelope of the coupling $g_{\mathrm{eff}}(t)$ and thereby controls the rate at which the photon is released into the waveguide.

For the temporal envelope of the photon shown in Figs. 5-4b–c, we choose a constant $g_{\text{eff}}$. By changing $g_{\text{eff}}$, we vary the length of the temporal envelope of the photon. To simplify the photon absorption scheme, we impose the condition that the emitted photons must be time-symmetric [82]. This way, the time-reverse of the pulses that emit the photon on the emitter module can be used to absorb the photon with the absorber module.

In addition to a time-symmetric photon, we seek to create a photon that decays as quickly as possible in order to minimize the impact of dephasing and non-radiative decay. As seen in Sec. 3.4, the coherence $\langle \hat{\sigma}^- \rangle$ of an emitter qubit naturally decays exponentially at rate $\gamma/2$. Thus, the temporal envelope of the photon amplitude decays exponentially at rate $\gamma/2$. In our setup, we transfer population between data and emitter qubits at rate $g_{\text{eff}}$. The population then decays from the emitters into the waveguide at rate $\gamma$. The emitter-waveguide coupling rate $\gamma$ is the upper-bound on the total rate of decay of the photon into the waveguide. Therefore, a time-symmetric photon wavepacket $f(t)$ with features of exponential decay is optimal, and a natural candidate is

$$f(t) \propto \operatorname{sech}\left(\frac{\gamma t}{2}\right). \tag{6.1}$$

We derive the pulse shapes necessary to produce a photon wavepacket of this shape, following the discussion in [84]. We simplify the discussion by considering a single driven emitter qubit which decays into a single-ended waveguide. The results of this discussion can be expanded straightforwardly to our system. The state vector of the emitter qubit $|\psi(t)\rangle$ evolves according to the non-unitary Schrödinger equation:

$$\frac{d}{dt}|\psi(t)\rangle = \left(-i\hat{H}(t) - \frac{\gamma}{2}|e\rangle\langle e|\right)|\psi(t)\rangle. \tag{6.2}$$

The qubit state vector is not properly normalized and its norm decays over time according to

$$\frac{d}{dt}\langle\psi(t)|\psi(t)\rangle = -\gamma|\langle e|\psi(t)\rangle|^2, \tag{6.3}$$

which depends on the overlap between the qubit state vector and the excited state.

The square norm of the qubit state vector $\langle\psi(t)|\psi(t)\rangle$ can be interpreted as the probability that a photon has not been emitted at time $t$. The probability of emitting a photon in the interval $(t, t+dt)$ is therefore $\gamma|\langle e|\psi(t)\rangle|^2 dt$. This allows us to write a combined state vector for the qubit-photon system,

$$|\Psi(t)\rangle = |\psi(t)\rangle|0\rangle + |g\rangle \int_{-\infty}^{t} d\tau \sqrt{\gamma}\langle e|\psi(t)\rangle \hat{a}^\dagger(\tau)|0\rangle \tag{6.4}$$

where $\hat{a}^\dagger(\tau)$ is the creation operator for a photon emitted into the waveguide in the time interval $(\tau, \tau + d\tau)$. The continuous creation operator has the commutator $[\hat{a}(\tau'), \hat{a}^\dagger(\tau)] = \delta(\tau' - \tau)$. This implies that the single photon state $\sqrt{d\tau}\hat{a}^\dagger(\tau)|0\rangle$ is properly normalized. We define the photon amplitude wavepacket

$$f(t) = \sqrt{\gamma}\langle e|\psi(t)\rangle, \tag{6.5}$$

We impose the condition that the photon is always emitted in the infinite time limit $t \to \infty$, which we use to properly normalize the photon wavepacket,

$$\int_{-\infty}^{\infty} |f(\tau)|^2 d\tau = 1. \tag{6.6}$$

Using the ideal photon wavepacket shape in Eq. 6.1, we arrive at the expression for the normalized wavepacket,

$$f(t) = \frac{\sqrt{\gamma}}{2}\operatorname{sech}\left(\frac{\gamma t}{2}\right). \tag{6.7}$$

From conservation of probability, we know that

$$\int_{-\infty}^{t} |f(\tau)|^2 d\tau + \langle\psi(t)|\psi(t)\rangle = 1. \tag{6.8}$$

We seek to find the Hamiltonian that yields the desired photon shape. The Hamiltonian of the qubit subject to a time-dependent resonant drive of strength $g(t)$ is

$$\hat{H}(t) = ig(t)(\hat{\sigma}^- - \hat{\sigma}^+) \tag{6.9}$$

Before proceeding, we properly normalize the qubit state vector to impose unitary dynamics. The normalized state vector is $|\phi(t)\rangle = |\psi(t)\rangle/\sqrt{\langle\psi(t)|\psi(t)\rangle}$ which obeys the Schrödinger equation

$$\frac{d}{dt}|\phi(t)\rangle = \left(-i\hat{H}(t) - \frac{\gamma}{2}|e\rangle\langle e| + \frac{\gamma}{2}|\langle\phi(t)|e\rangle|^2\right)|\phi(t)\rangle \tag{6.10}$$

We derive the relationship between the photon wavepacket and the overlap of the normalized state with the excited state by combining Eq. 6.5 and Eq. 6.8:

$$\langle e|\phi(t)\rangle = \frac{f(t)}{\sqrt{\gamma(1-\int_{-\infty}^{t}|f(\tau)|^2 d\tau)}} = \frac{1}{\sqrt{1+e^{-\gamma t}}}. \tag{6.11}$$

We parameterize the normalized state vector against a time-dependent angle $\theta(t)$

$$|\phi(t)\rangle = \cos\frac{\theta(t)}{2}|g\rangle + \sin\frac{\theta(t)}{2}|e\rangle \tag{6.12}$$

We substitute this parameterized qubit state into Eq. 6.10 and arrive at two coupled differential equations. Combining the differential equations yields

$$\dot{\theta}(t) = 2g(t) - \frac{\gamma}{2}\sin\frac{\theta(t)}{2}. \tag{6.13}$$

We note that $\langle e|\phi(t)\rangle = \sin\frac{\theta(t)}{2}$ relates $\theta(t)$ to the desired photon wavepacket $f(t)$ via Eq. 6.11. This allows us to write

$$\theta(t) = 2\arcsin\left(\frac{1}{\sqrt{1+e^{-\gamma t}}}\right), \tag{6.14}$$

which we substitute into Eq. 6.13 to solve for the time-dependent drive strength that yields the desired time-symmetric photon shape in Eq. 6.7

$$g(t) = \frac{\gamma}{2}\text{sech}\left(\frac{\gamma t}{2}\right). \tag{6.15}$$

This model can be generalized to produce a photon with arbitrary linewidth $\gamma_{\text{ph}} \leq \gamma$

with shape

$$f(t) = \frac{\sqrt{\gamma_{\mathrm{ph}}}}{2}\mathrm{sech}\left(\frac{\gamma_{\mathrm{ph}} t}{2}\right). \tag{6.16}$$

The photon linewidth is limited by the decay rate of the emitter qubit population into the waveguide $\gamma_{\mathrm{ph}} \leq \gamma$. Larger photon linewidths translate to a faster overall photon emission process. To release a photon with the largest linewidth, and therefore the fastest possible symmetric emission, we chose $\gamma_{\mathrm{ph}} = \gamma$ in the above analysis. To produce a time-symmetric photon shape with linewidth $\gamma_{\mathrm{ph}} \leq \gamma$, we conduct a similar analysis, yielding the time-dependent drive strength,

$$g(t) = \frac{\gamma_{\mathrm{ph}}}{4\mathrm{cosh}\left(\frac{\gamma_{\mathrm{ph}} t}{2}\right)} \frac{(1 + e^{\gamma_{\mathrm{ph}} t})\gamma/\gamma_{\mathrm{ph}} + 1 - e^{\gamma_{\mathrm{ph}} t}}{\sqrt{(1 + e^{\gamma_{\mathrm{ph}} t})\gamma/\gamma_{\mathrm{ph}} - e^{\gamma_{\mathrm{ph}} t}}}. \tag{6.17}$$

This simplified single-emitter model can be extended naturally to capture a data qubit coupled to the emitter with time-dependent coupling strength $g(t)$. The same time-dependent coupling strength can be implemented with a parametric exchange interaction mediated by a tunable coupler between the data and emitter qubits detailed in Sec. 5.4.2. We modulate the data-emitter coupling strength at the frequency of the detuning $\Delta$ of the two qubits $g_{\mathrm{eff}}(t) = g(t)\cos\Delta t$, depicted for different photon bandwidths in Fig. 6-2a. Going one step further, we can extend the model to include two pairs of data and emitter qubits to integrate this photon shaping scheme with our directional emission protocol discussed in Chapter 5.

Following the tunable coupling model discussed in Sec. 5.4.2, the relationship between the frequency of the tunable coupler $\omega_{\mathrm{c}}$ and the coupling between the relevant pair of qubits $\mathrm{Q}_i$ and $\mathrm{Q}_j$ is [67,68]

$$g(\omega_{\mathrm{c}}) = \frac{g_{i\mathrm{c}} g_{j\mathrm{c}}}{2}\left(\frac{1}{\omega_i - \omega_{\mathrm{c}}} + \frac{1}{\omega_j - \omega_{\mathrm{c}}} - \frac{1}{\omega_i + \omega_{\mathrm{c}}} - \frac{1}{\omega_j + \omega_{\mathrm{c}}}\right) + g_{ij} \tag{6.18}$$

where $g_{i\mathrm{c}}$, $g_{j\mathrm{c}}$, and $g_{ij}$ are defined in Eq. 5.19. We numerically invert Eq. 6.18 to find $\omega_{\mathrm{c}}(g_{\mathrm{eff}}(t)) = \omega_{\mathrm{c}}(g(t)\cos\Delta t)$, the time-dependent tunable coupler frequency required to release a time-symmetric photon of bandwidth $\gamma_{\mathrm{ph}} \leq \gamma$ with parametric interactions, as shown in Fig. 6-2b.

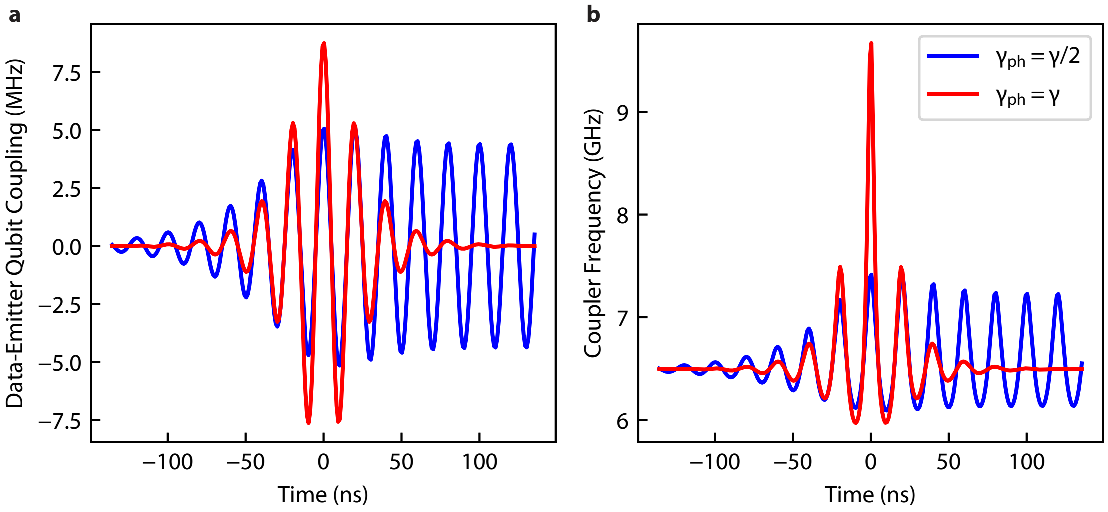

Figure 6-2: **Time-dependent data-emitter qubit coupling and tunable coupler frequency for time-symmetric photon emission with parametric interactions. a)** Data-emitter qubit coupling during symmetric photon emission, based on device parameters. The qubit frequencies are $\omega_i = 5.05$ GHz and $\omega_j = 5.1$ GHz. The coupling is modulated at the qubit detuning $\Delta = \omega_j - \omega_i = 50$ MHz. The bare qubit-qubit coupling based on device simulations is $g_{ij} = 18.9$ MHz, and the couplings of each qubit to the tunable coupler are $g_{ic} = 158.2$ MHz and $g_{jc} = 149.1$ MHz, referenced at the zero-coupling point coupler frequency 6.417 GHz. The emitter-waveguide coupling is $\gamma = 17.2$ MHz, and the time-dependent coupling is shown for the release of a photon with bandwidth $\gamma_{\text{ph}} = \gamma/2$ and $\gamma_{\text{ph}} = \gamma$. **b)** The time-dependent tunable coupler frequencies required to execute the data-emitter couplings shown in **a)** and release time-symmetric bandwidths $\gamma_{\text{ph}} = \gamma/2$ and $\gamma_{\text{ph}} = \gamma$ with parametric exhange interactions.

We plan to simplify the device design to use only one data qubit to prepare the emitters in the appropriate entangled state. This simplifies the photon emission protocol, as the initial $\sqrt{\text{iSWAP}}$ gate used to entangle the original two data qubits is no longer necessary. Instead, we can create the entangled state of choice $|\psi^{\pm}\rangle$ by first exciting the single data qubit with a $\pi$ pulse, and then using parametric exchange interactions to distribute the population evenly and simultaneously amongst the emitter qubits. The key is to ensure that the parametric exchanges interactions are $\mp 90$ degrees out of phase. This relative phase can be induced via the parametric modulation pulses. We scale the data-emitter qubit coupling $g(t)$ in the three-qubit design by a factor of $1/\sqrt{2}$ to emit a photon of the form in Eq. 6.7.

## 6.3 Symmetric Emission and Absorption Simulations

We model our emission and absorption module with four resonant qubits — two emitter qubits, denoted $\mathrm{Q}_1$ and $\mathrm{Q}_2$, each coupled with strength $g(t)$ to a different data qubit ($\mathrm{Q}_3$ and $\mathrm{Q}_4$, respectively) as shown in Fig. 6-3a. The emitter qubits are spaced by a distance $d = \lambda/4$ along a common waveguide, where $\lambda$ is the wavelength of the emission in the waveguide. We assume that the device is properly calibrated and the emitters are uncoupled as discussed in Fig. 5-2. We write the interaction Hamiltonian for this system, setting $\hbar$ to unity,

$$\hat{H} = g(t)\,(\hat{\sigma}_3^-\hat{\sigma}_1^+ + \hat{\sigma}_3^+\hat{\sigma}_1^-) + g(t)(\hat{\sigma}_4^-\hat{\sigma}_2^+ + \hat{\sigma}_4^+\hat{\sigma}_2^-) \tag{6.19}$$

where the raising and lowering operators of each qubit $\mathrm{Q}_i$ is denoted as $\hat{\sigma}_i^\pm$, where $i \in \{1, 2, 3, 4\}$ is the qubit number. We assume the only loss mechanism is the decay of the emitter qubits into the waveguide at rate $\gamma$. The master equation for this four-qubit system with density matrix $\hat{\rho}$ is

$$\frac{d\hat{\rho}}{dt} = -i\big[\hat{H}, \hat{\rho}\big] + \sum_j^2 \gamma D\big[\hat{\sigma}_j^-\big]\hat{\rho}. \tag{6.20}$$

where $D[\hat{O}] = \hat{O}\hat{\rho}\hat{O}^\dagger - \frac{1}{2}\{\hat{O}^\dagger\hat{O}, \hat{\rho}\}$ is the Lindblad dissipator. To emit time-symmetric photon with linewidth $\gamma$, we execute the time-dependent coupling discussed in Sec. 6.2,

$$g(t) = \frac{\gamma}{2}\mathrm{sech}\left(\frac{\gamma t}{2}\right). \tag{6.21}$$

We initialize the data qubits at time $t_0$ into the appropriate entangled state to emit a photon with the desired propagation direction, as discussed in Chapter 5 (+ for rightward emission, - for leftward emission),

$$|\psi(t = t_0)\rangle = |\mathrm{Q}_1\mathrm{Q}_2\mathrm{Q}_3\mathrm{Q}_4\rangle = |\psi^\pm\rangle = \frac{|ggeg\rangle \pm i|ggge\rangle}{\sqrt{2}}, \tag{6.22}$$

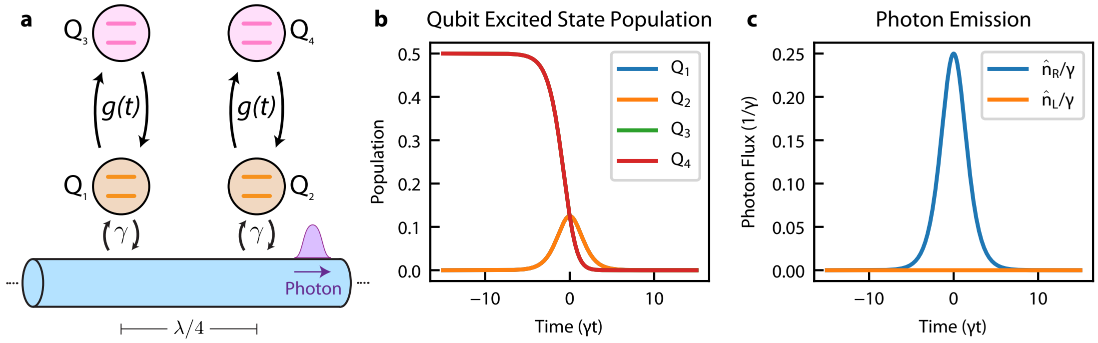

Figure 6-3: **Time-symmetric photon emission simulations. a)** Simplified model of device with two emitter qubits in orange and two data qubits in pink. The emitter qubits are spaced $d = \lambda/4$ along the waveguide in purple. The emitter-waveguide decay rate is $\gamma$. Each data-emitter qubit pair is coupled with time-dependent strength $g(t)$ shaped to produce a time-symmetric photon with the wavepacket shape in Eq. 6.7. **b)** Qubit population during the photon emission simulation. Note that the emitter qubits have equal population, as do the data qubits, throughout the emission process. The emitter qubits are only slightly populated before releasing the excitation into the waveguide. **c)** Photon flux in both propagation directions in the waveguide during emission. In this simulation, we initialized the data qubits into $|\psi+\rangle$ such that the shaped photon propagates in the rightward direction.

We numerically solve the master equation for $\hat{\rho}(t)$, which we use to solve for critical system observables over time such as qubit populations and coherences (i.e. $\langle\hat{O}(t)\rangle = \mathrm{Tr}[\hat{\rho}(t)\hat{O}(t)]$ ). For example, from the input-output relations in Eq. 5.3, we calculate the average photon flux through each end of the waveguide

$$\begin{aligned}\langle\hat{n}_{\mathrm{L}}(t)\rangle &= \frac{\gamma}{2}\left[\langle\sigma_1^+(t)\sigma_1^-(t)\rangle + \langle\sigma_2^+(t)\sigma_2^-(t)\rangle - i\langle\sigma_2^+(t)\sigma_1^-(t)\rangle + i\langle\sigma_1^+(t)\sigma_2^-(t)\rangle\right]\\ \langle\hat{n}_{\mathrm{R}}(t)\rangle &= \frac{\gamma}{2}\left[\langle\sigma_1^+(t)\sigma_1^-(t)\rangle + \langle\sigma_2^+(t)\sigma_2^-(t)\rangle + i\langle\sigma_2^+(t)\sigma_1^-(t)\rangle - i\langle\sigma_1^+(t)\sigma_2^-(t)\rangle\right]\end{aligned} \tag{6.23}$$

The time-dependent photon fluxes represent the photon wavepacket, shown in Fig. 6-3c. We also use the density matrix $\hat{\rho}(t)$ to calculate the qubit populations during the photon emission process, shown in Fig. 6-3b.

To simulate photon absorption, we extend the model to include an identical absorber device module, also composed of two emitter qubits $\mathrm{Q}_5$ and $\mathrm{Q}_6$ and two data qubits $\mathrm{Q}_7$ and $\mathrm{Q}_8$. The absorber module shares the same waveguide as the emitter module, as depicted in Fig. 6-1 and Fig. 6-4a. In this model, the modules are spaced an arbitrary distance $D = x_5 - x_1$, where $x_1$ and $x_5$ are the positions of the qubits along the waveguide. Our master equation approach operates under the Markov approximation discussed in Sec. 3.1 and 3.4, which assumes that the 1D continuum of modes in the waveguide has a much larger bandwidth than the emitter qubits. The qubits interact with the modes in the waveguide approximately instantaneously. For absorption simulations, a photon with the same bandwidth as the emitter qubits ($\gamma_{\text{ph}} = \gamma$) acts an input to the device module through the waveguide. Thus, for large arbitrary inter-module distances $D$, the Markov approximation breaks down and the master equation approach is no longer valid.

We proceed with our numerical master equation simulation by assuming that $D \ll 2\pi\nu/\gamma$, where $\nu$ is the speed of the emitted photon in the waveguide. This assumption allows us to ignore the large space-correlation of the photon and continue to use the master equation approach because the modules interact approximately instantaneously. Using our physical system parameters and a photon bandwidth of $\gamma/2\pi = 17.2$ MHz, we approximate the spatial extent of the photon as $2\pi\nu/\gamma \approx 7$ meters. In our experiment, the modules are about $D \approx 10$ cm apart along the waveguide, well within the spatial extent of the photon. However, it is important to note that the emission and absorption scheme works for any distance $D$, even though the master equation formalism can no longer be used to capture the system dynamics. The photon experiences more propagation loss for longer inter-module distances $D$, but there is no required short-range interaction that limits the absorption process.

We write the local interaction Hamiltonian of the emitter and absorber modules

$$\begin{aligned} \hat{H}_{\text{E}} &= g(t)\,(\hat{\sigma}_3^- \hat{\sigma}_1^+ + \hat{\sigma}_3^+ \hat{\sigma}_1^-) + g(t)(\hat{\sigma}_4^- \hat{\sigma}_2^+ + \hat{\sigma}_4^+ \hat{\sigma}_2^-) \\ \hat{H}_{\text{A}} &= g(-t)\,(\hat{\sigma}_7^- \hat{\sigma}_5^+ + \hat{\sigma}_7^+ \hat{\sigma}_5^-) + g(-t)(\hat{\sigma}_8^- \hat{\sigma}_6^+ + \hat{\sigma}_8^+ \hat{\sigma}_6^-). \end{aligned} \tag{6.24}$$

We execute the coupling strength $g(t)$ to produce a photon with bandwidth $\gamma_{\text{ph}} = \gamma$

$$g(t) = g(-t) = \frac{\gamma}{2}\text{sech}\left(\frac{\gamma t}{2}\right). \tag{6.25}$$

We emphasize that the coupling strength on the absorption module is the time reverse

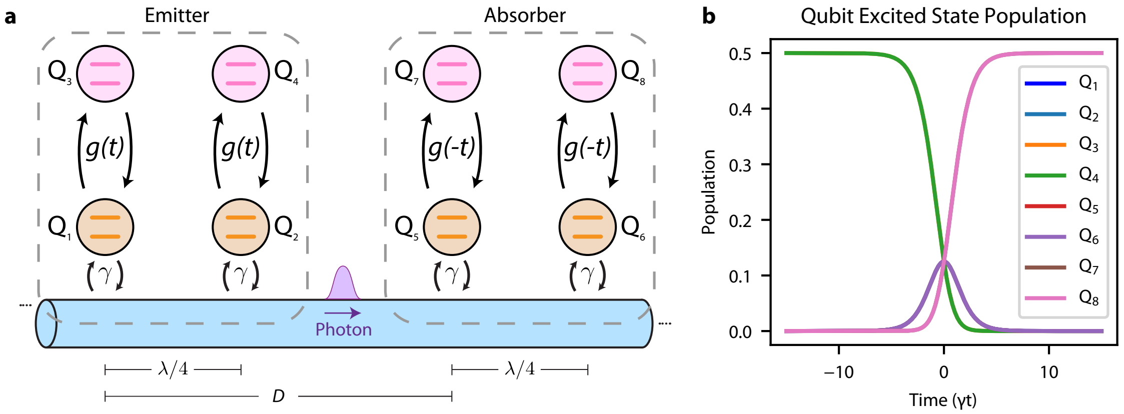

Figure 6-4: **Photon absorption simulation.** **a)** Model of the quantum interconnect, with the photon emission module on the left and absorption module on the right. The modules are each composed of two emitter qubits in orange $Q_{1/5}$ and $Q_{2/6}$ and two data qubits in pink $Q_{3/7}$ and $Q_{4/8}$. The emitter qubits of each module are each spaced $d = \lambda/4$ along a shared waveguide in purple, and the inter-module distance along the waveguide is $D$. The coupling between the data-emitter qubit pairs on the emitter module is $g(t) = \frac{\gamma}{2}\text{sech}\left(\frac{\gamma t}{2}\right)$, which releases a time-symmetric rightward propagating photon into the waveguide illustrated in Fig. 6-3c. In order to execute efficient absorption, the coupling between the data-emitter qubit pairs on the absorber module must be the time reverse $g(-t)$. **b)** Simulated qubit population throughout the rightward-propagating photon emission and absorption process. Note that data qubits on each module have identical population in this ideal simulation, and all emitter qubits have identical population dynamics throughout emission and absorption.

$g(-t)$. To produce a photon with the maximum bandwidth $\gamma_{\text{ph}} = \gamma$, $g(t)$ is already a time-symmetric function, but for smaller photon bandwidths $\gamma_{\text{ph}} < \gamma$ this is not the case, as the coupling strength takes the form in Eq. 6.17.

Next we write the waveguide-mediated interaction Hamiltonian the emitter qubit pairs on different modules, noting that in practice and in this model we cancel the waveguide-mediated interaction betweeen the emitter qubits on the same module,

$$\begin{aligned}\hat{H}_{\text{J}} = \frac{\gamma}{2}\sin\left(kD\right)[\hat{\sigma}_5^-\hat{\sigma}_1^+ + \hat{\sigma}_5^+\hat{\sigma}_1^- + \hat{\sigma}_6^-\hat{\sigma}_2^+ + \hat{\sigma}_6^+\hat{\sigma}_2^-] \\ + \frac{\gamma}{2}\sin\left(kD + \frac{\pi}{2}\right)[\hat{\sigma}_6^-\hat{\sigma}_1^+ + \hat{\sigma}_6^+\hat{\sigma}_1^-] \\ + \frac{\gamma}{2}\sin\left(kD - \frac{\pi}{2}\right)[\hat{\sigma}_5^-\hat{\sigma}_2^+ + \hat{\sigma}_5^+\hat{\sigma}_2^-].\end{aligned} \tag{6.26}$$

where $k = 2\pi/\lambda$ is the wave number of the emitted photon. Each emitter qubit is coupled to the waveguide at rate $\gamma$. The decay of each emitter qubit is also correlated with the decay of both emitter qubits on the other module. The master equation the governs the dynamics of the interconnect is

$$\frac{d\hat{\rho}}{dt} = -i\big[\hat{H} + \hat{H}_{\mathrm{J}}, \hat{\rho}\big] + \sum_{i,j=1,2,5,6} \gamma \cos(\phi_{i,j}) D\big[\hat{\sigma}_i^-, \hat{\sigma}_j^-\big]\hat{\rho} \tag{6.27}$$

where $D[\hat{A}, \hat{B}]\hat{\rho} = \hat{B}\hat{\rho}\hat{A}^\dagger - \frac{1}{2}\{\hat{B}^\dagger\hat{A}, \hat{\rho}\}$ is the Lindblad superoperator. The phase $\phi_{i,j} = k(x_j - x_i)$ represents the relative position phase between the emitter qubits. This master equation captures all time dynamics throughout photon emission, propagation in the waveguide, and absorption. We initialize the data qubits on the emitter module into the entangled state to emit a photon in the rightward direction towards the absorber module

$$|\psi(t = t_0)\rangle = |\psi^+\rangle = |\mathrm{Q}_3\mathrm{Q}_4\rangle = \frac{|eg\rangle + i|ge\rangle}{\sqrt{2}}. \tag{6.28}$$

We numerically solve the master equation to find the eight-qubit density matrix $\hat{\rho}(t)$, which we use to extract the individual qubit populations shown in Fig. 6-4b. At the end of this simulation, the data qubits $\mathrm{Q}_7$ and $\mathrm{Q}_8$ on the absorber module are in the state $|\psi^+\rangle$, indicating perfect state transfer.

This model can be modified to study the effects of many systemic imperfections, including and not limited to:

1. Qubit dephasing due to environmental flux noise
2. Deviations from an inter-qubit distance from $d = \lambda/4$
3. Imperfect cancellation of emitter qubit coupling
4. Slight qubit detunings
5. Non-radiative decay
6. Thermal photons in the waveguide

7. Unequal emitter-waveguide decay rates $\gamma$
8. Initial entangled state preparation error
9. Photon shaping imprecision
10. Hybridization of qubits with tunable couplers

In practice and in simulation, we find that dephasing disrupts the critical interference process in the waveguide during emission, which limits the emission and absorption efficiency. More details about systemic imperfects and their effects on directionality and absorption efficiency can be found in [47].

## 6.4 Remote Entanglement

Once photon absorption is successfully executed, the next step towards a viable quantum network is the demonstration of remote entanglement, the key to distributed quantum computing. Remote entanglement is a resource for gate teleportation [85,86]. The ability to teleport multi-qubit gates across different modules enables communication and computation schemes in large-scale quantum networks.

The quantum interconnect discussed throughout this chapter can facilitate the remote entanglement of the data qubits on the emitter module and their counterpart on the absorber module. The remote entanglement protocol builds on the photon absorption protocol. Instead of emitting and absorbing a photon, we can design data-emitter qubit couplings $\tilde{g}(t)$ such that the emitter module releases an excitation into the waveguide exactly half the time. In other words, instead of fully emitting the photon, we entangle the data qubits on the emitter module with the propagating photon in the waveguide.

We approach the problem of deriving the data-qubit emitter coupling as $\tilde{g}(t)$ similar to the derivation in Sec. 6.2 for the emission of a symmetric photon. When emitting a photon, we assume that the probability of emitting a photon is one as $t \to \infty$. The desired emitted photon probability amplitude or wavepacket $f(t)$ is normalized such that $\int_{-\infty}^{\infty} |f(t)|^2 dt = 1$. We seek to emit a photon of the same symmetric shape $\tilde{f}(t) \propto \text{sech}(\gamma t/2)$ with probability $\int_{-\infty}^{\infty} |\tilde{f}(t)|^2 dt = 1/2$. Therefore, with the proper normalization, the desired "half-photon" wavepacket is

$$\tilde{f}(t) = \frac{\sqrt{\gamma}}{2\sqrt{2}} \text{sech}\left(\frac{\gamma t}{2}\right) \tag{6.29}$$

We follow the same analysis in Sec. 6.2 to derive the corresponding data-emitter qubit coupling rate

$$\tilde{g}(t) = \frac{\gamma \text{sech}\left(\frac{\gamma t}{2}\right)\left(\tanh\left(\frac{\gamma t}{2}\right) - 1\right)}{2\sqrt{\tanh^2\left(\frac{\gamma t}{2}\right) - 2\tanh\left(\frac{\gamma t}{2}\right) + 5}}. \tag{6.30}$$

To emit a photon with linewidth $\gamma_{\text{ph}} < \gamma$ with probability $1/2$, a similar analysis yields the appropriate data-emitter qubit coupling rate

$$\tilde{g}(t) = \frac{\sqrt{\gamma_{\text{ph}}}\ \text{sech}\left(\frac{\gamma_{\text{ph}} t}{2}\right)\left[\gamma - \gamma_{\text{ph}} \tanh\left(\frac{\gamma_{\text{ph}} t}{2}\right)\right]}{2\sqrt{\gamma_{\text{ph}} \tanh^2\left(\frac{\gamma_{\text{ph}} t}{2}\right) - 2\gamma \tanh\left(\frac{\gamma_{\text{ph}} t}{2}\right) + 6\gamma - \gamma_{\text{ph}}}} \tag{6.31}$$

Notably, the necessary absorption data-emitter coupling rate is not the time reverse of $\tilde{g}(t)$ when a "half-photon" is emitted. Instead, for an emitted "half-photon" with bandwidth $\gamma_{\text{ph}} = \gamma$, the absorption data-emitter coupling rate is $g(-t)$ from Eq. 6.21 – the same coupling rate necessary for the full photon absorption process. For this remote entanglement protocol, the emitter module releases the photon with probability 1/2. The other half of the time, the excitation remains in the data qubits of the emitter module and the absorber module never receives the photon. When the photon is emitted, the absorber should always prepare to capture the photon in full. If the absorption data-emitter coupling rate is $\tilde{g}(-t)$, only a "quarter-photon" arrives at the data qubits on the absorber module. Therefore, the proper data-emitter coupling rate to absorb this "half-photon" is $g(-t)$ from Eq. 6.21, as was the case for full photon absorption.

We use the model outlined in Sec. 6.3 for absorption to numerically simulate the remote entanglement protocol shown in Fig. 6-5a. On the absorption model, the data-emitter qubit coupling used for the emitter module is $\tilde{g}(t)$ in Eq. 6.30, and $g(-t)$ in

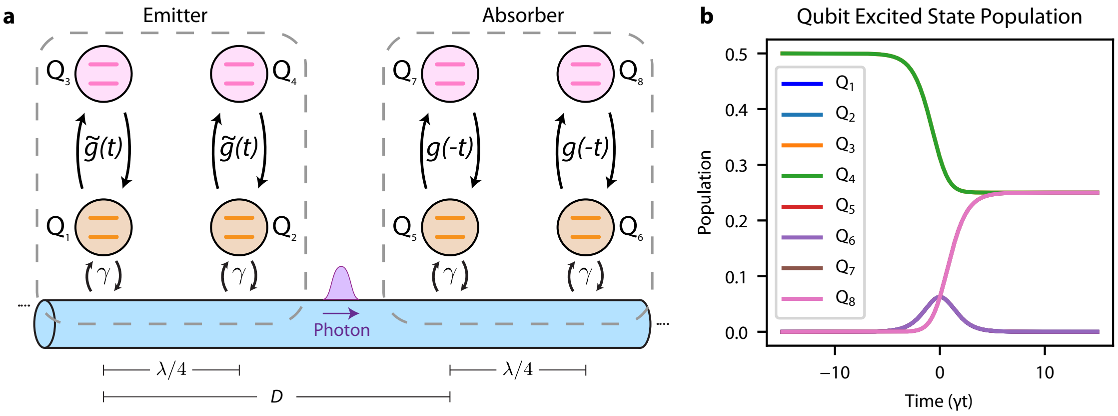

Figure 6-5: **Remote entanglement simulation.** **a)** Model of the quantum interconnect, with the photon emission module on the left and absorption module on the right. The modules are each composed of two emitter qubits in orange $Q_{1/5}$ and $Q_{2/6}$ and two data qubits in pink $Q_{3/7}$ and $Q_{4/8}$. The emitter qubits of each module are each spaced $d = \lambda/4$ along a shared waveguide in purple, and the inter-module distance along the waveguide is $D$. The coupling between the data-emitter qubit pairs on the emitter module is shown in Eq. 6.30, which releases a time-symmetric rightward propagating photon into the waveguide with probability $1/2$. The coupling between the data-emitter qubit pairs on the absorber module must be the time reverse $g(-t)$ in Eq. 6.21 to fully absorb the entangled photon. **b)** Simulated qubit population throughout the remote entanglement process. Note that data qubits on each module have identical population in this ideal simulation, and all emitter qubits have identical population dynamics. All data qubits are equally populated at the end of the protocol - a signature of the final four-qubit entangled state.

Eq. 6.21 for the absorber module. This adjustment is made in the system Hamiltonian. We use the master equation shown in Eq. 6.27 to calculate the population of each qubit in the emitter and absorber modules shown in Fig 6-5b.

Once the entangled photon is absorbed by the emitter module, the data qubits on both modules are in the four-qubit entangled state

$$|\psi\rangle = |\mathrm{Q}_3\mathrm{Q}_4\mathrm{Q}_7\mathrm{Q}_8\rangle = \frac{1}{2}\left[|eggg\rangle + i|gegg\rangle + e^{-ikD}\left(|ggeg\rangle + i|ggge\rangle\right)\right] \tag{6.32}$$

where $k$ is the wavenumber of the emitted photon and $D$ is the distance between the modules. The relative phase $e^{-ikD}$ results from rightward photon propagation across a distance $D$ in the waveguide between the emitter and absorber modules. Local single-and two-qubit gates can be used to switch between different combinations of remote two-qubit entangled states – a prerequisite for gate teleportation schemes [85,86].

We extend this approach to remotely entangle $2N$ data qubits on $N$ identical modules connected to a common waveguide. This network architecture and remote entanglement protocol can be used to generate W states with $2N$ non-local qubits:

$$|\psi_{\mathrm{qb}}\rangle = \frac{1}{\sqrt{2N}}\left(|egg...g\rangle + |geg...g\rangle + |gge...g\rangle + ... + |ggg...e\rangle\right). \tag{6.33}$$

We have the freedom to design data-emitter qubit coupling rates such as $\tilde{g}(t)$ in Eq. 6.30 to release a photon with $(N-1)/N$ probability from the first module in this array. Then, we also design absorption data-emitter qubit coupling rates for each sequential module in the array such that they each absorb the propagating photon with probability $1/N$. Once the $2N$-qubit state is prepared, local operations on each qubit can be used to prepare the non-local W state [87] for photon loss resilient communication schemes. Error mitigation strategies compatible with this network architecture include heralding, entanglement purification [88], teleportation with GHZ states [89], and quantum communication with W states [87].

# Chapter 7

# Conclusions: A Quantum Network

Superconducting circuits are a promising platform for the exploration of microwave quantum optics, in addition to the development of large-scale, extensible quantum computation. Superconducting systems are custom-designed and compatible with modern microelectronic fabrication techniques. However, in contrast to optical and atomic quantum systems that utilize optical photons or mobile atoms as information carriers for quantum communication, shuttling information across long distances remains an outstanding challenge in superconducting systems. The distribution of entanglement over distant, non-local modules enables robust quantum computation schemes.

In the last decade, waveguide Quantum Electrodynamics (wQED), a formalism that describes the interaction of atoms with a continuum of propagating photonic modes, has been explored within superconducting systems with artificial atoms. The original motivation for this exploration was rooted in the pursuit of novel, fundamental physics and quantum optics. More recently, the development of wQED within superconducting systems has motivated practical applications in quantum networks and communication.

In this thesis, we create a communication module for superconducting systems based on wQED. This module comprises four qubits and four tunable couplers that interface with a bidirectional waveguide. We engineer a quantum interference effect that results in the emission of an itinerant microwave photon in the direction of

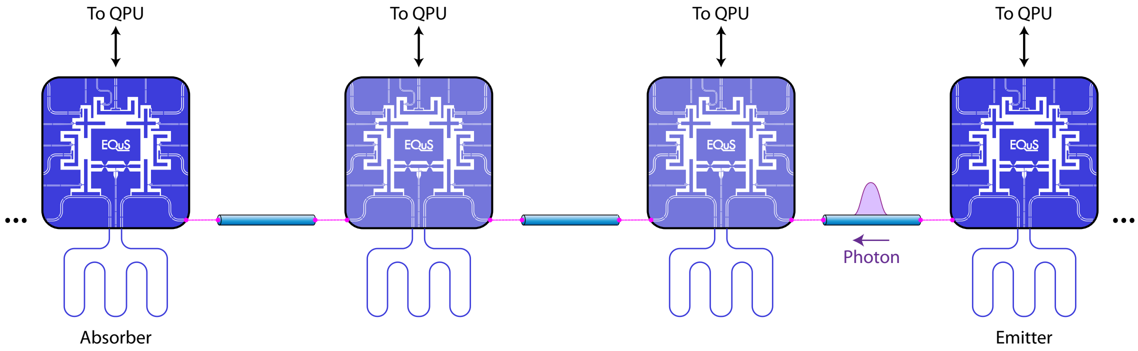

Figure 7-1: **An extensible, all-to-all quantum network.** An array of modules tiled along the same waveguide. The emitter module on the right emits a rightward propagating photon towards the absorber module on the left. The modules in between the absorber and emitter are placed in a transparency mode, such that they do not interact with the propagating photon.

propagation of choice in the waveguide. The time-reverse of this directional photon emission protocol can be used to absorb the photon with a different module on the waveguide. An emitter and absorber module together form a quantum interconnect capable of facilitating remote entanglement and gate teleportation.

By tiling many modules along a common waveguide as shown in Fig. 7-1, we can create an extensible quantum network with all-to-all connectivity. Any two modules can communicate with each other in the network via itinerant microwave photons. In addition to its utility for quantum communication applications, this set of cascaded modules can generate and manipulate stabilizer codes for quantum error correction [46]. This quantum network architecture enables high-fidelity entanglement distribution and information shuttling in support of extensible quantum information processing.

# Appendix A

# Experimental Setup

Throughout experiment detailed in Chapter 5, we use one device with two transmon emitter qubits ($Q_{1/2}$) [40] and two transmon data qubits ($Q_{3/4}$) arranged in a two by two lattice. There is a tunable coupler [67, 68] between the emitter qubits ($C_{12}$), between the data qubits ($C_{34}$), and between adjacent data/emitter qubit pairs ($C_{13}$ and $C_{24}$). All qubits and couplers (except $C_{12}$) are coupled to a $\lambda/4$ resonator with a resonance frequency between 8.0-8.4 GHz for dispersive readout. The key device parameters are summarized in Table A.1.

| Parameter | $Q_1$ | $Q_2$ | $Q_3$ | $Q_4$ |
|---|---|---|---|---|
| Frequency | 4.93 GHz | 4.93 GHz | 4.8 GHz | 4.85 GHz |
| Anharmonicity | -274 MHz | -273 MHz | -307 MHz | -307 MHz |
| $\gamma/2\pi$ | 3.2 MHz | 3.2 MHz | - | - |
| $\gamma_\phi/2\pi$ | 8 kHz | 41 kHz | - | - |
| $T_1$ | - | - | 13.8 $\mu$s | 13.4$\mu$s |
| $T_2^*$ | - | - | 18.1 $\mu$s | 23.6 $\mu$s |

Table A.1: **Summary of directional emission device parameters.** The operational qubit frequencies, anharmonicities, emitter-waveguide coupling strengths $\gamma$, emitter dephasing rates $\gamma_\phi$, and $T_1$ and $T_2^*$ of the data qubits are given for the emitter ($Q_{1/2}$) and data qubits ($Q_{3/4}$) on the device used throughout the experiment.

This experiment was conducted in a Bluefors XLD600 dilution refrigerator, which can reach a base temperature of 10 mK. The device is protected from ambient magnetic fields by superconducting and Cryoperm-10 shields below the mixing chamber (MXC). Each end of the waveguide that hosts the emitted photons is connected to

| Component | Manufacturer | Model |
|---|---|---|
| Dilution Fridge | Bluefors | XLD1000 |
| RF Source | Rohde & Schwarz | SGS100 |
| DC Source | QDevil | QDAC |
| Control Chassis | Keysight | M9019A |
| AWG | Keysight | M3202A |
| ADC | Keysight | M3102A |
| Frequency Standard | SRS | FS725 |

Table A.2: **Summary of control equipment.** The manufacturers and model numbers of the control equipment used for the experiment.

a microwave circulator for dual input-output operation. To minimize thermal noise from higher temperature stages, the inputs are attenuated by 20 dB at the 4 K stage, 10 dB at the Still, and 60 dB (40 dB for resonator readout input) at the MXC. The output signals are each filtered with a 3 GHz high-pass and 12 GHz low-pass filters. Two additional isolators are placed after the circulator in the MXC to prevent noise from higher-temperature stages traveling back into the device. A detailed schematic of the experimental setup is shown in Fig. A-1.

All eight qubit and coupler frequencies are tuned with both static flux biasing (DC) and fast flux control (RF). The DC and RF inputs are joined by a RF choke below the MXC before passing through a 300 MHz low pass filter. The RF flux control lines are attenuated by 20 dB at the 4K stage, and by 10 dB at the Still. The data qubits are equipped with local charge lines for independent single-qubit XY gates.

Outside of the dilution refrigerator, we use control electronics to generate signals for device operation, as specified in Table A.2. The pulse envelopes of the signals used for XY and Z control, readout input, and waveguide input are programmed in the Labber software and then uploaded to Arbitrary Waveform Generators (AWG) that are controlled by the Keysight PXIe Chassis. For XY control, waveguide, and readout inputs, these envelopes are then mixed with high-frequency local oscillator tones generated by RF sources. All microwave electronics are frequency-locked at 10 MHz by a common rubidium frequency standard. We place 1 kΩ resistors at the output of each DC voltage source to generate the current used to flux bias qubit frequencies.

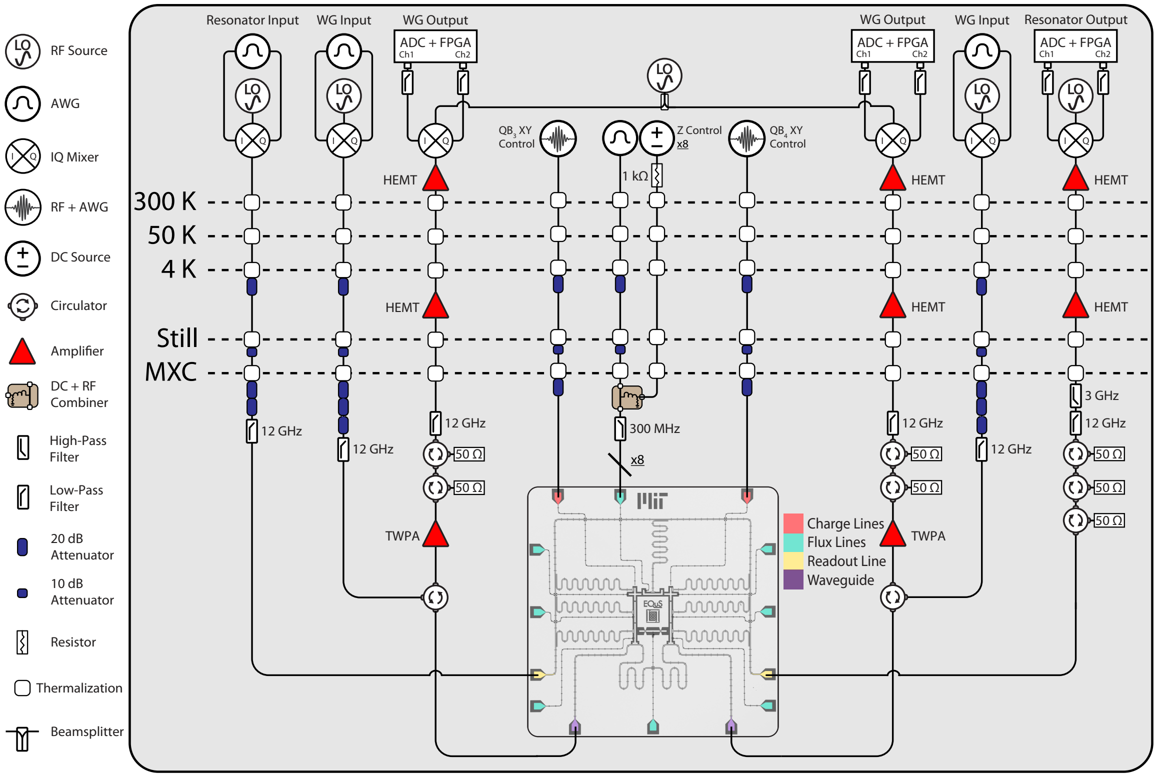

Figure A-1: **Setup for directional emission experiment.** Wiring schematic of the device and all electronics used to perform the experiment. Note that only one flux line configuration is shown (green), but each qubit and coupler is coupled to a flux line with separate, but identical, control electronics.

To provide further signal amplification on the output lines, we use a Traveling Wave Parametric Amplifier (TWPA) [90] at the MXC, a High Electron Mobility Transistor (HEMT) amplifiers at the 4K stage and MITEQ HEMT amplifiers at the room temperature stage. We then use an IQ mixer to down-convert the amplified signal to an intermediate frequency. The Analog to Digital Converter (ADC), which is also controlled by the same PXIe chassis, associated with the signal line digitizes and filters this signal. Finally, we use custom FPGA code to demodulate the signal for analysis.

# Bibliography

[1] J. F. Kurose and K. W. Ross, *Computer Networking: A Top-Down Approach.* Boston, MA: Pearson, 7 ed., 2016.

[2] J. Catsoulis, *Designing embedded hardware.* O'Reilly, 2005.

[3] J. L. Hennessy and D. A. Patterson, *Computer Architecture: A Quantitative Approach.* Amsterdam: Morgan Kaufmann, 5 ed., 2012.

[4] C. Monroe, R. Raussendorf, A. Ruthven, K. R. Brown, P. Maunz, L.-M. Duan, and J. Kim, "Large-scale modular quantum-computer architecture with atomic memory and photonic interconnects," *Phys. Rev. A*, vol. 89, p. 022317, Feb 2014.

[5] I. Söllner, S. Mahmoodian, S. L. Hansen, L. Midolo, A. Javadi, G. Kiršanskė, T. Pregnolato, H. El-Ella, E. H. Lee, J. D. Song, S. Stobbe, and P. Lodahl, "Deterministic photon–emitter coupling in chiral photonic circuits," *Nature Nanotechnology*, vol. 10, pp. 775–778, Sept. 2015.

[6] R. J. Coles, D. M. Price, J. E. Dixon, B. Royall, E. Clarke, P. Kok, M. S. Skolnick, A. M. Fox, and M. N. Makhonin, "Chirality of nanophotonic waveguide with embedded quantum emitter for unidirectional spin transfer," *Nature Communications*, vol. 7, p. 11183, Mar. 2016.

[7] J. Petersen, J. Volz, and A. Rauschenbeutel, "Chiral nanophotonic waveguide interface based on spin-orbit interaction of light," *Science*, vol. 346, pp. 67–71, Oct. 2014.

[8] R. Mitsch, C. Sayrin, B. Albrecht, P. Schneeweiss, and A. Rauschenbeutel, "Quantum state-controlled directional spontaneous emission of photons into a nanophotonic waveguide," *Nature Communications*, vol. 5, p. 5713, Dec. 2014.

[9] P. Lodahl, S. Mahmoodian, S. Stobbe, A. Rauschenbeutel, P. Schneeweiss, J. Volz, H. Pichler, and P. Zoller, "Chiral quantum optics," *Nature*, vol. 541, pp. 473–480, Jan. 2017.

[10] P. Solano, J. A. Grover, J. E. Hoffman, S. Ravets, F. K. Fatemi, L. A. Orozco, and S. L. Rolston, "Chapter Seven - Optical Nanofibers: A New Platform for Quantum Optics," in *Advances In Atomic, Molecular, and Optical Physics*, vol. 66, pp. 439–505, Academic Press, Jan. 2017.

[11] Y. Wan, D. Kienzler, S. D. Erickson, K. H. Mayer, T. R. Tan, J. J. Wu, H. M. Vasconcelos, S. Glancy, E. Knill, D. J. Wineland, A. C. Wilson, and D. Leibfried, "Quantum gate teleportation between separated qubits in a trapped-ion processor," *Science*, vol. 364, no. 6443, pp. 875–878, 2019.

[12] J. M. Pino, J. M. Dreiling, C. Figgatt, J. P. Gaebler, S. A. Moses, M. S. Allman, C. H. Baldwin, M. Foss-Feig, D. Hayes, K. Mayer, C. Ryan-Anderson, and B. Neyenhuis, "Demonstration of the trapped-ion quantum ccd computer architecture," *Nature*, vol. 592, pp. 209–213, Apr 2021.

[13] D. Bluvstein, H. Levine, G. Semeghini, T. T. Wang, S. Ebadi, M. Kalinowski, A. Keesling, N. Maskara, H. Pichler, M. Greiner, V. Vuletic, and M. D. Lukin, "A quantum processor based on coherent transport of entangled atom arrays," 2021.

[14] Y. P. Zhong, H.-S. Chang, K. J. Satzinger, M.-H. Chou, A. Bienfait, C. R. Conner, É. Dumur, J. Grebel, G. A. Peairs, R. G. Povey, D. I. Schuster, and A. N. Cleland, "Violating bell's inequality with remotely connected superconducting qubits," *Nature Physics*, vol. 15, pp. 741–744, Aug 2019.

[15] N. Leung, Y. Lu, S. Chakram, R. K. Naik, N. Earnest, R. Ma, K. Jacobs, A. N. Cleland, and D. I. Schuster, "Deterministic bidirectional communication and remote entanglement generation between superconducting qubits," *npj Quantum Information*, vol. 5, no. 1, p. 18, 2019.

[16] H.-S. Chang, Y. P. Zhong, A. Bienfait, M.-H. Chou, C. R. Conner, E. Dumur, J. Grebel, G. A. Peairs, R. G. Povey, K. J. Satzinger, and A. N. Cleland, "Remote entanglement via adiabatic passage using a tunably dissipative quantum communication system," *Phys. Rev. Lett.*, vol. 124, p. 240502, Jun 2020.

[17] Y. Zhong, H.-S. Chang, A. Bienfait, É. Dumur, M.-H. Chou, C. R. Conner, J. Grebel, R. G. Povey, H. Yan, D. I. Schuster, and A. N. Cleland, "Deterministic multi-qubit entanglement in a quantum network," *Nature*, vol. 590, pp. 571–575, Feb 2021.

[18] L. D. Burkhart, J. D. Teoh, Y. Zhang, C. J. Axline, L. Frunzio, M. Devoret, L. Jiang, S. Girvin, and R. Schoelkopf, "Error-detected state transfer and entanglement in a superconducting quantum network," *PRX Quantum*, vol. 2, p. 030321, Aug 2021.

[19] J. Ramette, J. Sinclair, Z. Vendeiro, A. Rudelis, M. Cetina, and V. Vuletić, "Any-to-any connected cavity-mediated architecture for quantum computing with trapped ions or rydberg arrays," 2021.

[20] P. Kurpiers, P. Magnard, T. Walter, B. Royer, M. Pechal, J. Heinsoo, Y. Salathé, A. Akin, S. Storz, J.-C. Besse, S. Gasparinetti, A. Blais, and A. Wallraff, "Deterministic quantum state transfer and remote entanglement using microwave photons," *Nature*, vol. 558, no. 7709, pp. 264–267, 2018.

[21] C. J. Axline, L. D. Burkhart, W. Pfaff, M. Zhang, K. Chou, P. Campagne-Ibarcq, P. Reinhold, L. Frunzio, S. M. Girvin, L. Jiang, M. H. Devoret, and R. J. Schoelkopf, “On-demand quantum state transfer and entanglement between remote microwave cavity memories,” *Nature Physics*, vol. 14, pp. 705–710, July 2018.

[22] P. Campagne-Ibarcq, E. Zalys-Geller, A. Narla, S. Shankar, P. Reinhold, L. Burkhart, C. Axline, W. Pfaff, L. Frunzio, R. J. Schoelkopf, and M. H. Devoret, “Deterministic remote entanglement of superconducting circuits through microwave two-photon transitions,” *Phys. Rev. Lett.*, vol. 120, p. 200501, May 2018.

[23] P. Kurpiers, M. Pechal, B. Royer, P. Magnard, T. Walter, J. Heinsoo, Y. Salathé, A. Akin, S. Storz, J.-C. Besse, S. Gasparinetti, A. Blais, and A. Wallraff, “Quantum communication with time-bin encoded microwave photons,” *Phys. Rev. Applied*, vol. 12, p. 044067, Oct 2019.

[24] P. Magnard, S. Storz, P. Kurpiers, J. Schär, F. Marxer, J. Lütolf, T. Walter, J.-C. Besse, M. Gabureac, K. Reuer, A. Akin, B. Royer, A. Blais, and A. Wallraff, “Microwave quantum link between superconducting circuits housed in spatially separated cryogenic systems,” *Phys. Rev. Lett.*, vol. 125, p. 260502, Dec 2020.

[25] H. J. Kimble, “The quantum internet,” *Nature*, vol. 453, no. 7198, pp. 1023–1030, 2008.

[26] N. Gisin and R. Thew, “Quantum communication,” *Nature Photonics*, vol. 1, pp. 165–171, Mar 2007.

[27] R. Valivarthi, S. I. Davis, C. Peña, S. Xie, N. Lauk, L. Narváez, J. P. Allmaras, A. D. Beyer, Y. Gim, M. Hussein, G. Iskander, H. L. Kim, B. Korzh, A. Mueller, M. Rominsky, M. Shaw, D. Tang, E. E. Wollman, C. Simon, P. Spentzouris, D. Oblak, N. Sinclair, and M. Spiropulu, “Teleportation systems toward a quantum internet,” *PRX Quantum*, vol. 1, p. 020317, Dec 2020.

[28] P. Kurpiers, T. Walter, P. Magnard, Y. Salathe, and A. Wallraff, “Characterizing the attenuation of coaxial and rectangular microwave-frequency waveguides at cryogenic temperatures,” *EPJ Quantum Technology*, vol. 4, p. 8, May 2017.

[29] R. W. Andrews, R. W. Peterson, T. P. Purdy, K. Cicak, R. W. Simmonds, C. A. Regal, and K. W. Lehnert, “Bidirectional and efficient conversion between microwave and optical light,” *Nature Physics*, vol. 10, pp. 321–326, Apr 2014.

[30] M. Mirhosseini, A. Sipahigil, M. Kalaee, and O. Painter, “Superconducting qubit to optical photon transduction,” *Nature*, vol. 588, pp. 599–603, Dec 2020.

[31] A. Wallraff, D. I. Schuster, A. Blais, L. Frunzio, R.-. S. Huang, J. Majer, S. Kumar, S. M. Girvin, and R. J. Schoelkopf, “Strong coupling of a single photon to a superconducting qubit using circuit quantum electrodynamics,” *Nature*, Sep 2004.

[32] O. Astafiev, A. M. Zagoskin, A. A. Abdumalikov, Y. A. Pashkin, T. Yamamoto, K. Inomata, Y. Nakamura, and J. S. Tsai, "Resonance fluorescence of a single artificial atom," *Science*, vol. 327, no. 5967, pp. 840–843, 2010.

[33] B. Kannan, A. Almanakly, Y. Sung, A. Di Paolo, D. A. Rower, J. Braumüller, A. Melville, B. M. Niedzielski, A. Karamlou, K. Serniak, A. Vepsäläinen, M. E. Schwartz, J. L. Yoder, R. Winik, J. I.-J. Wang, T. P. Orlando, S. Gustavsson, J. A. Grover, and W. D. Oliver, "On-demand directional photon emission using waveguide quantum electrodynamics," 2022.

[34] P. Krantz, M. Kjaergaard, F. Yan, T. P. Orlando, S. Gustavsson, and W. D. Oliver, "A quantum engineer's guide to superconducting qubits," *Applied Physics Reviews*, vol. 6, p. 021318, June 2019.

[35] J. Bardeen, L. N. Cooper, and J. R. Schrieffer, "Theory of superconductivity," *Phys. Rev.*, vol. 108, pp. 1175–1204, Dec 1957.

[36] B. Josephson, "Possible new effects in superconductive tunnelling," *Physics Letters*, vol. 1, no. 7, pp. 251–253, 1962.

[37] U. Vool and M. Devoret, "Introduction to quantum electromagnetic circuits," *International Journal of Circuit Theory and Applications*, vol. 45, no. 7, pp. 897–934, 2017.

[38] M. Tinkham, *Introduction to Superconductivity.* Dover Publications, 2 ed., June 2004.

[39] R. P. Feynman, R. B. Leighton, and M. Sands, *The feynman lectures on physics, vol. III: The New Millennium Edition: Quantum Mechanics.* Basic Books, 2015.

[40] J. Koch, T. M. Yu, J. Gambetta, A. A. Houck, D. I. Schuster, J. Majer, A. Blais, M. H. Devoret, S. M. Girvin, and R. J. Schoelkopf, "Charge-insensitive qubit design derived from the cooper pair box," *Phys. Rev. A*, vol. 76, p. 042319, Oct 2007.

[41] J. A. Schreier, A. A. Houck, J. Koch, D. I. Schuster, B. R. Johnson, J. M. Chow, J. M. Gambetta, J. Majer, L. Frunzio, M. H. Devoret, S. M. Girvin, and R. J. Schoelkopf, "Suppressing charge noise decoherence in superconducting charge qubits," *Phys. Rev. B*, vol. 77, p. 180502, May 2008.

[42] M. D. Lukin, "Modern atomic and optical physics - harvard university," 2021.

[43] H. Io-Chun, "Quantum optics with propagating microwaves in superconducting circuits," 2013.

[44] D. M. Pozar, *Microwave engineering; 4th ed.* Hoboken, NJ: Wiley, 2012.

[45] K. Lalumière, B. C. Sanders, A. F. van Loo, A. Fedorov, A. Wallraff, and A. Blais, "Input-output theory for waveguide qed with an ensemble of inhomogeneous atoms," *Phys. Rev. A*, vol. 88, p. 043806, Oct 2013.

[46] P.-O. Guimond, B. Vermersch, M. L. Juan, A. Sharafiev, G. Kirchmair, and P. Zoller, "A unidirectional on-chip photonic interface for superconducting circuits," *npj Quantum Information*, vol. 6, p. 32, Mar 2020.

[47] N. Gheeraert, S. Kono, and Y. Nakamura, "Programmable directional emitter and receiver of itinerant microwave photons in a waveguide," *Phys. Rev. A*, vol. 102, p. 053720, Nov 2020.

[48] M. Mirhosseini, E. Kim, X. Zhang, A. Sipahigil, P. B. Dieterle, A. J. Keller, A. Asenjo-Garcia, D. E. Chang, and O. Painter, "Cavity quantum electrodynamics with atom-like mirrors," *Nature*, vol. 569, no. 7758, pp. 692–697, 2019.

[49] R. Loudon, *The Quantum Theory of Light.* Oxford: Clarendon Press, 1973.

[50] P. Solano, J. A. Grover, J. E. Hoffman, S. Ravets, F. K. Fatemi, L. A. Orozco, and S. L. Rolston, "Chapter seven - optical nanofibers: A new platform for quantum optics," vol. 66 of *Advances In Atomic, Molecular, and Optical Physics*, pp. 439–505, Academic Press, 2017.

[51] B. R. Mollow, "Power spectrum of light scattered by two-level systems," *Phys. Rev.*, vol. 188, pp. 1969–1975, Dec 1969.

[52] A. A. Abdumalikov, O. V. Astafiev, Y. A. Pashkin, Y. Nakamura, and J. S. Tsai, "Dynamics of coherent and incoherent emission from an artificial atom in a 1d space," *Phys. Rev. Lett.*, vol. 107, p. 043604, Jul 2011.

[53] C. Eichler, D. Bozyigit, C. Lang, L. Steffen, J. Fink, and A. Wallraff, "Experimental state tomography of itinerant single microwave photons," *Phys. Rev. Lett.*, vol. 106, p. 220503, Jun 2011.

[54] I.-C. Hoi, C. M. Wilson, G. Johansson, T. Palomaki, B. Peropadre, and P. Delsing, "Demonstration of a single-photon router in the microwave regime," *Phys. Rev. Lett.*, vol. 107, p. 073601, Aug 2011.

[55] I.-C. Hoi, T. Palomaki, J. Lindkvist, G. Johansson, P. Delsing, and C. M. Wilson, "Generation of nonclassical microwave states using an artificial atom in 1d open space," *Phys. Rev. Lett.*, vol. 108, p. 263601, Jun 2012.

[56] R. HANBURY BROWN and R. Q. TWISS, "A test of a new type of stellar interferometer on sirius," *Nature*, vol. 178, pp. 1046–1048, Nov 1956.

[57] W. D. Oliver, J. Kim, R. C. Liu, and Y. Yamamoto, "Hanbury brown and twiss-type experiment with electrons," *Science*, vol. 284, no. 5412, pp. 299–301, 1999.

[58] A. F. van Loo, A. Fedorov, K. Lalumière, B. C. Sanders, A. Blais, and A. Wallraff, "Photon-mediated interactions between distant artificial atoms," *Science*, vol. 342, no. 6165, pp. 1494–1496, 2013.

[59] I.-C. Hoi, A. F. Kockum, L. Tornberg, A. Pourkabirian, G. Johansson, P. Delsing, and C. M. Wilson, "Probing the quantum vacuum with an artificial atom in front of a mirror," *Nature Physics*, vol. 11, no. 12, pp. 1045–1049, 2015.

[60] P. Forn-Díaz, C. W. Warren, C. W. S. Chang, A. M. Vadiraj, and C. M. Wilson, "On-demand microwave generator of shaped single photons," *Phys. Rev. Applied*, vol. 8, p. 054015, Nov 2017.

[61] J.-C. Besse, K. Reuer, M. C. Collodo, A. Wulff, L. Wernli, A. Copetudo, D. Malz, P. Magnard, A. Akin, M. Gabureac, G. J. Norris, J. I. Cirac, A. Wallraff, and C. Eichler, "Realizing a deterministic source of multipartite-entangled photonic qubits," *Nature Communications*, vol. 11, p. 4877, Sep 2020.

[62] B. Kannan, M. J. Ruckriegel, D. L. Campbell, A. Frisk Kockum, J. Braumüller, D. K. Kim, M. Kjaergaard, P. Krantz, A. Melville, B. M. Niedzielski, A. Vepsäläinen, R. Winik, J. L. Yoder, F. Nori, T. P. Orlando, S. Gustavsson, and W. D. Oliver, "Waveguide quantum electrodynamics with superconducting artificial giant atoms," *Nature*, vol. 583, pp. 775–779, Jul 2020.

[63] B. Kannan, D. L. Campbell, F. Vasconcelos, R. Winik, D. K. Kim, M. Kjaergaard, P. Krantz, A. Melville, B. M. Niedzielski, J. L. Yoder, T. P. Orlando, S. Gustavsson, and W. D. Oliver, "Generating spatially entangled itinerant photons with waveguide quantum electrodynamics," *Science Advances*, vol. 6, no. 41, p. eabb8780, 2020.

[64] K. Y. Bliokh, F. J. Rodríguez-Fortuño, F. Nori, and A. V. Zayats, "Spin–orbit interactions of light," *Nature Photonics*, vol. 9, pp. 796–808, Dec 2015.

[65] P. Solano, P. Barberis-Blostein, and K. Sinha, "Collective directional emission from distant emitters in waveguide QED," *arXiv:2108.12951 [quant-ph]*, Aug. 2021. arXiv: 2108.12951.

[66] E. S. Redchenko, A. V. Poshakinskiy, R. Sett, M. Zemlicka, A. N. Poddubny, and J. M. Fink, "Tunable directional photon scattering from a pair of superconducting qubits," *arXiv:2205.03293 [quant-ph]*, 2022.

[67] F. Yan, P. Krantz, Y. Sung, M. Kjaergaard, D. L. Campbell, T. P. Orlando, S. Gustavsson, and W. D. Oliver, "Tunable coupling scheme for implementing high-fidelity two-qubit gates," *Phys. Rev. Applied*, vol. 10, p. 054062, Nov 2018.

[68] Y. Sung, L. Ding, J. Braumüller, A. Vepsäläinen, B. Kannan, M. Kjaergaard, A. Greene, G. O. Samach, C. McNally, D. Kim, A. Melville, B. M. Niedzielski, M. E. Schwartz, J. L. Yoder, T. P. Orlando, S. Gustavsson, and W. D. Oliver, "Realization of high-fidelity cz and $zz$-free iswap gates with a tunable coupler," *Phys. Rev. X*, vol. 11, p. 021058, Jun 2021.

[69] M. S. Khalil, M. J. A. Stoutimore, F. C. Wellstood, and K. D. Osborn, "An analysis method for asymmetric resonator transmission applied to superconducting devices," *Journal of Applied Physics*, vol. 111, no. 5, p. 054510, 2012.

[70] S. Probst, F. B. Song, P. A. Bushev, A. V. Ustinov, and M. Weides, "Efficient and robust analysis of complex scattering data under noise in microwave resonators," *Review of Scientific Instruments*, vol. 86, no. 2, p. 024706, 2015.

[71] D. C. McKay, S. Filipp, A. Mezzacapo, E. Magesan, J. M. Chow, and J. M. Gambetta, "Universal gate for fixed-frequency qubits via a tunable bus," *Phys. Rev. Applied*, vol. 6, p. 064007, Dec 2016.

[72] T. F. Havel, "Robust procedures for converting among lindblad, kraus and matrix representations of quantum dynamical semigroups," *Journal of Mathematical Physics*, vol. 44, no. 2, pp. 534–557, 2003.

[73] K. Reuer, J.-C. Besse, L. Wernli, P. Magnard, P. Kurpiers, G. J. Norris, A. Wallraff, and C. Eichler, "Realization of a universal quantum gate set for itinerant microwave photons," *Phys. Rev. X*, vol. 12, p. 011008, Jan 2022.

[74] C. Eichler, D. Bozyigit, and A. Wallraff, "Characterizing quantum microwave radiation and its entanglement with superconducting qubits using linear detectors," *Phys. Rev. A*, vol. 86, p. 032106, Sep 2012.

[75] K. Inomata, Z. Lin, K. Koshino, W. D. Oliver, J.-S. Tsai, T. Yamamoto, and Y. Nakamura, "Single microwave-photon detector using an artificial l-type three-level system," *Nature Communications*, vol. 7, no. 1, p. 12303, 2016.

[76] S. Kono, K. Koshino, Y. Tabuchi, A. Noguchi, and Y. Nakamura, "Quantum non-demolition detection of an itinerant microwave photon," *Nature Physics*, vol. 14, pp. 546–549, Jun 2018.

[77] C. Eichler, "Experimental characterization of quantum microwave radiation and its entanglement with a superconducting qubit," 2013.

[78] J. Shapiro, "Quantum optical communication," 2016.

[79] J. M. Chow, J. M. Gambetta, A. D. Córcoles, S. T. Merkel, J. A. Smolin, C. Rigetti, S. Poletto, G. A. Keefe, M. B. Rothwell, J. R. Rozen, M. B. Ketchen, and M. Steffen, "Universal quantum gate set approaching fault-tolerant thresholds with superconducting qubits," *Phys. Rev. Lett.*, vol. 109, p. 060501, Aug 2012.

[80] Y. Yin, Y. Chen, D. Sank, P. J. J. O'Malley, T. C. White, R. Barends, J. Kelly, E. Lucero, M. Mariantoni, A. Megrant, C. Neill, A. Vainsencher, J. Wenner, A. N. Korotkov, A. N. Cleland, and J. M. Martinis, "Catch and release of microwave photon states," *Phys. Rev. Lett.*, vol. 110, p. 107001, Mar 2013.

[81] M. Pechal, L. Huthmacher, C. Eichler, S. Zeytinoğlu, A. A. Abdumalikov, S. Berger, A. Wallraff, and S. Filipp, "Microwave-controlled generation of shaped single photons in circuit quantum electrodynamics," *Phys. Rev. X*, vol. 4, p. 041010, Oct 2014.

[82] J. I. Cirac, P. Zoller, H. J. Kimble, and H. Mabuchi, “Quantum state transfer and entanglement distribution among distant nodes in a quantum network,” *Phys. Rev. Lett.*, vol. 78, pp. 3221–3224, Apr 1997.

[83] J. I. Cirac, A. K. Ekert, S. F. Huelga, and C. Macchiavello, “Distributed quantum computation over noisy channels,” *Phys. Rev. A*, vol. 59, pp. 4249–4254, Jun 1999.

[84] Pechal, Marek, *Microwave photonics in superconducting circuits*. PhD thesis, 2016.

[85] L. Jiang, J. M. Taylor, A. S. Sørensen, and M. D. Lukin, “Distributed quantum computation based on small quantum registers,” *Phys. Rev. A*, vol. 76, p. 062323, Dec 2007.

[86] K. S. Chou, J. Z. Blumoff, C. S. Wang, P. C. Reinhold, C. J. Axline, Y. Y. Gao, L. Frunzio, M. H. Devoret, L. Jiang, and R. J. Schoelkopf, “Deterministic teleportation of a quantum gate between two logical qubits,” *Nature*, vol. 561, pp. 368–373, Sep 2018.

[87] W. Dür, “Multipartite entanglement that is robust against disposal of particles,” *Phys. Rev. A*, vol. 63, p. 020303, Jan 2001.

[88] H. Yan, Y. Zhong, H.-S. Chang, A. Bienfait, M.-H. Chou, C. R. Conner, E. Dumur, J. Grebel, R. G. Povey, and A. N. Cleland, “Entanglement purification and protection in a superconducting quantum network,” *Phys. Rev. Lett.*, vol. 128, p. 080504, Feb 2022.

[89] D. M. Greenberger, M. A. Horne, A. Shimony, and A. Zeilinger, “Bell’s theorem without inequalities,” *American Journal of Physics*, vol. 58, no. 12, p. 1131–1143, 1990.

[90] C. Macklin, K. O’Brien, D. Hover, M. E. Schwartz, V. Bolkhovsky, X. Zhang, W. D. Oliver, and I. Siddiqi, “A near–quantum-limited Josephson traveling-wave parametric amplifier,” *Science*, vol. 350, no. 6258, pp. 307–310, 2015.